Master Thesis

Development and investigations of patient specific models of LVAD assisted hearts for flow field analysis in PIV experiments.

carried out for the purpose of obtaining the degree of Diplom-Ingenieur (Dipl.-Ing.)/Master of Science (MSc)

submitted at TU Wien

Faculty of Mechanical and Industrial Engineering

by

Alexander MAURER

Mat.No.: 00925733

under the supervision of

Ao. Univ. Prof. Heinrich Schima, PhD

Institute of Fluid Dynamics and Heat Transfer

Vienna, October 22nd 2023

_____

Signature

The experiments performed in this work were conducted during my employment at the *Ludwig Boltzmann Gesellschaft für Kardiovaskuläre Forschung*. Additionally, the project partially funded by the *Jubiläumsfonds of the Austrian National Bank*, Project Nr. 17314, titled "Patient individualized Fluid Dynamics in the Assisted Heart for Stroke Prevention".

I confirm, that the printing of this thesis required the approval of the examination board.

Affidavit

I declare in lieu of oath, that I wrote this thesis and carried out the associated research myself, using only the literature cited in this volume. If text passages from sources are used literally, they are marked as such.

I confirm that this work is original and has not been submitted for examination elsewhere, nor is it currently under consideration for a thesis elsewhere.

I acknowledge that the submitted work will be checked electronically-technically using suitable and state-of-the-art means (plagiarism detection software). On the one hand, this ensures that the submitted work was prepared according to the high-quality standards within the applicable rules to ensure good scientific practice "Code of Conduct" at the TU Wien. On the other hand, a comparison with other student theses avoids violations of my personal copyright.

Place and Date	*Signature*

Acknowledgements

I would like to thank my family for always supporting me during my studies and throughout my life.

I would like to thank my thesis advisor Prof. Schima for giving me the opportunity to gather research and work experience in his work group, for providing me with guidance and support during my research work and for his patience.

I would like to thank the entire PIV and CFD group at the Center for Medical Physics at AKH Wien, especially Thananya Khienwad, who I spent countless hours working over small and large problems in the course of our PIV experiments. Without her, this work would not have been possible. Thank you to Mojgan Ghodrati for assisting me with problems, giving me advice and making the work environment more enjoyable. Thank you to Philipp Aigner for guiding me through the challenges encountered in this project and providing feedback at all steps of the experimental process.

Table of Contents

English Abstract

Left Ventricular Assist Devices (LVADs) are an essential therapy for end-stage heart failure patients. Although 2 year survival rates have steadily increased since early generation LVADs, some problems remain. LVADs influence the intraventricular flow and can lead to increased risk of thrombus formation and other adverse events. One crucial aspect of LVAD therapy is implantation position, which can also influence thrombogenic risk and patient outcomes. This study seeks to demonstrate novel methods for generating flow phantoms from CT images of LVAD supported Left Ventricles and to compare two possible pump positions in a patient specific left ventricular model using two-dimensional Particle Image Velocimetry (PIV) experiments in a mock circulatory loop (MCL) setup.

The Patient specific models were created via Computed Tomography (CT) and three-dimensional processing software. The first model matches the position and angle of the LVAD found in the CT images (in-situ). The in situ position represented a diaphragmatic implantation position, while the modified position of the second model corresponds to an apical configuration. Additionally, the novel patient specific model creation process and subsequent PIV analysis with contractile wall movement have not been reported in scientific literature in the past. The experiments were performed with several contractility settings, including a patient specific hemodynamic profile, which matches the clinical parameters of the patient at the time of imaging. Analysis of PIV data can provide insight into the hemodynamic behavior associated with each pump position, including general velocity fields and specific pulsatility and stagnation parameters.

The modified pump position showed lower stagnation in the apical region in the entire apex, which is critical for thrombus formation. The largest decrease in mean SI that was observed in the apex inside a single plane corresponded to a reduction by 53%. Pulsatility was, however, not generally improved for this pump position and shows several cases where it was in fact decreased.

This comparative analysis demonstrates the impact of LVAD position on hemodynamic parameters and provides some insight into the complicated nature of LVAD and LV interactions. These findings suggest that it could be beneficial to investigate individual LVAD

placements based on patient specific factors such as ventricular geometry pre-operatively, which could improve patient outcomes.

Deutsche Kurzfassung

Linksventrikuläre Unterstützungspumpen (LVADs) sind eine essenzielle Behandlungsmethode für fortgeschrittene Herzinsuffizienz. Obwohl die klinische Ergebnisse solcher Behandlungsformen über die letzten Jahre stetig verbessert wurden, bestehen dennoch einige Probleme. LVADs können durch Veränderung des intraventrikulären Flusses zu einem erhöhten Risiko für Thrombusbildung und andere Probleme führen. Ein sehr wichtiger Aspekt von LVADs ist ihre Position im Ventrikel, welche ebenfalls einen erheblichen Einfluss auf das Thromboserisiko und andere Aspekte haben kann.

Diese Studie präsentiert neue Methoden, mit denen Modelle hergestellt werden können die in Strömungsmechanischen Untersuchungen verwendet werden. Zwei Pumpenpositionen werden innerhalb eines Modells eines linken Ventrikels in einem künstlichen Strömungsaufbau mittels zweidimensionaler *Particle Image Velocimetry* (PIV) Methoden verglichen.

Die Patientenmodelle wurden mittels CT Datensätzen und 3D Modellierungssoftware generiert. Das erste Modell entspricht der in den CT Daten sichtbaren LVAD Position innerhalb des linken Ventrikels des Patienten. Das zweite Modell hat eine modifizierte Pumpenposition zur Spitze des Ventrikels lateral verschoben und verdreht. Die Originalposition entspricht einer diaphragmatischen Position, während die modifizierte Position einer apikalen Position entspricht. Die Untersuchung solcher individuell angepasster Modelle in Strömungsaufbauten mit Pulsatilen Volumen wurde bisher nicht in wissenschaftlichen Publikationen veröffentlicht. Die Experimente wurden mit drei verschiedenen Konfigurationen der Schlagvolumen gemacht, unter anderem mit einer an den klinischen Daten des Patienten angenäherten Einstellung, die zur Zeit der CT-Aufnahme festgehalten wurden. Die Analyse der PIV Resultate soll zeigen, wie sich die Position des LVADs auf das intraventrikuläre Strömungsverhalten und davon abhängigen Parametern wie Stagnation oder Pulsatilität auswirken kann.

In den Ergebnissen zeigt die modifizierte Pumpenposition niedrigere Stangation in kritischen Bereichen für das Thromboserisiko. Die größte Senkung der mittleren Stagnation in dem apikalen Bereich liegt bei 53% gegenüber dem in-situ Modell. Gleichzeitig zeigt dieses modifzierte Modell allerdings auch vermehrt niedrigere Pulsatilität in den selben Bereichen.

Diese komparative Analyse soll den Einfluss der LVAD-position auf hemodynamischen Parametern zeigen und Einsicht in die komplizierte Interaktion zwischen LVAD und dem linken Ventrikel geben. Diese Resultate zeigen, dass es wichtig sein könnte, die LVAD Position mithilfe von individuellen Faktoren wie Ventrikulärer Geometrie vor einer Implantation anzupassen, da verbesserte Ergebnisse in Bezug auf Thromboserisiko und anderen Problemen zu erwarten sein könnten.

List of Figures

List of Tables

List of Abbreviations and Symbols

LVAD … Left Ventricular Assist Device

PIV … Particle Image Velocimetry

MCL … Mock Circulatory Loop

IC … Inflow Cannula

MV … Mitral Valve

AV … Aortic Valve

LV … Left Ventricle

LA … Left Atrium

CVD … Cardiovascular Disease

ECG … Electrocardiogram

RBC … Red blood cell

Re … Reynolds Number

PI … Pulsatility Index

SI … Stagnation Index

CT … Computed Tomography

HU … Hounsfield unit

IMAR … Iterative metal artefact reduction

SV … Stroke volume

1. Introduction and Motivation

1.1 General Introduction

Cardiovascular disease (CVD) is the leading cause of death in most of the world, with up to 18 million deaths per year, or roughly 32% of all total deaths worldwide yearly. One of the largest challenges in the field of cardiac surgery today is the dependence on heart transplants, which are resource intensive and rely on the donation suitable hearts as a source. Left Ventricular Assist Devices (LVADs) provide a treatment method for certain heart disease conditions that would lead to heart failure or death without transplantation. LVADs were initially used as *bridge to transplant* devices, which extended the amount of time a patient could wait for a suitable transplant to become available. Over recent years many improvements have been made in various aspects of the LVADs, which has allowed them to be implanted as *destination therapy*, with the average survival of patients approaching an average of 5 years [1]–[4]. Today's implanted LVADs are 3rd generation LVADs such as Abbott's Heartmate 3 (Abbott Laboratories, Chicago, IL, USA), and previously also Medtronic's HVAD (Medtronic, Minneapolis, MN, USA), which has been discontinued and is no longer be available for implantation.

One of the main remaining problems of this generation of LVADs is the possible occurrence of thromboembolic complications and infection post-implant, potentially caused by the altered intraventricular flow field, change in shear rates and through the complicated interactions of pharmacological factors which are influenced by the supplemental medication required by the patient after LVAD implantation [5]–[8]. The occurrence of unphysiological low velocity flow regions caused by the presence and operation of the LVAD is also associated with an increased risk of thrombus formation [5], [7], [9]–[12]. Proper positioning of the LVAD inside the ventricle has an influence on thromboembolic risk as well [13]–[19]. One in-silico publication reported decreased stagnation for an apical pump configuration, when compared to a diaphragmatic configuration [15]. Describing the factors that create the low velocity regions in LVAD assisted hearts should lead to improvements in patient survivability (or reduction in adverse events) through findings for pump design, control aspects or surgical implantation methods.

Visualization of the intraventricular flow or the tissue surrounding the LVAD can be difficult due to the Titanium alloy housing of the device. A common approach for modeling flow fields of LVAD assisted hearts is to use in-vitro Particle Image Velocimetry (PIV) setups, where a mechanically assisted left ventricular (LV) model is investigated through use of a LV model placed in a mock circulatory loop (MCL) setup. Recent developments in additive manufacturing and cardiac segmentation algorithms have led to more accurate modeling of the geometry of patient specific LVs. While limitations remain, these new models provide many benefits and enable visualization of patient specific LVAD supported geometries.

The supported left ventricle of a single LVAD patient who suffered an ischemic stroke was segmented and two pump configurations were selected for PIV experiments using pulsatile LV models in an MCL setup. The results of these intraventricular flow field

investigations, as well as the novel approach for creating soft, flexible patient specific left ventricular models for PIV experiments in a pulsatile mock loop setup will be presented in this work.

The experimental results and the results of two different approaches to the patient specific model creation process are presented here, alongside many aspects from image acquisition of the cardiac CT, image processing methods, creation of the 3D-model and experimental methods required for proper PIV imaging. One patient specific geometry was created according to the exact locations found in the CT images and the second model was created with a modified pump position, which corresponds to the ideal implantation position and direction based on common guidelines for pump implantation. The changes in the intraventricular flow field resulting from the change in LVAD position show a reduction in stagnation areas in many parts of the LV model, especially in the apical region. Fluid stagnation inside the ventricle has been linked to an increased risk for thrombus formation and indicates that the altered apical position and angling of the inflow cannula toward the mitral valve is more optimized in this aspect. Stagnation was reduced in the apex and while pulsatility was increased, which indicates improved washout with the modified pump position.

1.2 Study Aim

This project aims to investigate the impact of LVAD positioning inside patient specific left ventricular models in in-vitro Particle Image Velocimetry (PIV) experiments. For this purpose, a patient specific model was created from CT images reproducing the patient's anatomical structure and LVAD position as seen in the images (diaphragmatic position). A second artificial pump position was selected for comparison with this model, with a laterally displaced position of the IC corresponding to an apical pump position.

The main objectives of this project are as follows:

1. Creation of two patient specific flexible translucent models for invitro PIV experiments in a mock loop setup
2. Flow field analysis of each model, including additional ROI flow parameter analysis in the apex of each model
3. Comparison of these results in an effort to understand the impact of LVAD placement on critical flow parameters for thrombosis risk in LVAD patients.

2. Background

The cardiovascular system is a circulatory system that encompasses various organs and other components such as arteries, veins, the lymphatic system, the lung, capillaries and the heart (Figure 1).

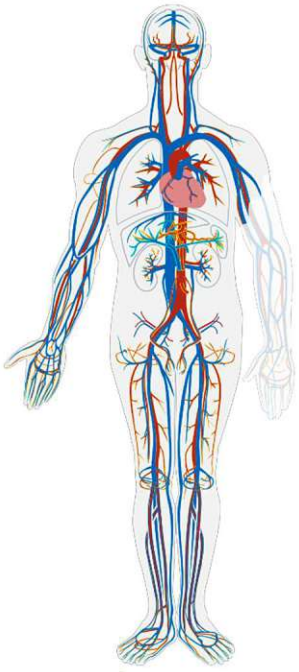

Figure 1: An overview of the human circulatory system. The heart, lung, kidneys, liver and main arteries and veins are depicted in the image. [20]

While the most obvious function of the cardiovascular system is the transport of blood throughout the body, it carries a wide variety of transport- as well as non-transport related functions. The transport of liquids, nutrients, minerals, hormones, metabolic products and blood gases is performed with the heart acting as a pump, delivering these components throughout the body and enabling exchange of these components between cells and tissue. One of the most complex functions of blood lies withing its possibility to coagulate, involving mechanisms such as platelet activation, adhesion and aggregation or deposition of fibrin.

The pumping mechanism of the heart consists of two phases: diastole and systole. In short, the left ventricle contracts in systole, ejecting blood volume into the circulatory system through the opened aortic valve. This phase is followed by the diastolic (filling) phase, where blood enters the left ventricle before the cycle is repeated.

The circulatory system can be considered as a combination of two systems in series: the arterial system and the venous system. The systems can each be characterized through their different mean oxygen concentrations (oxygenated vs de-oxygenated blood), transport direction, as well as through the pressures occurring in the systems.

The large circulation is responsible for transporting nutrients and oxygen throughout the cardiovascular system and starts in the left ventricle, where blood is ejected into the aorta, before circulating to locations of gas exchange (capillaries) and once again returning to the heart, entering the small circulatory system via the right atrium. The small system transports blood to and from the lungs for O_2 and CO_2 exchange and is considered to start at the right ventricle and end at the left atrium.

2.1 Cardiac Anatomy & Physiology

The heart is an organ consisting of specialized muscle cells known as the myocardium and acts as the pump for the entire circulatory system. It consists of four chambers: the left and right atria as well as the left and right ventricles (Figure 2). The combination of left atrium and left ventricle are often referred to as the *left heart* - the same is true for the right side. The circulatory system consists of two subsystems, where the left and right heart can be viewed as two pumps connected in series. The right heart contains both the right atrium and right ventricle, the atrioventricular valve (tricuspid) as well as the pulmonary valve and acts as a low pressure pump (<25mmHg) that transports blood to the lungs for gas exchange.

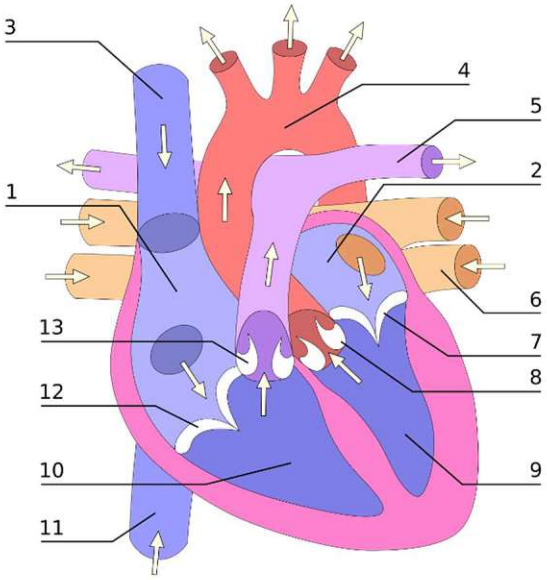

Figure 2: The four chambered heart. Components: 1) Right Atrium. 2) Left Atrium. 3)Vena cava superior. 4) Aorta. 5) Pulmonary artery. 6) Pulmonary vein. 7) Mitral valve. 8) Aortic valve. 9) Left ventricle. 10) Right ventricle. 11) Vena cava inferior. 12) Tricuspid valve 13) Pulmonary valve. [21]

The right side of the heart acts as a volume pump in both diastole and systole. The left ventricle behaves as a volume pump in systole and a suction pump in diastole and is generally a higher pressure system with a mean pressure of 100mmHg, which is maintained by the heart pumping mechanism.

During the cardiac cycle heart valves act as monodirectional flow gates, closing when the pressure difference and flow between the connected chambers is reduced to zero, preventing backward flow. In the left ventricle the atrioventricular valve is a bileaflet valve known as the mitral valve, which is prevented from prolapsing into the atrium during systole by the chordae tendineae. The left ventricle can exhibit highly individualized complex trabeculae structures, which are sometimes strongly pronounced.

2.1.1 Hemodynamics and Electrocardiograms

Hemodynamics describes blood flow in the circulatory system and includes all homeostatic mechanisms ultimately responsible for the dynamics of the circulatory system. Due to the hybrid nature of blood, which is a suspension of solid components in a fluid, its behavior is not just regulated passively from external influences such as gravity but also through biochemical processes such as coagulation, which can occur in the microscopic level of the fluid in response to changes in pressure or flow. These processes are highly complex and depend on numerous physical and biochemical parameters and will be further described in a later section.

The physiological nature of the pulsatile cardiac system can be visualized with pressure and volume curves, as well as electrocardiogram and phonocardiogram curves, of the LV, such as the one seen in Figure 3. The pressure inside the LV (blue), LA (yellow) and aorta (red) can be seen in the top graph. After atrial systole (a) the mitral valve closes, which produces an audible signal in the acoustic phonocardiogram at the bottom of the figure. This closing enables isovolumic contraction which produces a steep pressure increase while the volume remains constant (=isovolumic), as visible in the volume curve (pink) below the pressure graph. Once the LV pressure increases over the aortic pressure the aortic valve opens and ejection begins. When the LV pressure decreases below the aortic pressure the aortic valve closes (2nd heart sound) and isovolumic relaxation begins. The pressure drops rapidly during this phase and once the atrial pressure is reached the mitral valve opens, enabling rapid inflow. The end of inflow is once again reached when atrial contraction is complete and the cycle repeats again. The electrocardiogram (ECG, green) below the volume curve in Figure 3 shows the signal captured through electrodes representing the current dipole created by the electrical excitation of the heart. The characteristic phases of the ECG are the P wave, representing atrial excitation, the QRS complex and the T wave. The QRS complex represents ventricular excitation that travels as an action impulse from the sinoatrial node (primary pacemaker of the heart) toward the atrioventricular node, where it passes to the bundle of his and so-called purkinje fibers. The T wave represents repolarization of the ventricles. The direction of the total electric dipole is captured through the use of three or more electrodes and the projection of the three dimensional dipole on two dimensional axes.

Note the aortic pressure curve in Figure 3, which decreases steadily after isovolumic relaxation. The aorta achieves this smoothing of the pulsatile nature of cardiac contraction through the so-called Windkessel effect, which is an effect of the more elastic vessel walls that allows expansion and temporary storage of blood for delayed distribution throughout the systemic circulation.

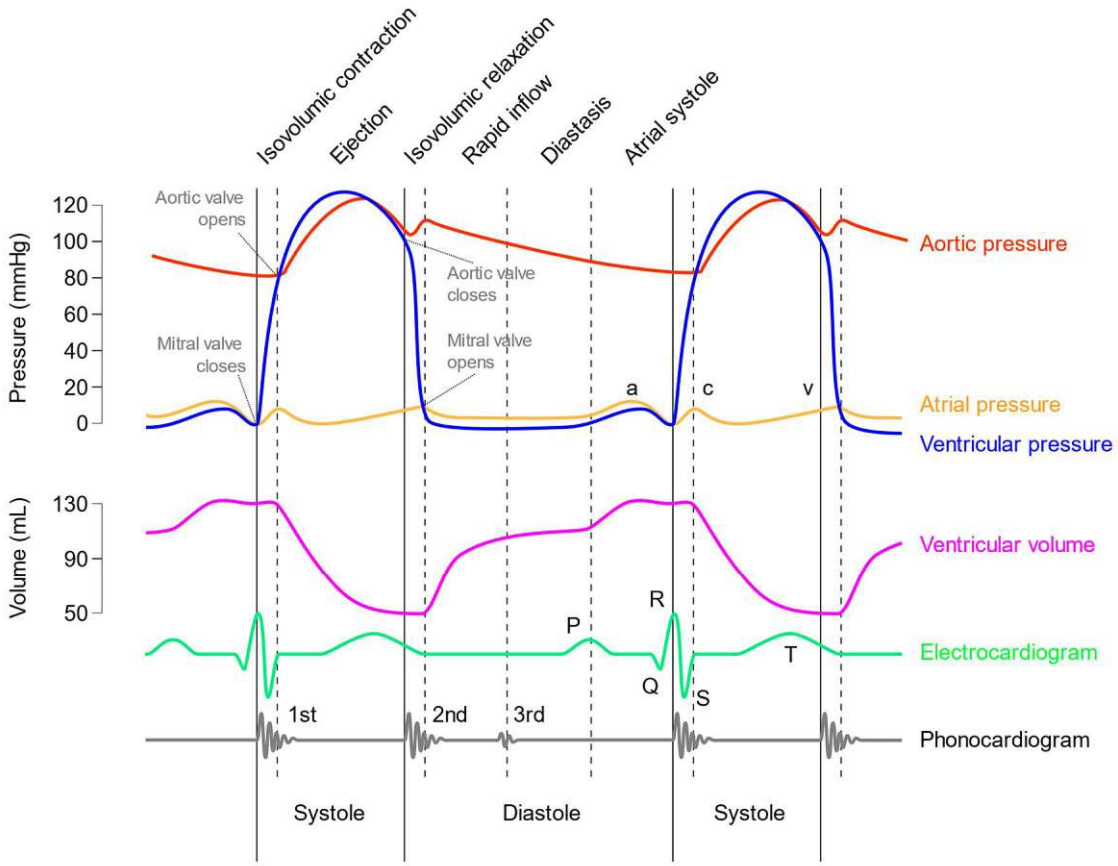

Figure 3: The Cardiac Cycle. [20]

2.2 Blood

2.2.1 Components

Blood is a suspension of blood cells in blood plasma and is the medium used for delivering nutrients and oxygen throughout the circulatory system by the body in vertebrates. Blood cells consist mainly of three types of cells: red and white blood cells, as well as platelets. Red blood cell's (RBC or erythrocytes) cytoplasm contains large amounts of hemoglobin, the protein responsible for binding oxygen to RBCs for oxygen transportation. Each red blood cell contains hemoglobin molecules as well as other components vital for cell function, such as other proteins and lipids. The term white blood cell refers to a variety of cells, such as monocytes and lymphocytes, that are a part of the body's immune system and aid by destroying or removing pathogens or other undesired substances from the body. The suspension of all these particles inside the liquid plasma makes blood act as a non-Newtonian fluid.

2.2.2 Blood Damage and Thrombosis

Damage to blood can occur in a variety of ways, including "hemolysis, platelet activation, alteration of the coagulation cascade, thrombosis and emboli, reduced functionality of the white blood cells, and destruction of von Willebrand factor (vWf)" [21]. Hemolysis is dependent on shear stress magnitudes and exposure times [22] and the shear rate and

vorticity play a crucial role in thrombus formation, especially since “viscosity and therefore coagulation are dependent on velocity gradients” [23]. Regions of low wall shear stress have been considered clinically relevant parameters for thrombus deposition and are often linked to regions of stasis [24], while high shear rates can activate platelets and lead to the formation of microparticles [25]. Stenoses are regions where the narrowing of vessel walls can lead to regions of increased shear rates, however LVADs must consider these aspects in pump design as well.

Thrombosis is a highly complex mechanism that enables blood coagulation when certain conditions arise in the cardiovascular system. A simple but rather effective model for the description of thrombus generation can be described using Virchow’s triad [26]: The factors of stasis of blood flow, endothelial injury and hypercoagulability all contribute to thrombus formation. While it is often difficult to exactly determine the origin or cause of a thrombotic event in clinical settings, LVAD designs must consider how to prevent activation of one or more of these mechanisms to guarantee complication free transportation of blood through the cardiovascular system.

Stasis refers to the case where alterations in normal blood flow lead to local low flow velocities. These situations can arise during long surgeries or even extended air or car travel. In this project one of the main concerns with positioning of the inflow cannula was the creation of areas of stasis in the apex of the ventricle. Pump positioning and control (i.e. pump speed modulation) seems to play a role in the development of stasis.

Endothelial injury concerns any situation in which injuries or trauma cause damage to vessel walls, as well as events where extreme shear rates (low or high) occur, which can lead to the activation of the highly complex coagulation cascade as a response. Also, surface phenomena and the contact of blood with the surface of the LVAD inflow cannula can lead to formation of thrombi and must be considered in the design of the LVAD.

The third and final aspect of Virchow’s triad concerns **Hypercoagulability**, or abnormally strong tendencies to develop thrombi due to an alteration in the constituents of blood. Patients suffering from hypercoagulability don’t necessarily require external events to trigger thrombus generation, but rather suffer from diseases such as *factor V Leiden*, or others, which can lead to excessive formation of thrombi and cause complications in routine procedures.

In the mechanical circulatory support field, it is critical to minimize the impact of the LVAD on these clotting factors, especially stasis and endothelial injury, as the pump is a foreign object placed into the ventricle and in contact with blood at all times. The formation of a thrombus inside the ventricle that is then released and transported via the LVAD into the circulation can cause pulmonary embolisms, ischemic strokes and other fatal adverse events. This is one of the most dangerous occurrences for LVAD patients and its risks must be minimized.

Thrombi forming in the ventricle are called pre-pump thrombi, while those occurring inside of the pump or outside of the outflow graft are called intra- and post-pump thrombi, respectively. While it is often difficult to exactly determine the origin of a thrombus, proper

pump design and placement are considered vital to minimize the prevalence of these events for LVAD patients.

2.3 Heart failure

Heart failure is a progressive disease that is characterized by an inability of the heart muscle to pump blood effectively through the circulatory system. Heart failure can be caused by high blood pressure, diabetes and other diseases and even by an unhealthy diet. There are many forms of heart failure, often classified either by the preservation or reduction of its ejection fraction.

$$EF[\%] = \frac{SV}{EDV} * 100 \qquad \text{(Eq. 1)}$$

Where EF is the ejection fraction in %,

SV is the stroke volume, or the volume of ejected blood (in systole),

and EDV is the End Diastolic Volume, or the maximum volume of the heart (in diastole).

Heart transplantation is still a viable treatment method today along with LVAD therapy, however a lack of suitable donor hearts limits the viability of large scale transplantation for patients suffering from end stage heart failure. The improvement of LVAD therapy with regards to patient outcomes and quality of life has made it possible to move from a form of bridge to transplant therapy to destination therapy. This is in large part due to the modernization of LVAD technology, as well as improvements in patient care and other aspects. Failing hearts are able to regain some loss of function under LVAD support due to an effect called reverse remodeling [27].

2.4 PIV

Due to the complexity of the topic the explanations will be kept brief, however more comprehensive explanations can be found in Raffel et al [28], which is considered standard PIV literature. The purpose of this section is to provide a brief overview over the methods applied in these experiments.

2.4.1 Light Sources and Light Sheet Optics

There are various forms of laser technologies and though the most commonly used lasers in PIV applications are either gas or semiconductor lasers. The most commonly used gas lasers in PIV are Argon-ion lasers, though very high currents are required to achieve excitation states [29]. Semiconductor lasers offer several advantages and the laser used in the gathering of experimental data for this diploma thesis was a semiconductor laser (Nd:YAG).

Laser light can be used for a variety of interferometry applications. In PIV experiments an optical setup is used to create thin laser light sheets for scattering events captured from light scattering particles suspended in fluids. The shape of the light beam is adapted through the use of specific lenses, ultimately resulting in the creation of a thin light sheet, which can then be used for two-dimensional PIV imaging.

2.4.2 Tracer Particles

PIV as a measurement technique actually indirectly measures the velocity of the flow fields by directly measuring the velocity of the tracer particles suspended inside the fluid. Therefore, PIV experiments require seeding of light scattering particles within the imaged fluid. Tracer particles must therefore follow the true flow of the fluid during the experiments, requiring careful choice of seeding particle properties to achieve neutral buoyancy in the fluid. Should the density of the fluid and tracer particles be different, sedimentation or rising of these particles would occur due to gravitationally induced velocity.

Consider the "gravitationally induced velocity U_g of a spherical tracer particle in a viscuous fluid at a very low Reynolds number" [30]:

$$U_g = d_p^2 \frac{(\rho_g - \rho)}{18\mu} g \qquad \text{(Eq. 2)}$$

Where U_g is the gravitationally induced velocity of the tracer particle,

d_p is the diameter of the spherical tracer particle.

The gravitationally induced velocity is zero when neutral buoyancy is achieved, or ρ equals ρ_g.

2.5 Mathematical Background

2.5.1 Blood Flow

The fluid mechanical properties of blood are non-Newtonian in nature since blood consists of a suspension of particles inside a liquid. The consequence of this mixture is that "shear stress is a *nonlinear* function of the local strain rate. It depends not only on the local strain rate, but also on its *history*. Such '*memory*' effect gives the fluid an elastic property, in addition to its viscous property. Most non-Newtonian fluids are therefore *viscoelastic*."[31]

The equation governing the motion of viscous fluids is called the Navier-Stokes equation. For non-Newtonian fluids this equation exists with adaptations, such as for Bingham fluids (i.e. toothpaste) or Power-law fluids (i.e. corn starch slurries), however no analytical solution to the equation has been discovered so far. A common approach to solving problems where the Navier-Stokes equation governs the system in question is to use numerical simulations or experimental methods such as PIV.

A consequence of the viscoelastic properties of blood is the existence of two general types of flow: *laminar* and *turbulent* flow.

2.5.2 Laminar and Turbulent Flow

In 1883 Reynolds demonstrated the existence of two types of flow of water through a tube, by injecting a thin stream of dye into the flow and varying the velocity of the flow. At low flow velocity the dye remained inside a well-defined straight path along the flow direction.

No mixing was visible between these layers at low flow velocity. The appearance of these straight flow lines resembles laminae, hence the name laminar flow (Figure 4, top) [32].

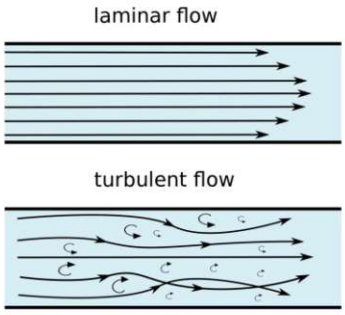

Figure 4: Laminar and turbulent flow. In laminar flow, the individual layers do not transition over each other. Turbulent flow shows eddies of varying sizes where flow direction is disturbed. [33]

Increasing the flow velocity above a certain threshold caused mixing of the individual parallel layers, visualized by irregular motion of the dye streak and spreading throughout the cross section of the tube. Such flow behavior is called *turbulent* flow (Figure 4, bottom). In Reynolds' experiments a transition between laminar and turbulent flow was always observed at a certain ratio between fluid velocity, tube diameter and fluid viscosity, also called the Reynolds number (transition at Re ≈ 3000).

$$Re = \frac{Vd}{\nu} \qquad \text{(Eq. 3)}$$

Where V is the velocity averaged over the cross section of the tube

d is the diameter of the tube

ν is the viscosity of the fluid

Turbulent flow is associated with energy loss and more inefficient fluid transport when compared to laminar flow. In the case of characteristic LVAD flow patterns occurring in supported hearts, vortices appearing in intraventricular flow could however be beneficial in assisting with washout of stagnant flow areas.

2.5.3 Equations & Calculated Parameters

Continuity Equation

Since the two subsystems are connected in series, net flow through both systems must be equal over time, otherwise nonzero divergence of liquid on one side of the system would be the consequence, reminiscent of the behavior of voltage dividing circuits in electrical engineering. This fundamental consequence of the connection in series is described through the continuity equation, which is presented in differential form for fluid dynamics (eq. 4).

$$\frac{\partial \rho}{\partial t} + \vec{\nabla} \cdot (\rho \vec{u}) = 0 \qquad \text{(Eq. 4)}$$

Where ρ is the *fluid density*,

t is *time* and

$\vec{u}$ is the *flow velocity vector field*.

The continuity equation is a conservation equation that is presented here in its differential form. It describes how the rate at which mass enters the system is equal to the rate at which mass leaves the system plus the accumulation of mass inside the system. If no accumulation of mass occurs, then the net flux remains zero and the inflow is equal to outflow. In a simplified form, where the fluid is assumed to be incompressible, this equation can be simplified to a volume continuity equation:

$$\vec{\nabla} \cdot \vec{u} = 0 \qquad \text{(Eq. 5)}$$

Where $\vec{u}$ is the *flow velocity vector field*.

Ohm's Law

The cardiovascular system can be approximated by a lumped parameter circuit where Ohm's law describes the relationship between pressure and flow.

Cardiac adaptation: $\bar{p}_{Arterial} = CO * \bar{R}_{Periphera}$ (Eq. 6)

Where $\bar{p}_{Arterial}$ is the mean arterial pressure,

CO is total cardiac output and

$\bar{R}_{Peripheral}$ is the *mean peripheral vascular resistance*.

Classic Ohm's Law	Voltage	Resistance	Current
Cardiovascular	Mean arterial pressure	Mean peripheral vascular resistance	Cardiac output

In the experimental setup a (peripheral) resistance clamp is placed in the mock flow circuit to adjust the hemodynamic settings of the MCL (see MCL section for more details).

Ensemble Averaging

"A *collection* of experiments, performed under an identical set of experimental conditions, is called an *ensemble*, and an average over the collection is called an *ensemble average*, or *expected value.*"[34] PIV measurements are performed repeatedly for each experimental setting to allow for ensemble averaging, since turbulent flow fields are being measured which would otherwise make comparisons between conditions very challenging.

$$\vec{v}_{Ensemble}(x, y, t) = \frac{\sum_i \vec{v}_i(x,y,t)}{n} \qquad \text{(Eq. 7)}$$

Where $\vec{v}_{Ensemble}(x, y, t)$ is the ensemble average in each point (x,y) for each timepoint (t),

$\vec{v}_i(x,y,t)$ is the time-resolved velocity field of the individual measurements in each point (x,y),

and n is the number of individual measurements.

This is sometimes referred to as the phasic average since each phase of the cardiac cycle consists of data from multiple measurements to create a single representative time-resolved flow field.

Mean velocity calculation (Steady State)

$$\vec{v}(x,y) = \frac{\sum_t \vec{v}(x,y,t)}{n} \quad \text{(Eq.8)}$$

The mean velocity vector in each coordinate (x,y) is calculated by creating the mean from the time-resolved velocity in each coordinate.

Pulsatility Index:

The pulsatility index (PI) is a dimensionless local quantity that can be used to describe the local pulsatility inside the flow field over the duration of the PIV measurement. The definition for the pulsatility index is:

$$PI(x,y) = \frac{|\vec{v}_{max}(x,y)| - |\vec{v}_{min}(x,y)|}{|\vec{v}_{mean}(x,y)|} \quad \text{(Eq. 9)}$$

Where $|\vec{v}_{max}(x,y)|$ is the magnitude of the maximum velocity in each pixel (x,y),

$|\vec{v}_{min}(x,y)|$ is the magnitude of the minimum velocity in each pixel (x,y)

And $|\vec{v}_{mean}(x,y)|$ is the mean velocity magnitude in each pixel (x,y).

An increase in PI corresponds to a wider range of velocities being observed within a pixel or ROI, when averaged over all pixels inside an ROI.

Stagnation Index

The Stagnation Index (SI) is a local quantity that is inversely related to the velocity

$$SI(x,y) = \sqrt{\frac{A_{LV} * t}{\int_0^t |\vec{v}(x,y)|^2 dt}} \quad \text{(Eq.10)}$$

Where A_{LV} is the total area of the flow field (or Region of Interest),

t is the duration of the observation and

$\int_0^t |\vec{v}(x,y)|^2 dt$ corresponds to the integral over the observation duration of the local velocity magnitude in each pixel (x,y) or all pixels inside an ROI. The units of the SI are [$s*m^{-1}$].

3. Methods & Materials

3.1 Overview of the Study

The topics covered in this Master Thesis pertain to the creation process for physical models of patient specific Left Ventricular (LV) geometries and subsequent in-vitro flow field analysis of these patient specific LVAD supported hearts in an experimental Particle Image Velocimetry (PIV) system (Figure 5). Starting from CTs acquired from LVAD patients who suffered ischemic strokes the heart geometry was segmented and prepared for manufacturing of transparent silicone models which could be placed in a Mock Circulatory Loop (MCL) for PIV imaging. Additionally, modifications were performed on the patient's LVAD position within the LV, enabling direct in-vitro comparison of the flow fields resulting from two different pump positions in the same patient specific LV geometry. The geometry of a single patient was selected for closer experimental analysis in this thesis, though several models were created in the scope of a related project at the Center for Medical Physics and Biomedical Technology, at the General Hospital Vienna. The segmented 3D CT geometries were converted into 3D CAD models for the application of additive manufacturing methods. In this process the segmented geometry was presented to clinical experts and with their guidance the exact positioning of the pump was selected.

While the presence of LVADs in the LV already leads to unphysiological flow behavior inside the ventricle, the in-situ implantation position found in the CT images seemed to be laterally displaced aways from the apex of the ventricle, possibly exacerbating these flow conditions. Therefore, under the guidance of clinicians, a second theoretical pump position was defined, which corresponds to an apical implantation of the LVAD, with the inflow cannula (IC) facing directly to the Mitral Valve (MV) – which is considered to be the standard implant method for LVADs.

By comparing the resulting flow fields of these two models some insight could be gained on the influence of the pump position on the intraventricular flow and its consequences on apical stagnation and thrombogenic risk inside the LV. Clearly defined relationships for the distances and angles of the Aortic Valve (AV), MV and IC could be determined using CAD software (Inventor, Autodesk, Inc., San Rafael, CA, USA) and physical models were manufactured using PLA filament or Stereolithographic methods. A hollow silicone model with roughly 2mm wall thickness was created, using conventional Mold-injection methods or Rotocasting methods.

PIV experiments were performed on each model, using the same PIV setup for each, with slight adaptations to the experimental setup resulting from the geometry changes. This mainly concerned changes to the position and angle of the HVAD and custom pump holder inside the MCL setup. Software processing of this data was performed in the acquisition software (Dantec Dynamics GmbH, Ulm, Germany), as well as in MATLAB (MathWorks, Natick, MA, USA).

The PIV system used for these experiments is an existing system at the Center for Medical Physics and Biomedical Technology at the Medical University of Vienna. The

methods described in the following sections were developed in close cooperation with Ms. Dr. med. scien. Thananya Khienwad, as similar experimental methods were applied in her doctoral thesis titled “Investigation of cardiac flow patterns in patients with cardiac assist devices using Particle Image Velocimetry: Effects of speed changes and particular patient-specific cardiac geometries” [35].

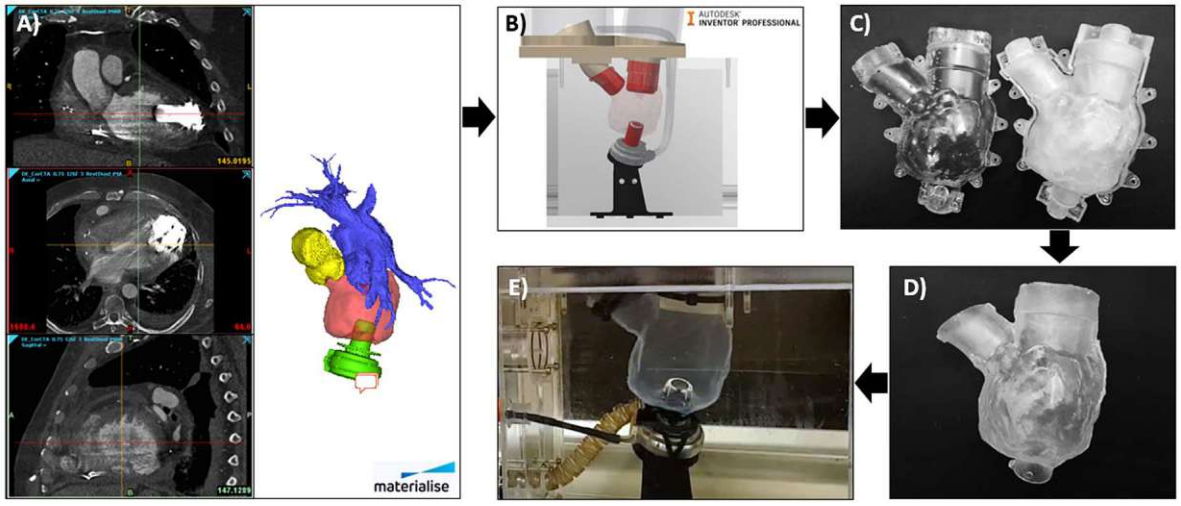

Figure 5: The model creation process: A) CT segmentation. B) Valve connectors are created and the position of the LVAD is defined in the liquid filled box of the MCL. C) Shells and a core are printed using additive manufacturing methods. For models created with rotocasting methods, this step was replaced by Rotocasting. D) A silicone model of the LV is created via injection molding from the printed parts. E) The transparent silicone model is placed on a 3D printed pump holder that assists in properly positioning the model in the MCL setup. (Source: Thesis of T. Khienwad[35])

3.2 Patient Specific Data

The patient LV was selected due to the occurrence of an ischemic stroke event under LVAD support. Image segmentation was performed at the Center for Medical Physics and Biomedical Engineering at the Medical University of Vienna and Ludwig Boltzmann Institute for Cardiovascular Research. The aim of the patient selection process was to find a patient who suffered an ischemic stroke under LVAD support (HM3 or HVAD) and was readmitted to the clinic following this event, with a subsequent CT scan of the heart. While the collection of many different patients under these criteria would have been desirable, only few CT datasets were suitable for segmentation, as the pump artifacts were so disruptive, that only few structures were clearly discernable inside the ventricle. The CTs of a single patient were selected due to the relatively high contrast of the CT images, ensuring accurate representation of the geometry in the CT data.

Hemodynamic data was also available from the patient, which was recorded around the date of the CT. This data was used as a basis for the definition of our experimental parameters in the experiments, in an attempt to recreate patient specific flow conditions. The clinically documented pump speed of the patients is significantly higher than the pump speed used in the experiments. This is due to the fact that the patient had a HM3 LVAD implanted, while we were limited to the use of HVADs in the experimental setup at this time, due to availability of a transparent IC on a modified HVAD required for PIV imaging. At the time of writing, the MCL has been adapted to include the possibility of a HM3 LVAD that has a transparent IC for further research projects. The experimental pump speed was chosen to

match the patient specific mean pump flow rate. Two additional MCL working points were defined, one additional setting for Partial Support ("Standard Partial Support") with aortic valve opening) and one for Full Support (no aortic valve opening). The final hemodynamic parameters used in the experiments as well as the hemodynamic responses of the system are presented in the results section. These parameters were achieved in the experimental setup by adapting the peripheral resistance of the MCL, the pump speed of the HVAD, the fluid level in the preload chamber and the compliant volume of air inside the aortic chamber with the aim of achieving 5 l/min total cardiac output and 80mmHg mean Aortic pressure over all working points.

3.2.1 Cardiac CT

Computed Tomography is form of X-ray technology which can be used to capture image sets (DICOM files) for multiplanar reconstruction of three dimensional objects. The CTs used for segmentation in this research project were acquired from readmitted LVAD patients suffering from ischemic events who were being treated at the Medical University of Vienna. The images were captured using an ECG gated dual-beam CT system (Siemens Somatom Drive Dual Source CT scanner, Siemens AG, Munich, Germany) at the Vienna General Hospital. Dual-beam CTs enabled imaging the patient with both 100kV and 140kV spectrum X-ray beams simultaneously, which has the benefit of increased contrast around some areas of the left ventricular myocardium at 100kV and a clear three dimensional image with the precise location of the implanted metallic LVAD housing at 140kV. Both image sets were used in Mimics 22 (Materialise NV, Leuwen, Belgium) to increase the quality of the segmentation around the apical site of the LVAD implantation, where artefacts created by the scattering of X-rays on the LVAD surface appear as shadows or bright streaks of radiation across the images. Forms of image filtering such as IMAR (Iterative Metal Artifact Reduction, Siemens AG, Munich, Germany) exist, however these filtering algorithms were created for pacemakers or other more common metallic implants and are not optimized for detecting the scattered X-rays in images where LVADs are present. Datasets with these algorithms applied were used in the segmentation process since the benefit they provided often outweighed the drawbacks, mainly the reduced contrast around the pump due to filtering of the images. While some adaptations to the capturing parameters would have been desired, data was selected from a set of captured images produced in routine follow-up examinations or after hospital readmissions.

3.3 CT Segmentation Process

3.3.1 Overview

The CT segmentation process involves several steps which will be discussed in this section, however a brief mention of important parameter choices made before and during acquisition is necessary for a better understanding of the segmentation process. Parameters such as the chosen X-ray spectrum (which is usually 100kV or 140kV for cardiac CTs) and exposure dose were chosen by radiologists to achieve the best possible image quality while keeping the patient's radiation dose as small as possible. Due to movement of the cardiac anatomy during image acquisition, ECG gating is applied during Cardiac CT imaging, where

images are collected via a gated trigger that is linked to the ECG signal of the patient. This enables repeated measurement at the same phase of the cardiac cycle and a reduction of motion artifacts. As mentioned previously, additional filtering algorithms such as iMAR can be applied to improve the image quality close to the inflow cannula of the LVAD, though these algorithms often struggle with the artifacts created by the LVAD.

The datasets were then selected for best possible contrast with the smallest available slice thickness and with a special focus for the image quality around the apex of the left ventricle. After selection, the datasets were exported to Mimics Innovation Suite (Materialise NV, Leuwen, Belgium) for segmentation. Individual image slices are carefully investigated and myocardial structures are marked during segmentation, while structures such as trabeculae and the chordae tendinae are excluded from the lumen. Once the relevant structures have been masked and labeled, a radiologist and a cardiac surgeon were consulted to confirm accurate segmentation of the cardiac structures. A second pump position was defined for the experiments with guidance of the cardiac surgeon, ensuring proper positioning of the apical pump position.

After the models were segmented, preparations for the additive manufacturing processes were made in 3-matic (Materialise NV, Leuwen, Belgium). Additional modifications to the valve connectors required for MCL implementation were performed in Inventor (Autodesk, Inc., San Rafael, CA, USA).

3.3.2 Dataset Selection

The datasets were initially analyzed using the software RadiAnt DICOM Viewer (Medixant, Poznán, Poland) with the aim of finding high contrast images. The patient chosen for this project had only 100kV images available, however the image quality was significantly better than in any other dataset. A slice thickness of 1.5mm/1mm was selected, as this slice thickness had the lowest image noise around the apical area. Since the CT image slice thickness is inversely related to the 3D voxel size, smaller slice thickness is preferable and requires less filtering during post-processing, provided the image noise is low enough to gain useful image information from the resolution increase.

3.3.3 CT Segmentation

The methods for segmentation of these models were developed and refined over the course of the project. The final approach is based on work performed in cooperation with Mr. Schneckenleitner (Figure 6) and contains methods that were refined through discussions with him in internal projects at the Center for Medical Physics and Biomedical Engineering, Medical University of Vienna. The segmentation was fully performed in *Mimics innovation suite* (Materialise NV, Leuwen, Belgium), which is a medical image data processing software for CT image segmentation. The LV, LA and Aorta ascendens were marked in the CT images by creating three dimensional masks in the software. There are a multitude of features available for segmentation inside Mimics consisting mainly of Thresholding or Mask Edit features. Thresholding uses a user defined upper and lower threshold (in Hounsfield Units, HU) to select areas corresponding to the desired tissue type. During Thresholding a bounding region is also defined in 3 dimensions by dragging the edges of the region to the

desired region of interest, reducing the number of undesired structures inside the region of interest. This bounding region was placed around the LV lumen, including parts of the Left Atrium (LA), Aorta ascendens and the other areas surrounding the LV.

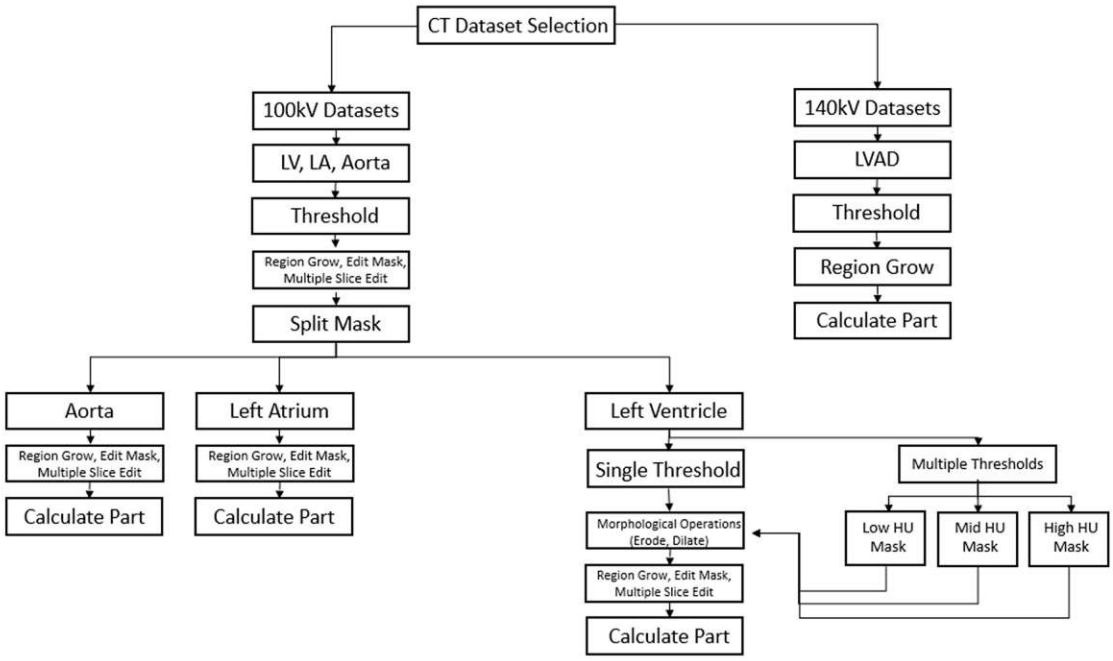

*Figure 6: Workflow of CT Segmentation Process. The starting file is a selected CT dataset and the output are Parts (**.stl** files) of the Aorta, LA, LV and LVAD with matched coordinate system for further processing. When many artifacts are present inside the LV a Multiple Threshold approach proved useful during segmentation. The multiple masks were combined to a single mask and compared to the Single Threshold mask before being finalized.*

The time required for the thresholding approach could be reduced significantly through the choice of a suitable multiplanar reconstruction view, where the three orthogonal views of the CT images could be individually rotated parallel to the direction of the inflow cannula, resulting in a clearer image of the surrounding apical area of the LV lumen (Figure 7).

The segmentation process was initially performed with a single threshold inside the LV and later refined using multiple thresholds for different areas of the ventricle, since the single threshold was not able to mark the entire LV lumen without adding additional unwanted areas outside of the LV.

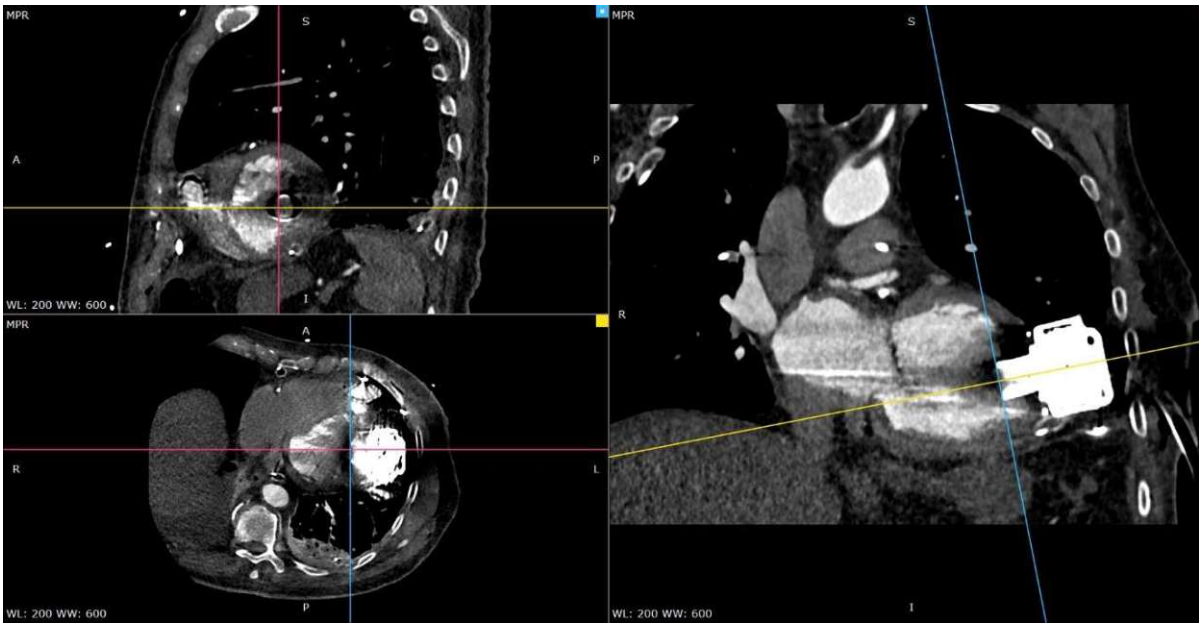

Figure 7: A Multiplanar Reconstruction (MPR) is shown using Radiant. The three planes can be rotated for orientation along the inflow cannula of the LVAD. The images here show images captured at 100kV, 1.5mm slice thickness, 60% Phase (Diastole) and with CDR iMAR filter algorithms applied. Note the black shadows around the inflow cannula, in every plane, which are still present after metal artefact reduction algorithms have been applied.

The LVAD could be segmented in a few steps by creating a new mask, applying a lower threshold of 1400 HU and an no upper limit threshold with the “keep largest object” option selected (Figure 8).

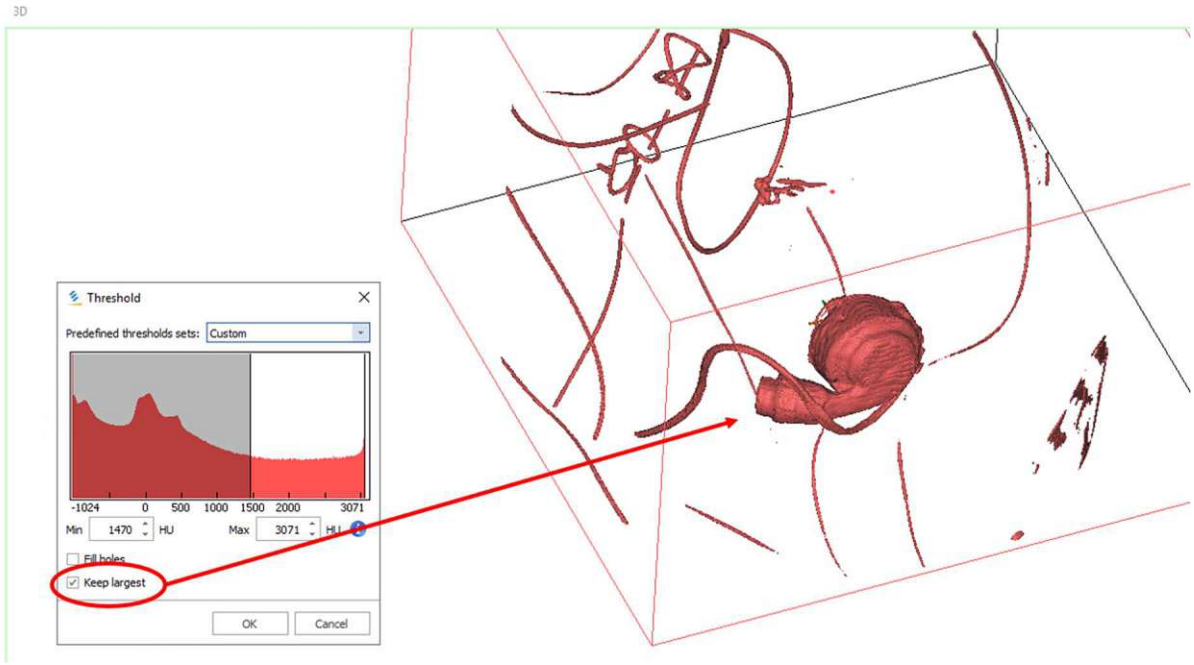

Figure 8: LVAD Segmentation can be performed in a simple step: Setting the lower threshold of the masking tool to 1500HU and the upper limit to the maximum occurring HU value, as well as selecting the “keep largest” option in the thresholding window results in the segmentation of the largest non-tissue structure. In this case this is the LVAD and its attached components, such as the outflow and driveline.

This step removes all unconnected parts from the mask of the largest object in this greyscale range, which corresponds to the LVAD. Region growing was then applied to the LVAD mask as the final step. The LVAD was segmented to allow for detailed segmentation of the

myocardium around the apex, as well as for later placement in a virtual mock loop model, where it could used to define the angle of a pump holder for exact placement inside the model ventricle (Figure 15).

A HU Threshold of 225 to 760 HU was selected for the single threshold segmentation of the LV. These upper and lower bounds lie beyond the HU boundaries usually applied in soft tissue segmentation, however this was required in this case due to the introduction of the LVAD artifacts in the images and the applied filtering method.

The detailed masking process of the LV starts by reducing the amount of unwanted data collected in the initial masks, by applying several different masking functions such as Multiple Slice Edit, Split Mask, and Region Grow in addition to the aforementioned Thresholding.

The spine and ribcage structures can be split from the LV mask using the *Edit Mask* and *Split Mask* features. A brush tool or lasso tool is used to mark the boundaries of the mask and to remove any links to ribcage or other bone structures from the LV mask. *Multiple Slice Edit* is another function that can be used to edit several layers of a mask at once, which is beneficial when the boundaries of the mask are clear but when inner ventricular structures such as trabeculation were not incorporated in the initial rough masking process (Figure 9). This function was used extensively during segmentation, sometimes with its built-in interpolation function and other times for individual layer editing. When using the linear interpolation function it is recommended to constrain the interpolation to a small length, otherwise the resulting interpolation would appear artificial and require further editing.

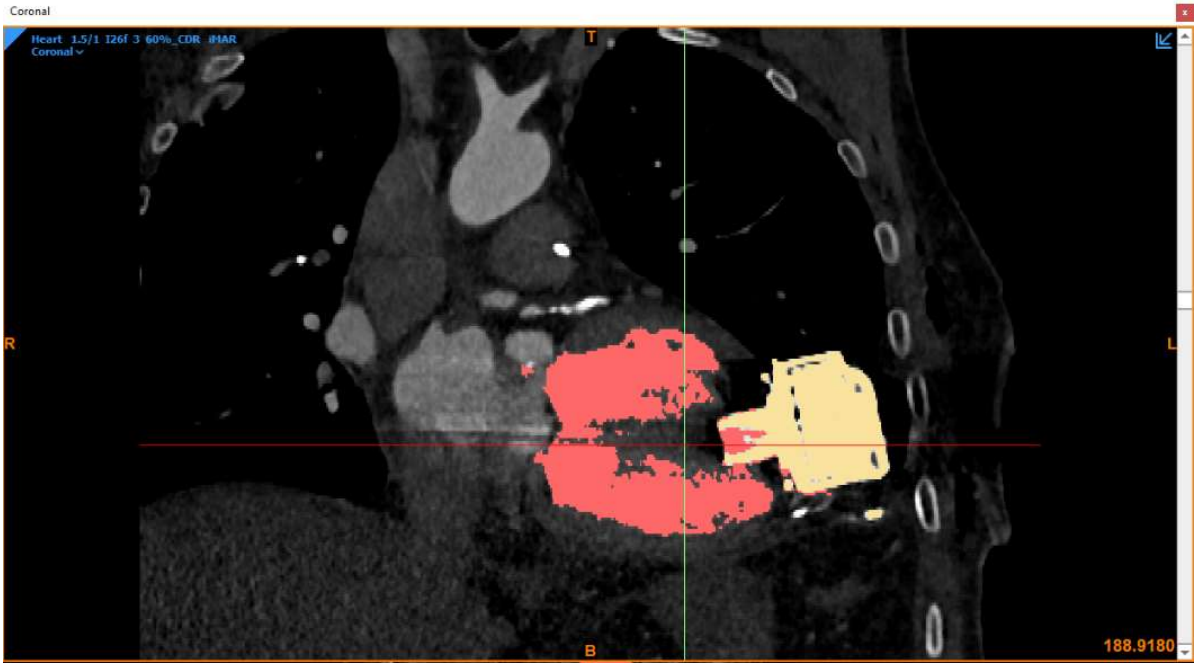

Figure 9: Trabeculation that was removed from the mask in the rough masking process needs to be filled in manually through use of Edit Mask or Multiple Slice Edit.

The first steps after LVAD segmentation consisted of removing large unwanted structures such as the spine or ribcage from the masks, as well as defining the boundaries of the LA and

Aorta with the LV, as the contrast in these areas was significantly higher than at the apical region (Figure 10).

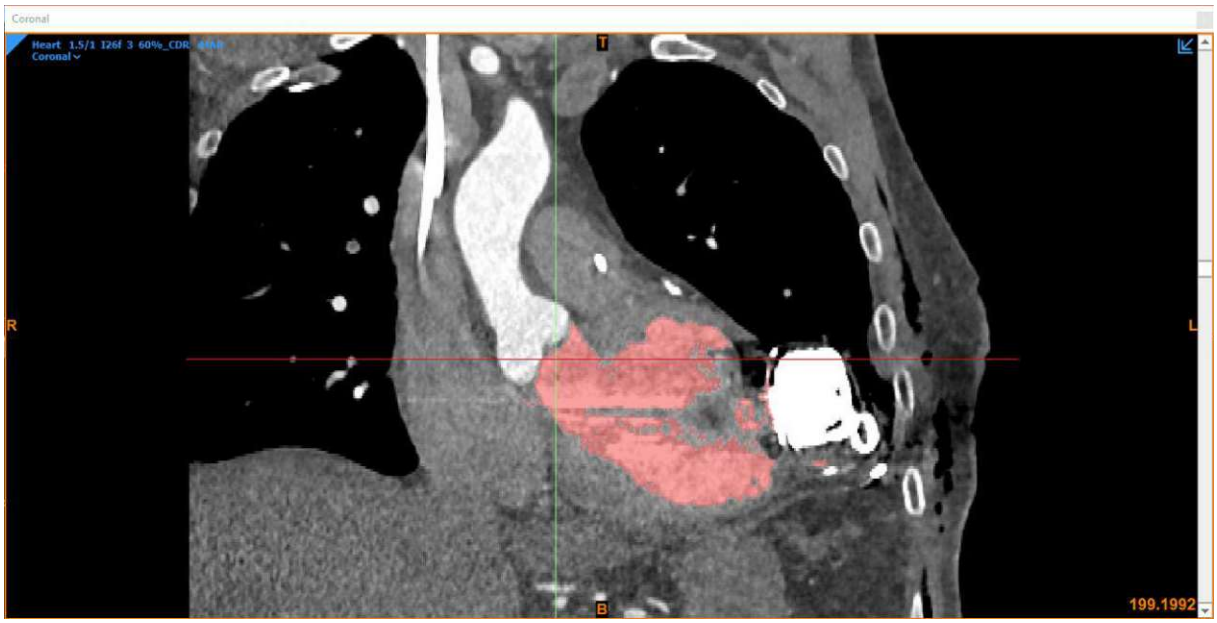

Figure 10: The Left Ventricular Outflow Tract masking resulting from the initial masking is more accurate than the masking at the apex and requires almost no further processing.

The MV can be clearly seen and separated from LV structures during segmentation (Figure 11). While the segmentation of the LA and Aorta proved straightforward, the LV required several complex steps to achieve suitable accuracy, as described in the flowchart in Figure 6. A multi-threshold approach was used for specific subregions of the LV, as the image artifacts caused the lumen of the LV to appear in different HU ranges depending on the distance to the LVAD (Figure 10).

The final masks for the Aorta, LA, LV and LVAD were all exported as parts, or stl-file format, for further processing.

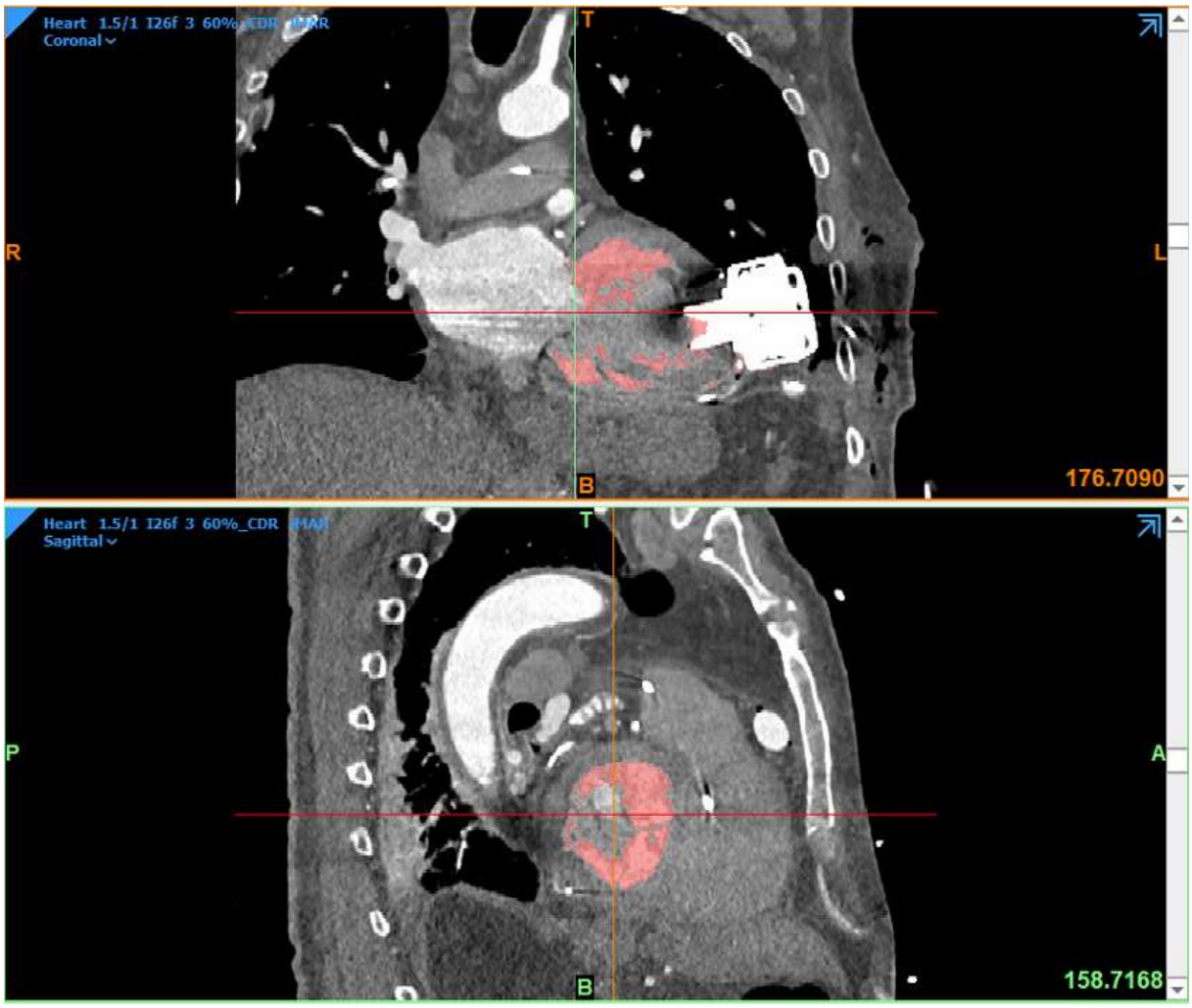

Figure 11: The Coronal & Sagittal views of the open Mitral Valve can be seen here. The MV is clearly separate from the LV Lumen in this case, however the exact border is unclear. Multiple- & Single Slice Editing are performed to define the border between the MV and LV Lumen.

3.3.4 Defining the Control Pump position

The *control pump position* was found by placing a three dimensional *part* representing the LVAD into the more optimal position at the apex of the ventricle. The *modified IC position* was defined through translation and rotation of the segmented LVAD to closely match the IC direction with the MV-apex axis. The in-situ IC position was then closed using *Multiple Slice Edit* with interpolation. The rest of the segmented model was kept identical. The finished *modified* model was presented to a cardiac surgeon and the final placement of the LVAD was decided in in a discussion based on guidelines for optimal placement. In the patient this placement was not possible due to the proximity of the LV apex to the ribcage and possibly due to other circumstances making this placement difficult or impossible (Figure 12).

The final positions of the in-situ and modified pump position were exported together with the segmented LV, ascending Aorta and LA geometries (Figure 12 and Figure 13) for post-processing.

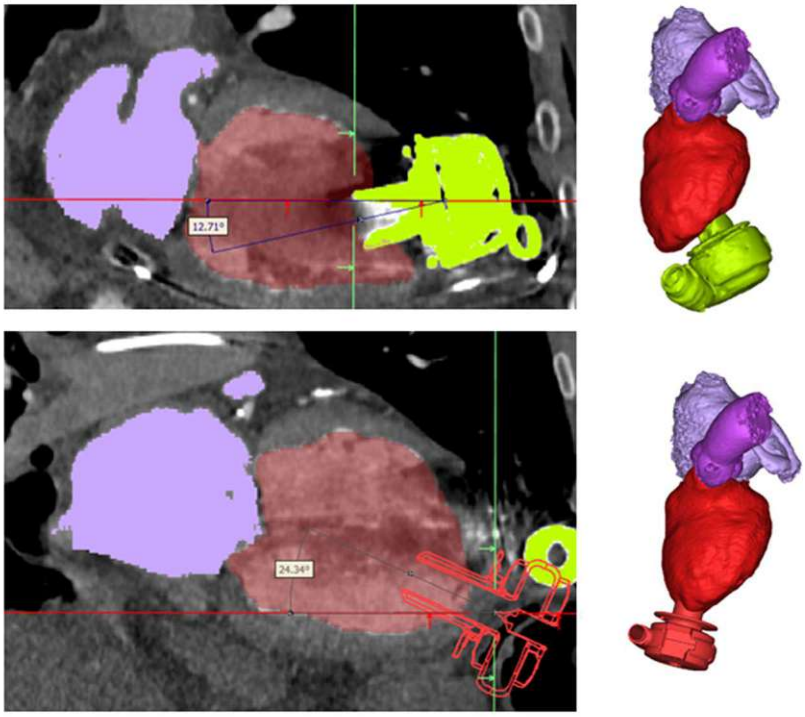

Figure 12: Side by side comparison of the two selected pump positions. The top left image shows the actual LVAD position (green LVAD mask), as captured in the CT images. On the bottom left image the outline of the modified IC position can be seen in a red outline overlayed over the CT image.

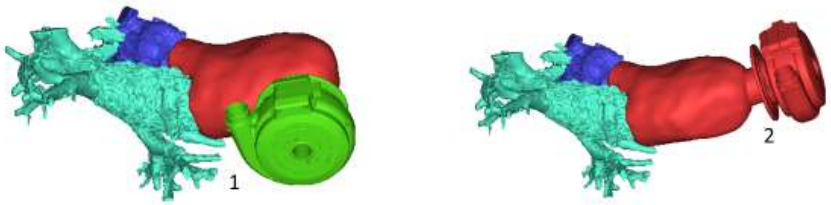

Figure 13: An alternative view of the two pump positions in the final models can be seen here. The green LVAD (1) shows the position and angle of the in-situ LVAD position as defined from the CT images. The red LVAD (2) was placed according to the recommended insertion position, which was translated toward the apex and with the IC rotated toward the MV. The structures of the Left Heart are color coded: Red – LV, Cyan – LA, Blue – Aortic Root.

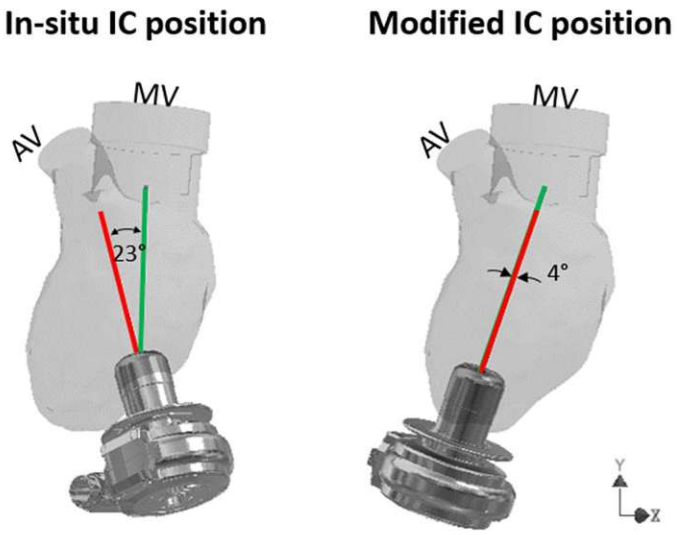

Figure 14: The two pump positions used in the experimental setups can be seen here with regards to the angle between the IC-axis and the MV-apexl-axis. The In-situ IC position (left) was segmented from the CT images, while the Modified IC position (right) was placed manually along the MV-apex axis.

3.3.5 Post-Processing

The segmentation process provides virtual models (called *parts* in Mimics) of the LV, LA, Aortic Root and LVAD, which must be smoothed and converted to STL files before 3D-printing, since the outer structure of the ventricular model can be very rough after the segmentation process. While a rough mask might be feasible for other applications, the manufacturing of the silicone models required smoother surfaces. These were imported into 3-matic (Materialise NV, Leuwen, Belgium), where filters were applied locally to uneven regions of the model. The finished model was then exported for further adaptations into the CAD software *Inventor*. Cylinders were placed at the locations of the LVAD IC, AV and MV to define the position of the cylinders containing the biological valves and the IC of the physical LVAD in the real model. The finished model was then placed inside a digital version of the MCL chamber used in PIV experiments, enabling accurate positioning of each component for placement during PIV experiments and definition of a *pump holder*, which was also printed using PLA and additive manufacturing methods for the individual pump positions found in the two configurations (Figure 15).

Figure 15: A prototype for the pump holder, which defines the direction and position of the LVAD within the MCL.

3.3.6 Model Creation

Two different manufacturing methods were used in the model creation process: Rotocasting and Injection molding using a hollow shell with an inner core. The creation process for each will be explained in this section, along with benefits and disadvantages of each.

Though many models were created in the process of developing this Thesis one final ventricular model was created through a Rotocasting approach, while another model was manufactured through silicone injection into a hollow mold with a core. The models are only discernable by their IC position.

3.3.6.1 PLA Additive manufacturing & Rotocasting

The model containing cylinders at the IC, AV and MV position was printed using PLA filament with an Anycubic i3 Mega 3D printer (HONGKONG ANYCUBIC TECHNOLOGY CO., LIMITED). The individual layers of the filament additive manufacturing process were smoothed by applying a layer of polish and hardened under UV light, preventing them from being visible in the finished silicone model which could cause problems during PIV image acquisition.

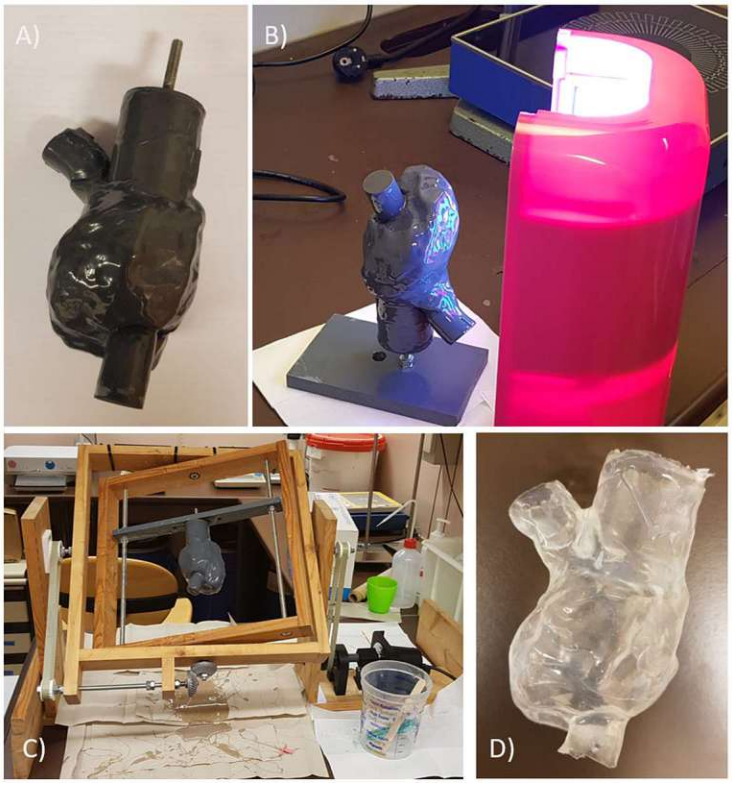

Figure 16: The segmented model (in-situ position) was printed using PLA filament additive manufacturing (A) and coated with a layer of polish that was hardened using UV light (B). It was placed in a rotocaster (C) and coated in silicone (Sortaclear-18). After a 24 hour curing process the finished model was removed from the core (D).

The polished model was then placed in a rotocasting device, which consists of two frames that can rotate individually using a belt drive system powered by a small electric motor, enabling full rotation of the model in space. The model is suspended in the middle of these frames to reduce the torque on the electric motor during rotation. The gravity acting upon the applied liquid silicone ensures an even coating of the model as long as the rotation of the model is consistent.

Roughly 150g of Sortaclear 18 were prepared by mixing the two components (Sortaclear 18 A and B) of the silicone in a 10:1 proportion. Much of this silicone was lost during rotocasting as the excess coating flowed off the model during rotation of the device. The cure time of this material was about 24h at room temperature, however the rotocaster was left running for roughly eight hours after application of the liquid silicone. After this time the silicone no longer flowed around the model when the rotocaster was left stationary for the rest of the curing process.

Multiple attempts were required since the coating depended highly on the pouring technique used in the application of the liquid material. This technique proved difficult as the frame had to rotate before application of the viscous silicone, yet the pouring of the material over the model had to be performed carefully. Small holes were sometimes found at the end of the curing process and occasionally some drops of excess silicone seemed to get caught on another side of the model due to the rotation. Overall, it was possible to

create roughly 2mm thick hollow models of the LV geometry, but it was quite tedious and prone to problems caused by the forces acting upon the rotocasting frame. The pulleys for the rotocaster had to be replaced after some hours of operation due to wear, however the low cost of these parts made this feasible, as they are all printed using the same PLA manufacturing methods used to create the LV model core. The finished model showed no differences when compared with the other applied method, however it took several attempts to achieve a working model.

3.3.6.2 Stereolithography & Injection Molding

A different method was applied in the case of the modified pump position model. The finished 3D model was used to create a 2mm thick digital model (measured from the outside of the core) and outer shells were designed to enable injection molding of Sortaclear 18 using a syringe. Screw holes were placed in close proximity all along the border where the two sides of the outer shells meet, ensuring even distribution of compressive forces during injection molding. Holes were placed above the MV and AV cylinders to enable escape of air during the injection of silicone. The injection itself was performed using an opening that was designed to fit a syringe at the bottom of the model.

The core and shells were printed using a Formlabs 2 (Formlabs Inc., Somerville, MA, USA) and cured using the Formlabs postcuring chamber (Figure 17). The assembled model was injected with the same silicone used in the rotocasting methods (Sortaclear 18, see Figure 18) and left to cure for up to 48 hours. The curing process took considerably longer with the injection molding methods. After curing was complete, the shells were separated from the core and the 2mm thick cured silicone model could be removed from the inner core.

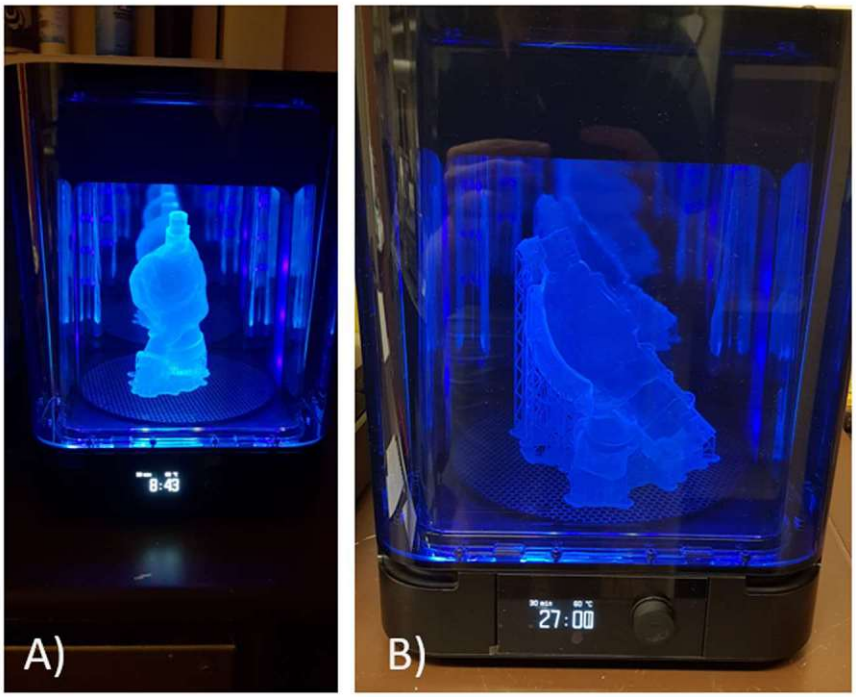

Figure 17: The printed core (A) and one side of the outer shell (B) used for injection molding of the modified model can be seen during the post-curing process.

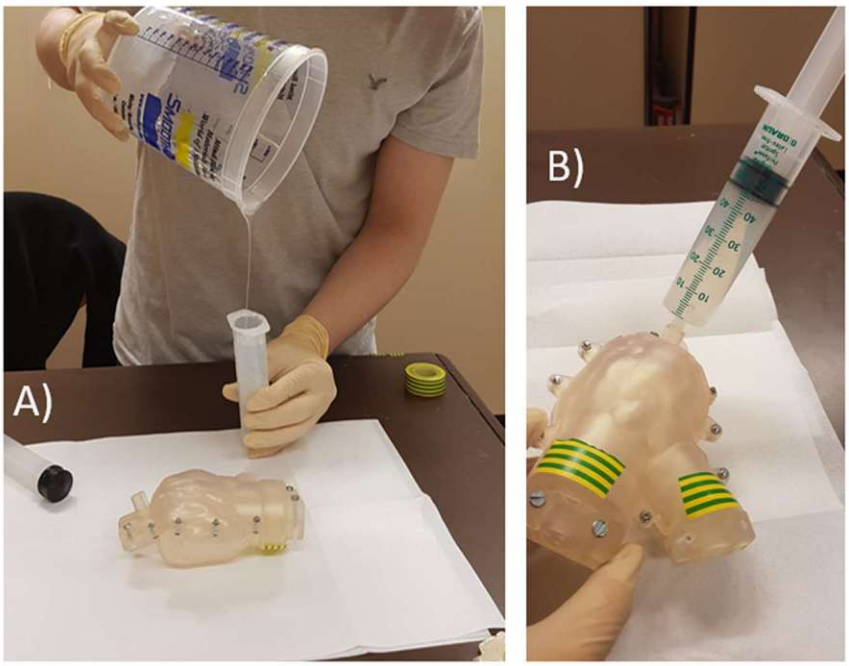

Figure 18 Sortaclear 18 was filled into a syringe with a technique that allows remaining bubbles to escape the flow (A) and injected into the mold (B)

3.3.6.3 Comparison of methods

Rotocasting proved to be fairly cheap, as all that is required is the wooden frame and parts that enable coupling to a small electric motor for rotational movement. The wooden frame and parts required some upkeep; however the replacement components were readily available in our lab workshop and should cost no more than a few Euros when bought new in a store, making rotocasting a cheap but upkeep-intensive method for the creation of these models. It was difficult but not impossible to achieve even wall thickness and to remove the models from the core without tearing the silicone. Still, this method can is viable if the more expensive alternative is not available.

Injection molding methods consisted of printing a core and shell model, which had to be designed in CAD software, using transparent material in a commercially available 3D printer. The material cost for this method is much higher, especially if the printer has to be acquired purely for this purpose. The shell and core are brittle, making repeated casting of the silicone model nearly impossible, should a replacement be required. The printing of the core and shell also takes significantly longer than just printing of the shell for the Rotocaster.

Mechanical assessment of the models was limited to a stress test, where the models were attached to tubes and filled with fluid before they were checked for stability under increasing pressure. This was done to make sure the models were able to withstand the pressure of the piston pump acting in the filled MCL. Next, they were both attached to the MCL lid, where they were filled with water and left hanging overnight. Sometimes very small tears would appear visible after this process, even though the model looked well sealed at a first glance. At that stage, the model was attached to 3D-printed tubes that had the same size and shape of the MV and AV holders and the holes were covered with additional layers

of silicone. This approach was successful when the holes were limited to the surface of the valve cylinders (outside the imaging area) however small holes could be fixed relatively inconspicuously even if they were in the middle of the LV model's walls. If the models showed signs of leaks or had too much silicone applied after these steps, an additional model had to be cast, and the best models from an optical and mechanical perspective were manufactured with the pointwise addition of silicone on problematic areas after the initial curing process was complete. Optical Assessment of the model was done using the glycerol/water mixture used in the MCL for experiments and a checkerboard graph, where the distortion of light could be assessed.

Overall, both methods were used to produce models that could be used in these experiments. The injection molding method, however, produced more reliable results as the physical spacing between core and shell is constant and leads to more easily reproducible results than the rotocasted models, where the result is somewhat dependent on the experience of the user.

3.4 Cardiac Simulator / Mock Cirulatory Loop

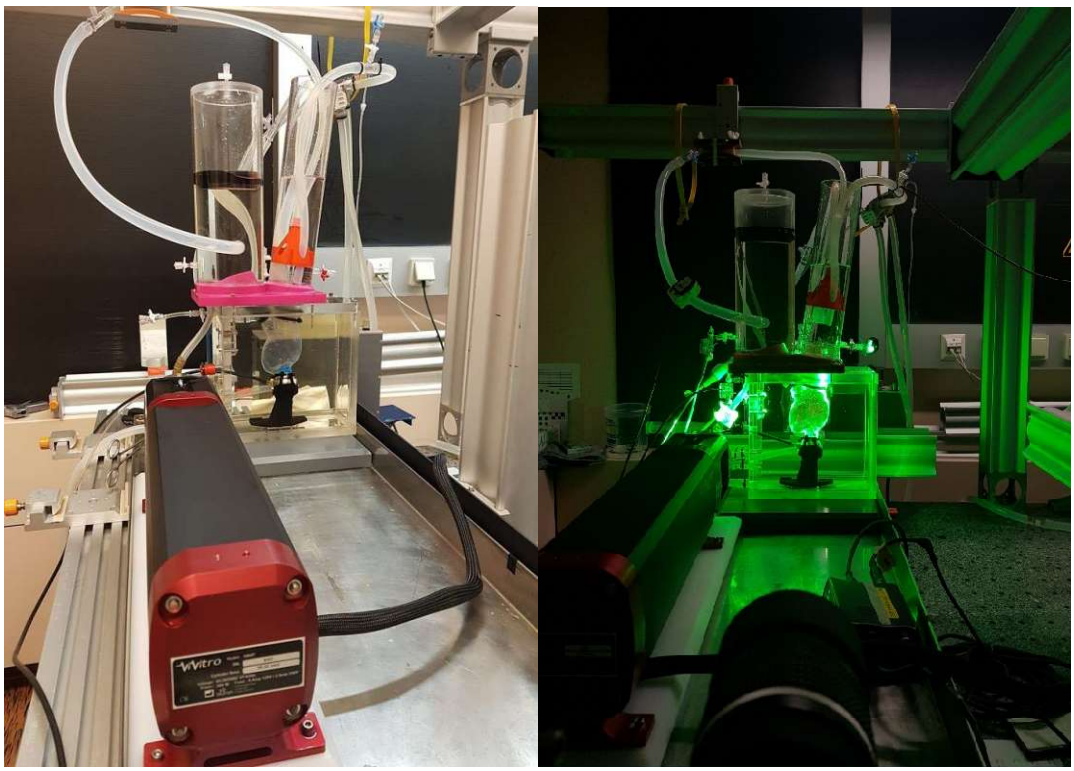

Figure 19: The Mock Circulatory Loop Setup including the Patient Specific LV geometry. The right image was captured during PIV acquisition. The light emitted by the Nd-YaG laser is in the visible spectrum of light and appears green.

3.4.1 Components

The patient specific model was placed inside a sealed chamber that was used to create the MCL setup (Figure 19) and a HVAD (Medtronic, Minneapolis, MN, USA) LVAD was inserted into the predetermined position for each model. The MCL was filled with a heated aqueous Glycerol solution (50% by weight) for the purpose of refractive index matching and viscosity

matching of the blood analogue liquid. The sintered inflow cannula of the HVAD pump was replaced with a clear polished acrylic inflow for optical purposes in the experimental setup. The valve in- or outflow sections of the model were aligned with valve-holding cylinders on the lid of the sealed chamber. Each of these cylinders contained a trileaflet porcine valve (32mm diameter for the MV, 23mm diameter for the AV) which were retrieved from a Slaughterhouse and fixated using Glutaraldehyde, as reported in a previous publication [36]. The valves can be seen in their holding cylinders in Figure 20.

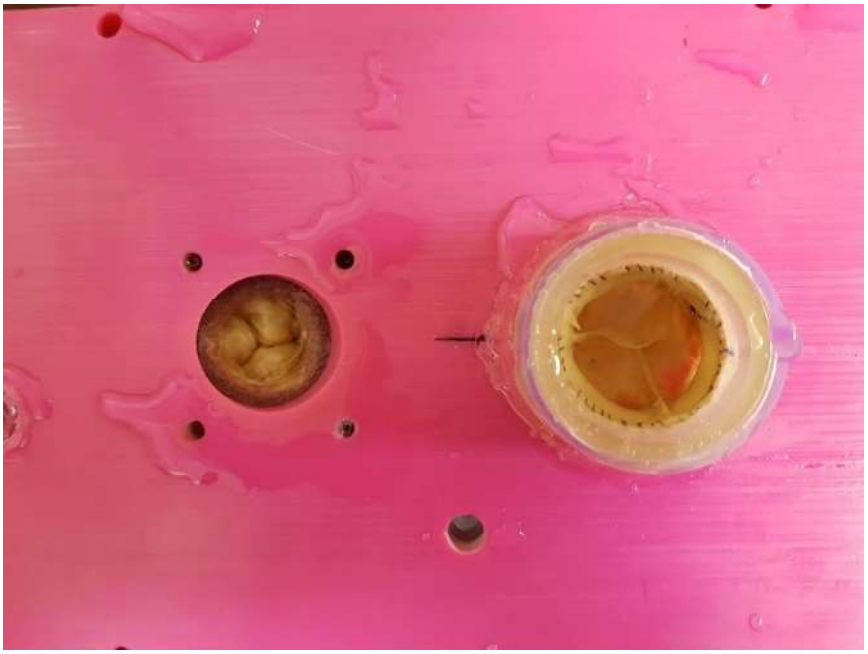

Figure 20: The biological valves were placed inside cylinders in the MCL lid. The orientation of the leaflets was chosen carefully and aligned with an indication on the lid. The mounting of an additional LVOT is possible on the left, where the AV is placed in a recess of the lid.

A 3/8in silicone tube was used as the outflow graft of the pump to transport flow over the LVAD to an aortic chamber, located just above the cylinder holding the aortic valve in place. This aortic reservoir was pressurized and contained a predetermined volume of air (~785ml) atop the contained liquid to act as the compliant component of the dynamic system, modelling the Windkessel effect of the Aorta. Another reservoir was used for the atrial chamber and kept open to atmospheric pressure. A ½-inch silicone tube was used to transport liquid from the aortic chamber to the atrial chamber, passing through a clamp that could be adapted to vary the peripheral resistance of the system. Pressure transducers (TruWave pressure transducers, Edwards Lifesciences LLC, Irvine, CA, USA) captured pressure signals during experiments and were connected at the ventricular chamber of the circulatory loop, as well as in the aortic and atrial chambers (Figure 21). Flow rates were captured via flow sensors (H9XL and HT110R, Transonic Sytems Inc., Ithaca, NY, USA) that were located at the outflow graft of the LVAD and the tube connecting the atrial and aortic chambers (Figure 21).

An aqueous Glycerol mixture (50%/50% by weight) was used in these experiments. The choice of 50% glycerol solution was due to the thickness of the model wall, as well as its

more complex structure, making exact index refraction matching necessary for PIV imaging. This mixture required heating the liquid inside the MCL to 35.5°C using a liquid heat exchanger, that was placed as a second parallel loop with in- and outflow at the atrial chamber, resulting in a viscosity of 3.72 cP, mimicking a hematocrit of 40%.

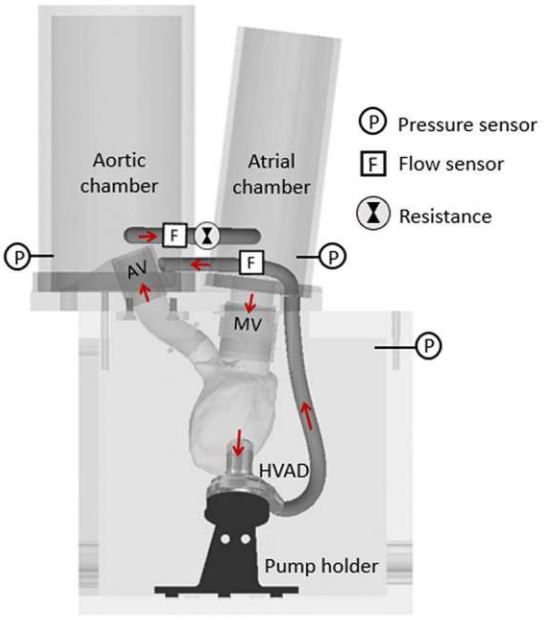

Figure 21: A schematic overview of the mock circulatory loop system and pressure and flow measurements performed. The LV model and HVAD are placed on a pump holder to prevent deformation of the model and allow accurate placement of a coordinate system. Two flow sensors are used to calculate the total cardiac output and LVAD flow. Pressure transducers placed in the Atrial and Aortic chambers, as well as in the box holding the LV are used to determine pressure.

3.4.2 Laser & Camera System

A double pulsed Neodym-yttrium-aluminum-garnet (Nd-YAG) laser (Litron Lasers Ltd, Rugby UK) was used in these experiments. The laser emits light at a wavelength of 1064µm, however the frequency can be increased through frequency doubling and signal separation to achieve a wavelength of 532µm, corresponding to green light in the visible light spectrum. The light beam is expanded into a roughly 4mm wide light sheet that can be aligned with the measurement object to create thin illuminating image planes in the desired direction. The light is scattered from tracer particles suspended in the model liquid inside the ventricular model and is then captured with a high speed CMOS camera (SpeedSense9020; Vision Research, NJ, USA). The double exposure required for PIV images was triggered with the laser pulses at a frequency of 100Hz. The camera has limited storage capacities with a maximum buffer size of about 750 image pairs. Data therefore has to be exported from the camera buffer to the software environment before it can be stored for later processing in the PIV image recording software. Time between pulses varied depending on the intraventricular velocity of the specific planes. The correct time between pulses was found through use of the “quarter displacement rule” [37].

3.5 Coordinate System Definitions

A global coordinate system was defined based on the placement of the model inside the MCL. The coronal midplane was defined to intersect the middle of the AV, MV and the center of the tip of the IC. The sagittal midplane was placed perpendicular to the coronal midplane, intersecting the center of the tip of the IC and the MV. Parallel planes were captured in 5mm steps.

The parallel planes were captured by moving either the camera, laser, mirrors in the optical setup, the platform carrying the MCL or a combination of these. The optical path length of the light from the image plane to the camera sensor was kept constant in this way, enabling the use of a single focus setting on the camera for purposes of simpler image calibration (Figure 23). Measurements performed in this way ensure that only a single plane has to be calibrated in the software to ensure correct calculation of the measured velocities. The positive coronal planes were recorded using two mirrors placed at 45° angles each behind the MCL, while the sagittal planes were recorded using a single mirror placed at a 45° angle next to the MCL. These coordinates were defined in the in-situ model and used for the modified model as well, since the position of the MV and AV did not change between the in-situ and modified models and the definition of the midplanes is based on these landmarks in the experimental setup.

.

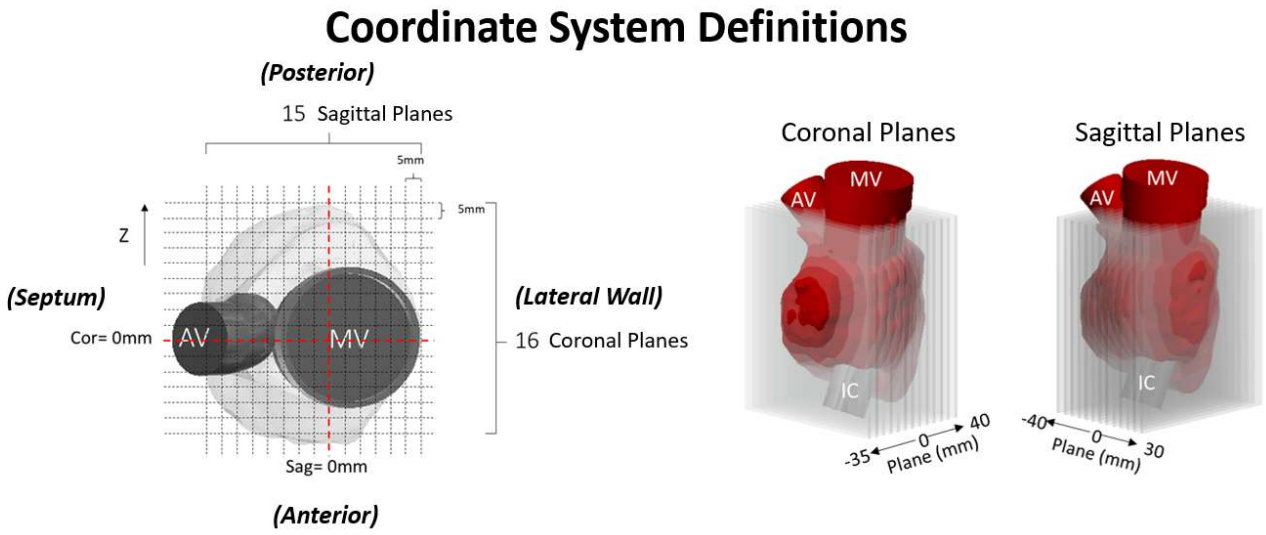

Figure 22: The definition of the global coordinate system used in both experiments. The coronal midplane (0mm) intersects the MV, the AV and the tip of the IC. The sagittal midplane (0mm) is orthogonal to the coronal midplane and intersects the MV and the center of the IC. Parallel planes were captured in 5mm steps from the midplane. This plane positioning and spacing was used in both experiments, as the position of the AV and MV was unchanged.

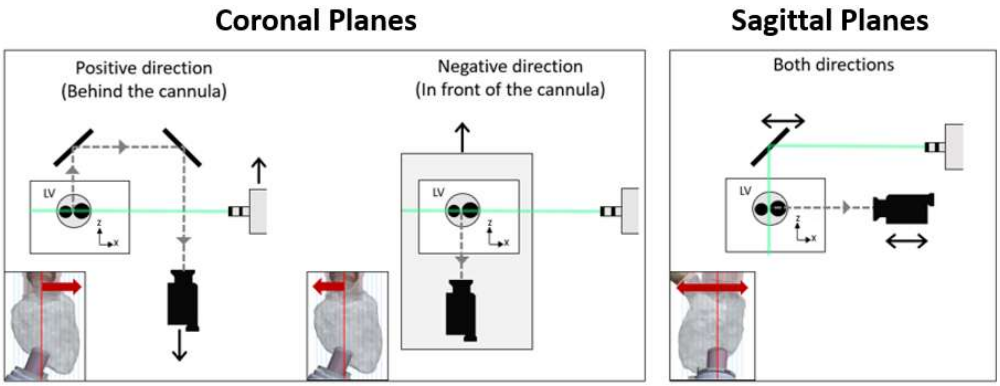

Figure 23: The camera setup utilizes moving the camera, laser, mirrors or even the optical setup to keep the optical path length constant between the imaging plane and the camera sensor when moving from plane to plane. Note that the red line represents a plane that is orthogonal to the view to illustrate the direction of the movement.

3.6 Apex of the Model and Apical Parameters

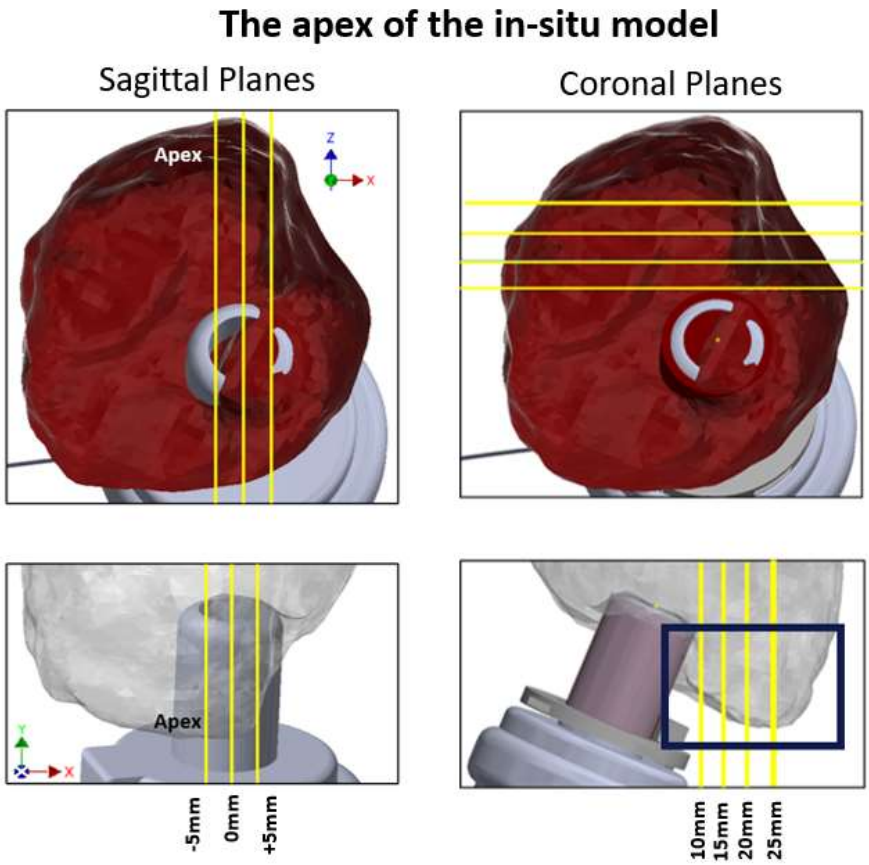

Figure 24: The apex of the LV model is located in the coronal planes 10mm to 25mm and in the sagittal planes -5mm to +5mm. The top images show a top-down view through the model, while the bottom images show orthogonal side views.

The apex of the in-situ model can be found in the coronal planes 10mm, 15mm, 20mm and 25mm, and the orthogonal sagittal planes -5mm, 0mm and +5mm (Figure 24). ROIs were defined in the apical parts of these planes to calculate local Pulsatility Index and Stagnation Index maps and compare the situations between the two models. Since the modified pump

position has the IC placed at the apex of the model the area of the apical ROIs are not identical, especially when the IC is located inside the defined ROI. A closer inspection of these critical areas can however still provide some insight into the altered flow resulting from the changed pump position and the overall position of the apex did not change between models.

Both the Stagnation Index and Pulsatility Index will be computed specifically in the apical subregion within the aforementioned planes, which will be presented in the Results section, (see Figure 38 and Figure 39).

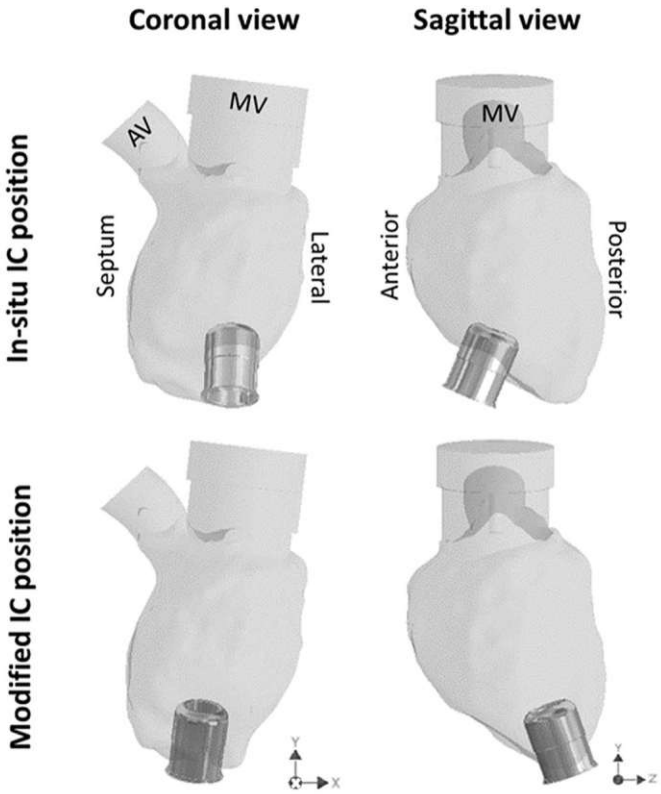

Figure 25: The two models can be seen in coronal and sagittal views. In the modified IC position the cannula faces the anterior wall of the LV and is nearly in-line with the MV-apical axis, placed at the apex of the LV.

3.7 Software

3.7.1 Data Capture & Data Processing

A MicroLabBox (CP1103 PPC Controller Board, dSPACE Inc., Paderborn, Germany) was used to enable synchronization of the optical system to the mock circulatory loop setup. Image acquisition was performed using DynamicStudio 3.14 (Dantec Measurement Technology A/S, Skovlunde, Denmark) and post-processing was performed in both DynamicStudio and MATLAB (MathWorks, Natick, MA, USA). For this purpose, the data was transferred to MATLAB via an export script in DynamicStudio, where it was saved as structured data for further analysis. During experiments the PIV system captures double frame images at a rate of 100Hz in the form of greyscale datasets for each timepoint.

After PIV acquisition post-processing starts directly in DynamicStudio where following steps are performed:

The scale factor of the image is defined by marking a known length in the image, such as the width of the IC, and inputting its length into DynamicStudios. This scale factor is calculated for every plane. An adaptive masking algorithm was applied, which removed areas outside of the LV walls in each step of the cardiac cycle.

Adaptive Correlation algorithms were then applied in DynamicStudio using interrogation windows of 32x32 pixels with 50% overlap to calculate the velocity fields. Hemodynamic data, which were captured during the experiments, are matched to specific image files to highlight possible interesting moments in a recording or measurement errors. The resulting velocity fields are then exported to MATLAB, where further calculations can be performed. The complete experimental results are collected in a structure that contains the data of all planes for the entire measurement duration. Results are computed by accessing substructures of these files in later steps. Adaptive masking was applied, which is described in more detail in T. Khienwad's thesis [35] in Chapter 7.1.4 Dynamic mask. Captured flow field data must be masked for proper correlation calculations, since moving particles close to the wall and outside of the model could be mistaken as intraventricular motion by the algorithm. This (automated) adaptive mask was used to assist in masking the large amounts of data produced during these experiments, which combined several algorithms available in DynamicStudio, such as thresholding and filters.

The automated wall detection algorithm resulted in a time-resolved mask that could be applied to each individual data set without the need to mask them by hand. An example of such a masked dataset can be seen in Figure 26 B).

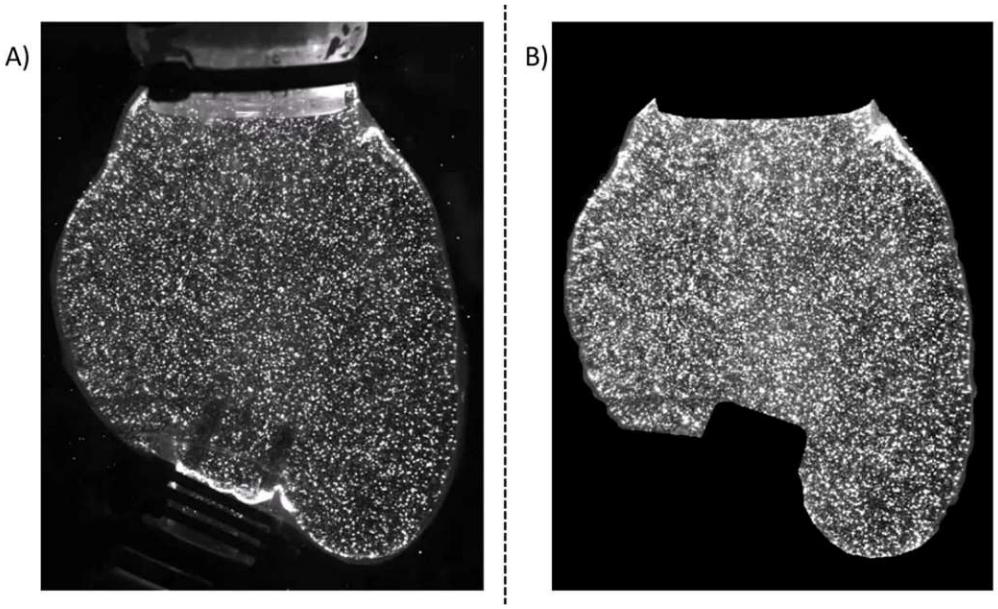

Figure 26: Adaptive masks were used to cut out the areas outside of the LV wall. A) Raw image captured during PIV experiments can be seen for a single frame. B) The same frame can be seen after automatic masking was applied. The "dynamic" nature of the mask is due to the moving walls of the model over time.

This entire experimental process was repeated for each experiment (Experiment 1: In-situ positon, Experiment 2: Modified Position) and was stored in separate file structures, due to size limitations resulting from the large amounts of data.

3.7.2 MATLAB Data Processing

The collected data is processed in MATLAB using structure arrays that contain the complete experimental data of an experiment in single files (for easier importing and data handling). The size of these files was around 16 GB for each experiment, which is therefore also the lower limit for RAM requirements to process these files in MATLAB. A single frame for a certain timepoint has a gridsize of 71*55 pixels, where the orthogonal vector components ***u*** and ***v*** are stored in each pixel, along with other essential information, such as the size of each singular grid step in every direction. The gridsize is a direct result of the interrogation area sizes and the corresponding scaling factor which is determined before analysis via known landmarks in the raw image, such as the width of the inflow cannula. The resulting velocity vectors can be calculated for each point of the image using these components.

Structure arrays enable storage of these components for each point in time and for each measured plane, using array indices that determine the plane of interest and the number of the frame in question. The total size of this array is 71x55x75x26x16, where 71x55 is the image size, 75x26 is the frame index and the beat index, and 16 is an identifier for the plane (or 15 for Sagittal).

Ensemble averages (Eq. 7) are calculated for each set of 71x55 pixels and timepoint (1 to 75), corresponding to 750ms long cardiac cycles, which are just a result of the chosen heart rate and time resolution of the image capture. These ensemble averages can then be used for time-resolved calculations of the ensemble average or mean value calculations of flow parameters.

4. Results

4.1 Hemodynamic Response

Experiment (48x7s data)	Contractility Setting	SV [ml]	Pump Speed [RPM]	Heart Rate [BPM]	Mean Aortic Pressure ± SD [mmHg]	Mean Preload ± SD [mmHg]	Mean CO ± SD [l/min]	Mean LVAD flow ± SD [l/min]	Mean aortic flow ± SD [l/min]
1) In Situ	*Patient Specific*	58	2650	80	86.9 ± 1.4	15.1 ± 0.4	5.3 ± 0.1	4.4 ± 0.2	0.9 ± 0.0
	Standard Partial Support	64	2430	80	82.2 ± 1.6	15.1 ± 0.4	5.1 ± 0.1	3.8 ± 0.2	1.4 ± 0.0
	Standard Full Support	35	2825	80	81.9 ± 0.1	15.5 ± 0.2	5.0 ± 0.1	5.0 ± 0.1	0.0 ± 0.0
2) Modified	*Patient Specific*	58	2680	80	85.4 ± 1.4	13.9 ± 0.3	5.1 ± 0.0	4.3 ± 0.2	0.8 ± 0.0
	Standard Partial Support	64	2480	80	80.9 ± 1.5	13.9 ± 0.3	4.9 ± 0.0	3.8 ± 0.1	1.2 ± 0.0
	Standard Full Support	35	2815	80	79.6 ± 0.3	14.0 ± 0.1	4.8 ± 0.0	4.8 ± 0.1	0.0 ± 0.0

Table 1: Mean Hemodynamic Parameters of responses recorded during 1) In-Situ position experiments and 2) Modified pump position experiments. Mean values are obtained by calculating the mean value over 48 recordings of 7s each, which were captured during image acquisition.

Both (in-situ and modified) PIV Experiments were performed for three different contractility settings: Patient Specific (58ml SV), Standard Partial Support (64ml SV) and Full Support (35ml SV). Mean values and standard deviation (SD) were computed by calculating the mean over 48 separate 7s long recordings (Table 1), which were captured during PIV image acquisition. The time-resolved hemodynamic response for each setting can be found in Figure 27 (in-Situ) and Figure 28 (Modified) for both experiments for 3 second windows. The two separate experiments (In Situ and Modified pump position) produced similar responses, though slightly adjusted to achieve the necessary total CO of 5 l/min. The Full Support setting (SV35) was selected to investigate situations where the entire outflow of the ventricle is transported by the pump. In that case aortic flow is zero and consequently, aortic valve opening does not occur. The Patient Specific setting (SV58) corresponds to a Partial Support setting, where nonzero aortic flow occurs, with hemodynamic parameters matching those that were captured around the time of CT acquisition. An additional Partial Support setting with increased stroke volume was also chosen (SV64).

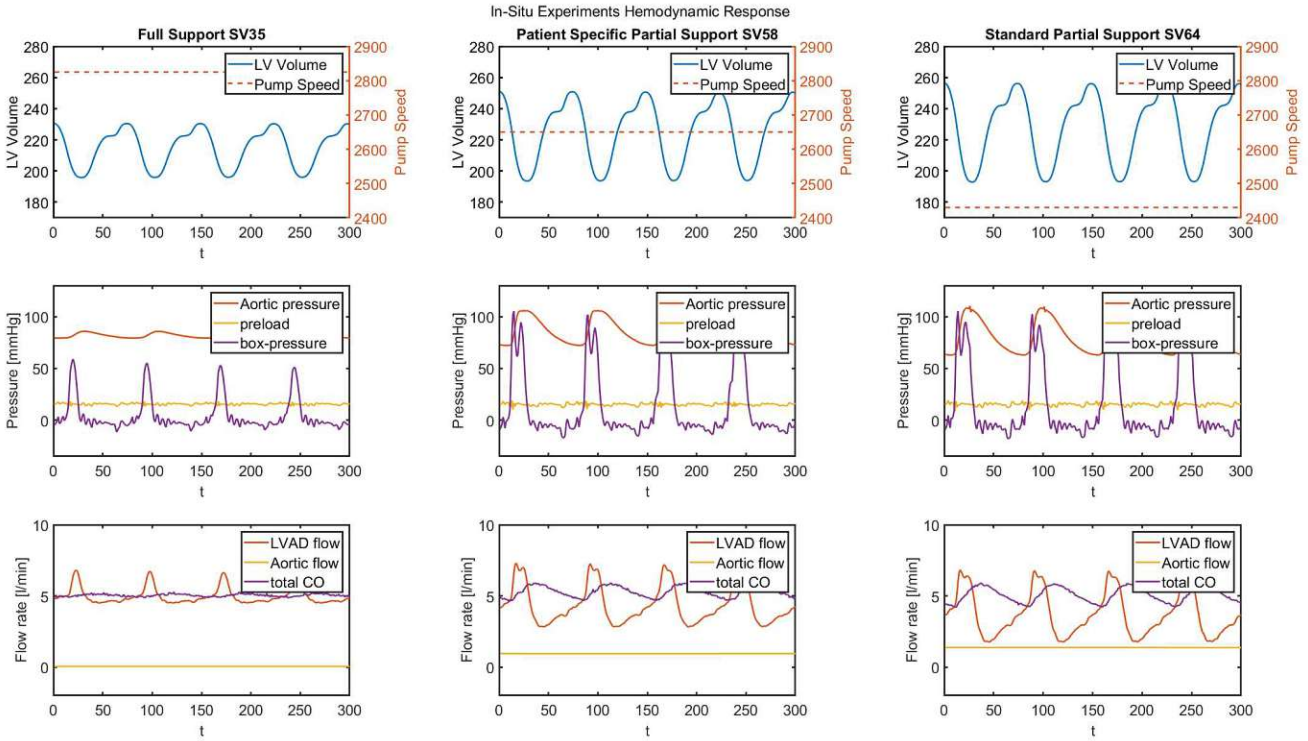

Figure 27: Hemodynamic Responses for the in-Situ pump position experiments. 3s of data are presented here.

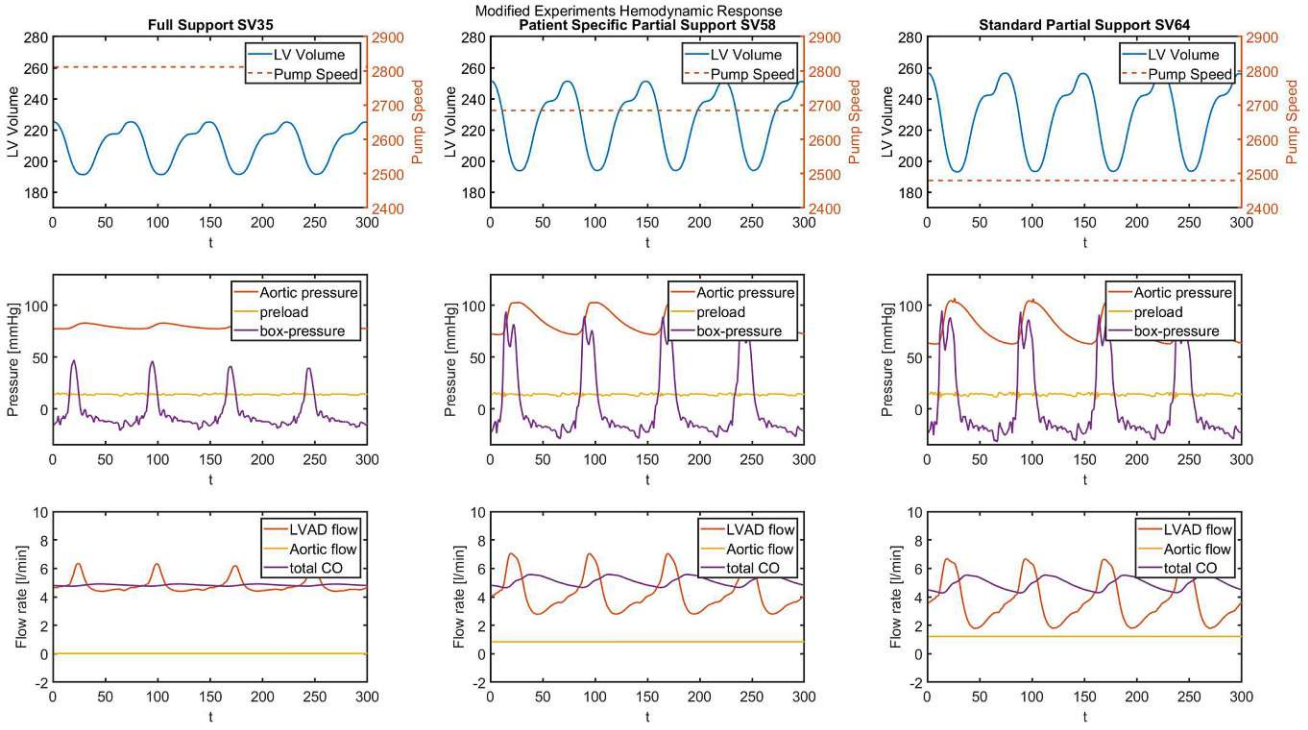

Figure 28: Hemodynamic Responses for the Modified pump position experiments. 3s of data are presented here.

4.2 Velocity Field Analysis

The intraventricular flow fields exhibit characteristic LV flow under LVAD support in all cases, with a diastolic inflow jet traveling toward the IC at the apex and characteristic

clockwise and counter-clockwise vortices appearing on either side of the jet (vortex ring). In the Full Support setting, the complete cardiac output is transported via the LVAD outflow, with the aortic valve remaining closed for the entire measurement duration. Mean aortic flow is nonzero in the other (Partial Support and Patient Specific) contractility conditions, meaning there is opening of the AV and flow through the valve and LVOT.

The captured intraventricular flow fields are presented here for the patient specific contractility setting (58ml SV), while the flow fields and velocity related parameters of the additionally captured settings can be found in the Appendix.

Mean velocity fields for every plane are presented in this section, along with the results of close-up investigations of the apical ROI in each model.

4.2.1.1 In-situ pump position:

The intraventricular mean velocity flow fields for the in-situ pump position and patient specific contractility settings can be seen in Figure 29 (Coronal planes) and Figure 30 (Sagittal planes), along with the mean velocity calculated over the flow field for each plane. The captured flow fields show characteristics of LV flow under LVAD support in all configurations, including a diastolic jet that travels toward the apex of the LV that is accompanied by clockwise and counterclockwise vortices on both sides of the jet. In this contractility setting systolic ejection of flow occurs via both the LVAD and AV (mean LVAD flow: 3.8 l/min; mean AV flow: 1.2 l/min).

The mean velocity fields of the coronal planes show a distinct inflow jet travelling from the MV to the apex of the model. The angle of the IC is not aligned with the travel direction of the jet. The mitral jet can be seen in all planes between -25mm and +15mm due to the increased mean velocity along itmain pathway. Characteristic vortices can be seen around the midplane and surrounding planes.

The apex of the in-situ model, which is closer defined via ROIs in Figure 24, can be seen in the coronal planes 10mm to 25mm and in the sagittal planes -5mm to +5mm. In the coronal view these planes show that only a small part of the inflow jet was directed towards the apex, with large velocity increases visible between Coronal planes -20mm and 5mm in the center of the flow field.

In the sagittal view the apex is more clearly visible and parts of the vortex ring of the mitral jet seems to reach into the apex itself, however there is a distinct low velocity region in planes 0mm and 5mm and no vortex to increase flow velocity in this region. There seems to be flow around the cannula, though it is of relatively low velocity. The distribution of mean velocities in the Coronal view has a peak at the -15mm plane (mean velocity: 139mm/s) and minima around the planes where the apex is defined (10mm to 25mm, minimum mean velocity: 73mm/s). The Sagittal view shows more normal distribution with a peak around the 5mm plane (122mm/s). In a later section, the results of the apical analysis will provide more insight into these critical areas.

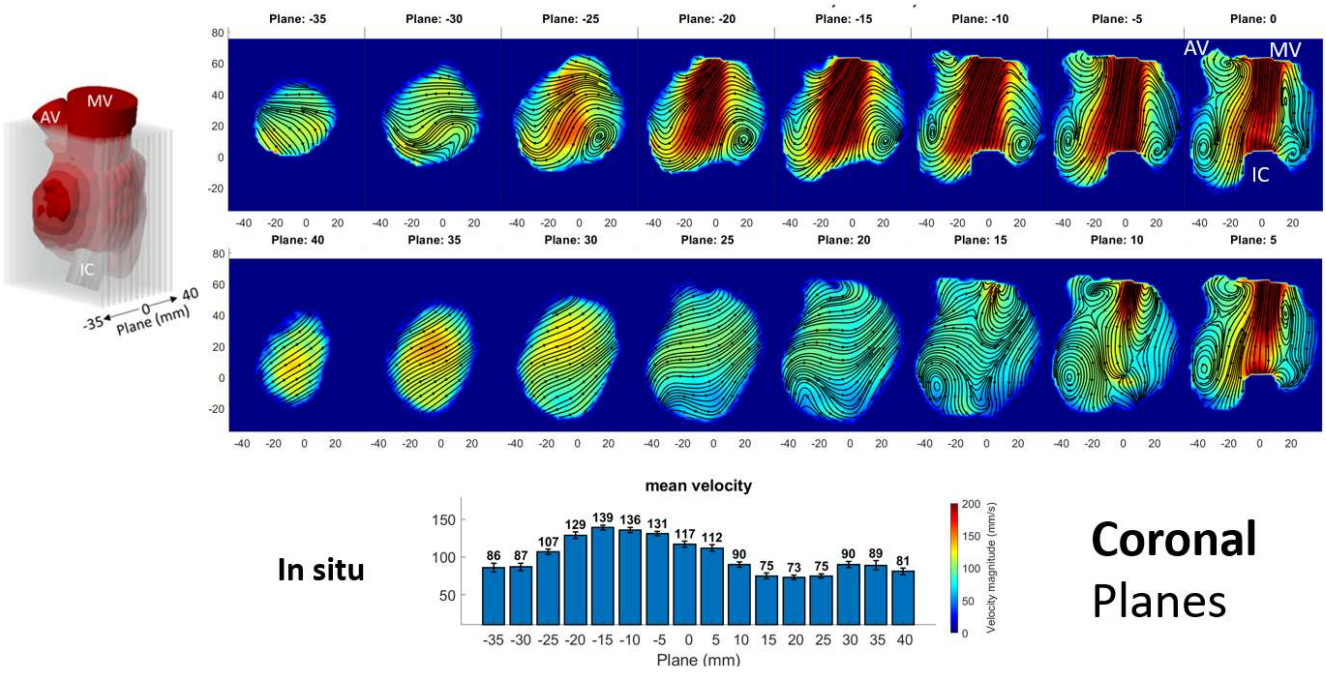

Figure 29: Mean velocity fields of Coronal Planes for the in-situ pump position and patient specific contractility settings (58ml SV). The bar plot shows the mean velocity calculated over the entire field for each plane.

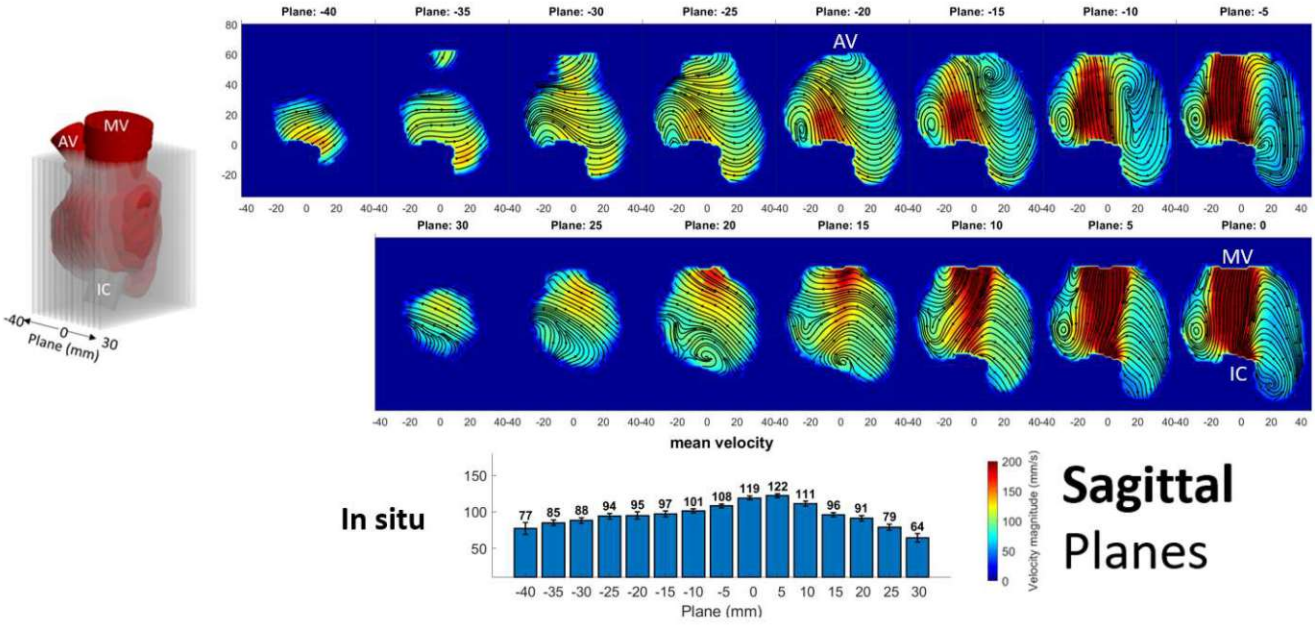

Figure 30: Mean velocity fields of Coronal Planes for the in-situ pump position and patient specific contractility settings (58ml SV). The bar plot shows the mean velocity calculated over the entire field for each plane.

4.2.1.2 Modified pump position:

The intraventricular mean velocity flow fields for the modified pump position and patient specific contractility settings can be seen in Figure 31 (Coronal planes) and Figure 32 (Sagittal planes), along with the mean velocity calculated over the entire flow field in each plane.

Note that the LVAD is located in different planes due to a lateral displacement toward the negative direction (coronal view). It is also angled toward the direction of the mitral jet (in the coronal view, Figure 25). The exact same definition for the plane positions is used in both models (see Figure 22, Coordinate System Definitions), so the position of the MV and AV are identical in both experiments. Only the IC position is changed.

As mentioned previously, the intraventricular flow fields exhibit characteristic flow expected from LVAD supported LVs, including the occurrence of a transmitral jet with characteristic vortices on both sides. The right side vortex in the coronal midplane (and close surrounding planes) is significantly larger than the left side vortex. Planes 30mm to 15mm show the position of the IC in the modified configuration along with parts of the mitral inflow jet, that appear to transport their characteristic vortices to the sides of the cannula (especially in planes 15mm, 20mm and 25mm).

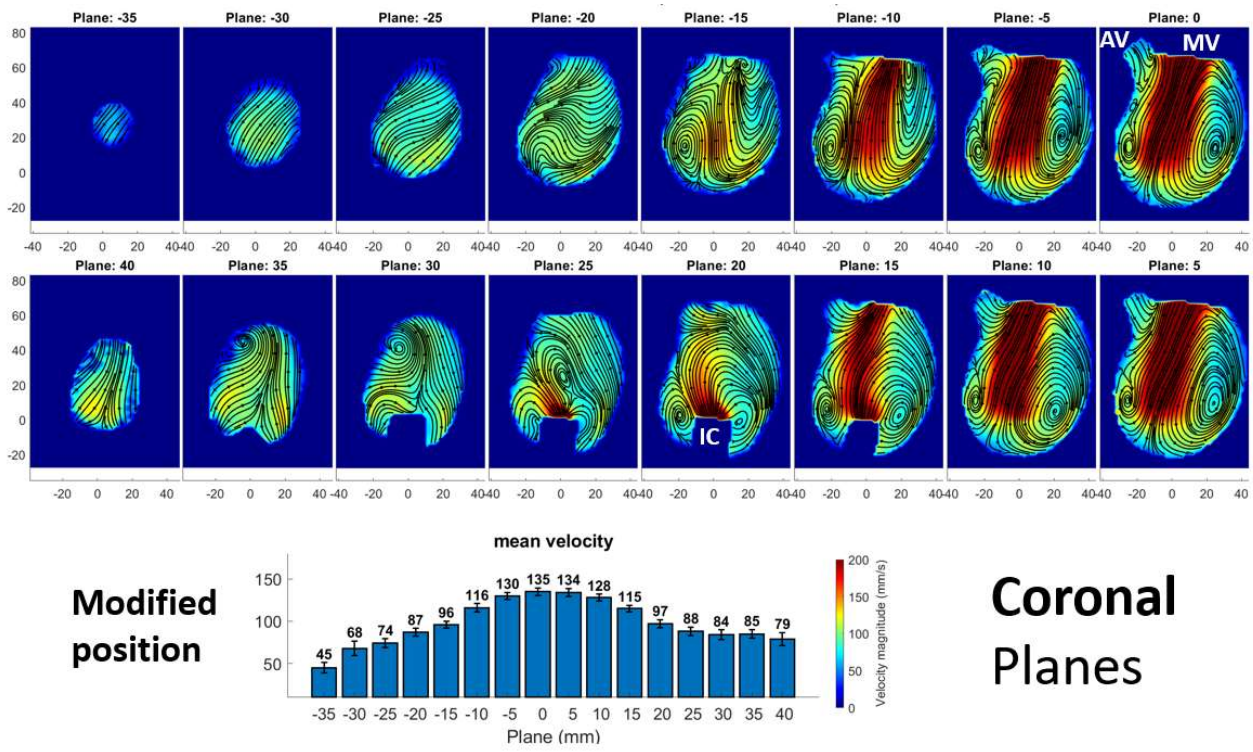

*Figure 31: Mean velocity fields of **Coronal** Planes for the **modified** pump position and **patient specific contractility** settings (58ml SV). The bar plot shows the mean velocity calculated over the entire field for each plane.*

The sagittal view of the modified LVAD position (Figure 32) shows how the mitral jet is transported to the apex, which is located in the Sagtittal planes of -5mm, 0mm and 5mm (Figure 24), with a large vortex visible in the sagittal midplane, toward the lower right side of the flow field. The mean velocities in both views seem nearly normally distributed, with a peak at either the Cor 0mm (mean velocity: 135mm/s) or Sag -5mm (mean velocity: 141mm/s) position and generally decreasing values toward either side of the model. Note that the planes containing the apex show higher mean velocities than in the in-Situ model.

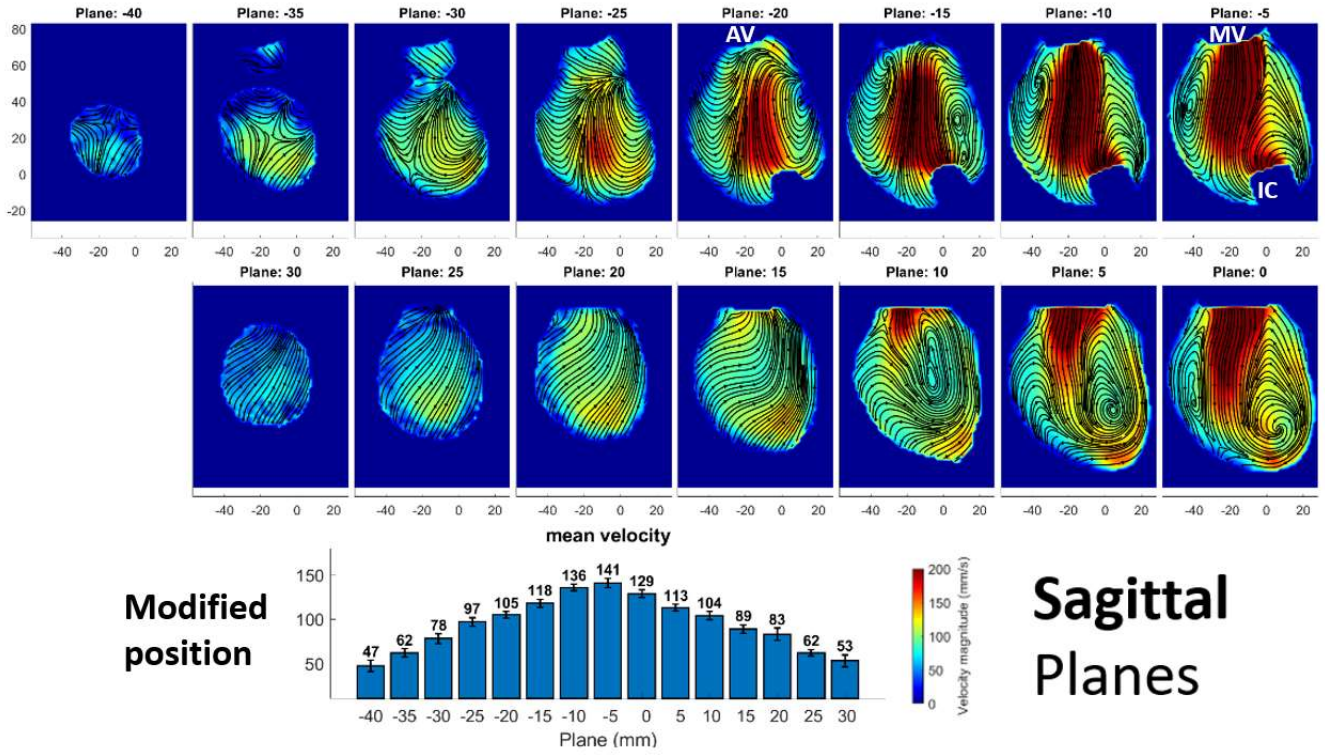

*Figure 32: Mean velocity fields of **Sagittal** Planes for the **modified** pump position and **patient specific contractility** settings (58ml SV). The bar plot shows the mean velocity calculated over the entire field for each plane.*

The apex of the Sagittal planes is located in the planes -5mm to 5mm and in this case a part of the IC can be seen in plane -5mm. The vortex of the jet can be seen reaching the apical area and some smaller regions of higher velocity flow appear close to the apex. The mean velocity distribution shows a peak at -5mm with nearly normal distribution around this value.

A 3D reconstruction of this flow behavior can be seen for both models in Figure 33 with four distinct time points selected during both Systole and Diastole. Comparing the Mid diastolic timing between models it is clear that the mitral jet travel direction and IC angle are not as well aligned as they are in the Modified position.

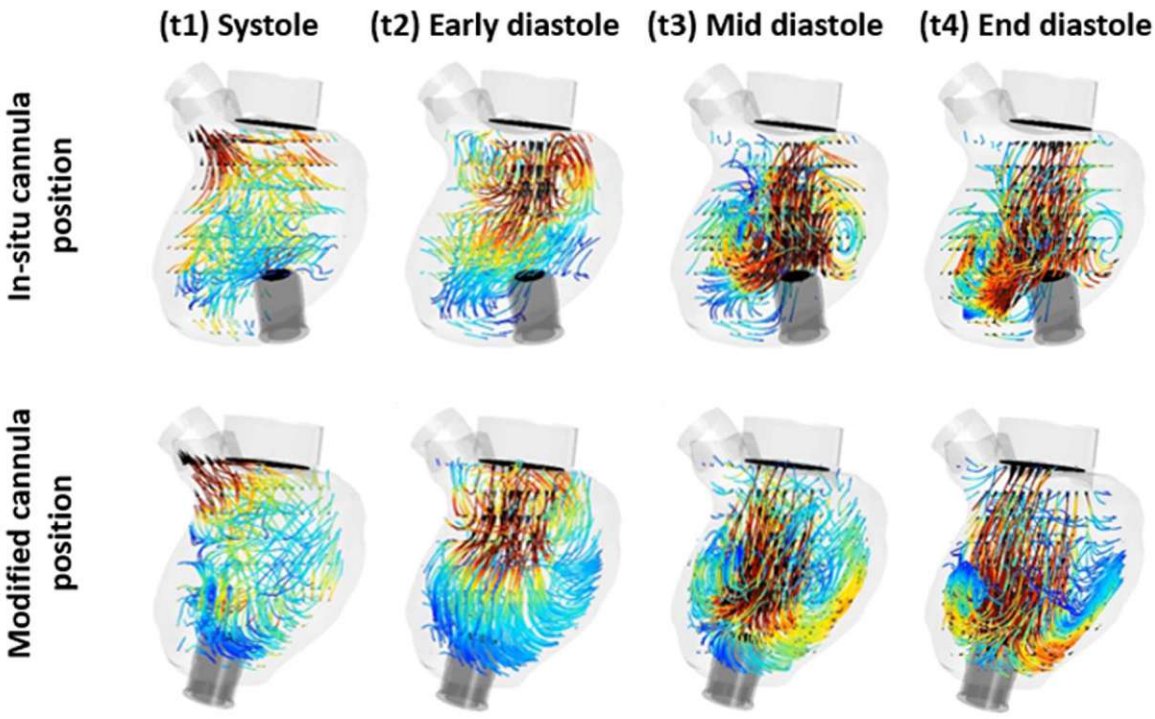

Figure 33: A three dimensional reconstruction (interpolation) can be seen here for both pump positions at four different time points. (t1) Systole, (t2) Early diastole, (t3) mid diastole and (t4) end diastole. The interaction between the mitral jet and the inflow cannula of the LVAD seems to play a role in determining the effectiveness of apical washout via the inflow jet

4.3 Stagnation Analysis

4.3.1.1 In-situ pump position:

The mean SI analysis of both Coronal (Figure 34) and Sagittal (Figure 35) views shows the mean stagnation over all captured planes. High stagnation is visible in the apex of the model in both views. Additionally, regions close to the walls of the model, where the mean velocities were reduced, show increased mean SI values as well. Along the pathway of the transmitral jet, mean SI was strongly decreased. The distribution of mean SI values calculated over every plane shows nearly uniform distribution of mean SI values across the entire model.

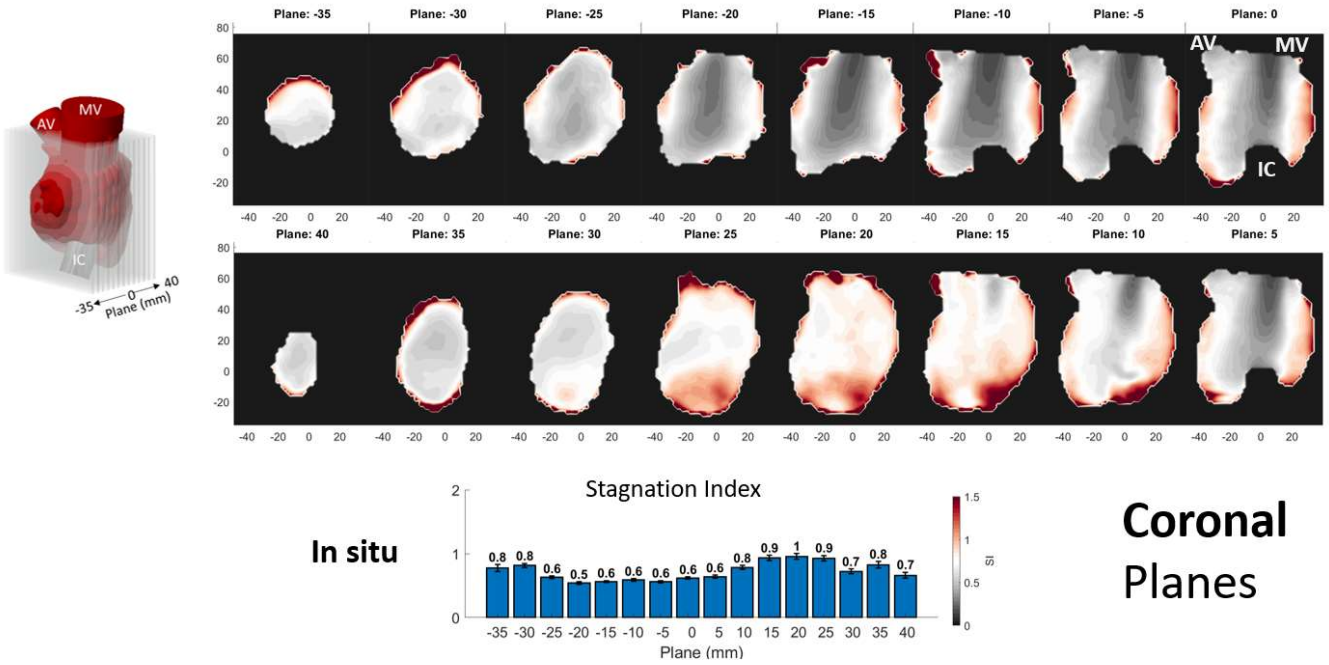

*Figure 34: Stagnation Index analysis of the **Coronal** planes for the **in situ** pump position and **patient specific contractility** settings (58ml SV). The bar plot shows the mean SI value calculated over each plane.*

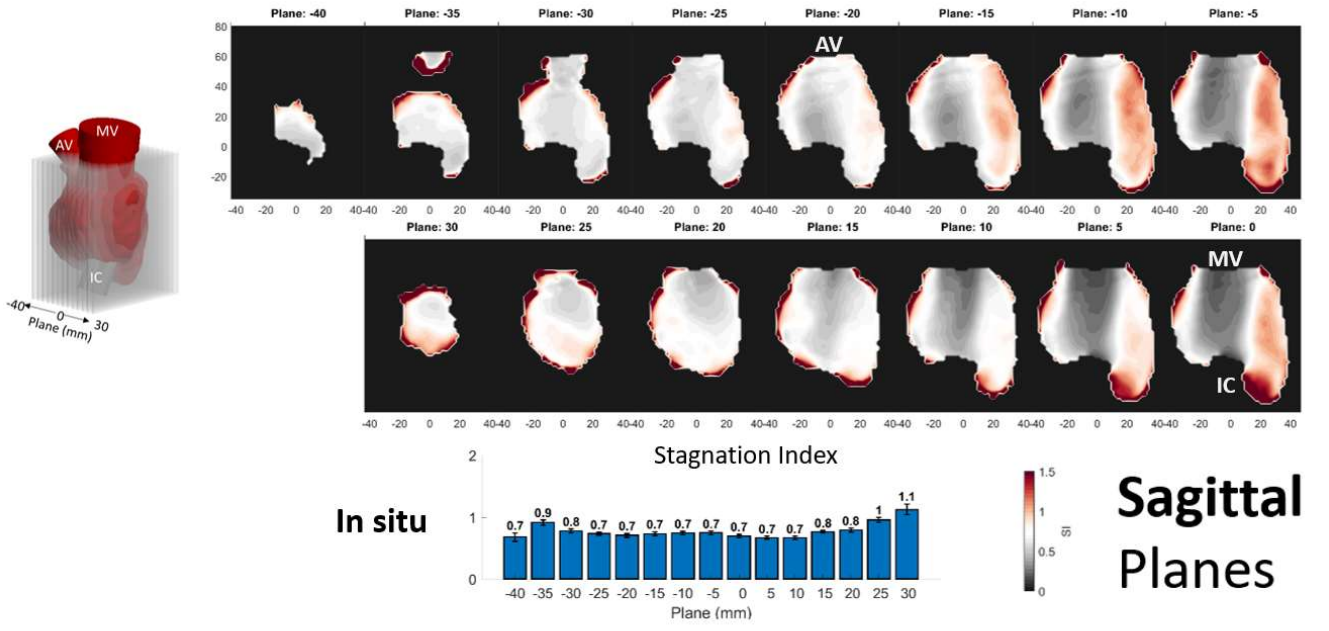

*Figure 35: Stagnation Index analysis of the **Sagittal** planes for the **in situ** pump position and **patient specific contractility** settings (58ml SV). The bar plot shows the mean SI value calculated over each plane. An area of high stagnation is visible on the right side of the IC, especially in the apex of the LV.*

4.3.1.2 Modified pump position:

The mean SI results for the modified pump position are shown for Coronal (Figure 36) and Sagittal (Figure 37) views. Though the critical regions around the apex of the in situ model show improvements in mean SI, the distribution of SI values over all planes seems to be less uniform than in the in situ model. The regions of high stasis in the apex appear strongly diminished in comparison.

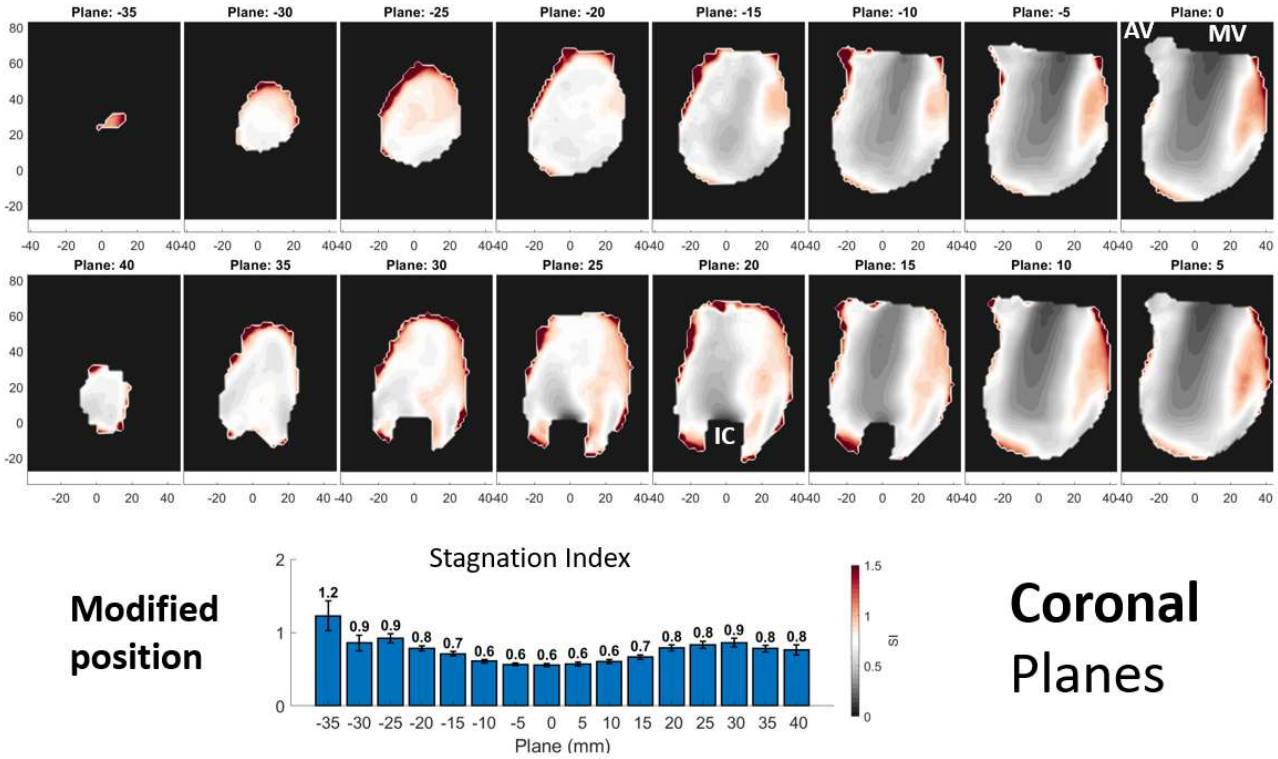

*Figure 36: Stagnation Index analysis of the **Coronal** planes for the **modified** pump position and **patient specific contractility** settings (58ml SV). The bar plot shows the mean SI value calculated over each plane.*

In the Coronal view the apical stagnation is reduced on the right side of the IC, yet the left side of the IC shows remaining areas of high stagnation.

In the Sagittal view the high stagnation regions located inside the in-situ model's apex are no longer visible.

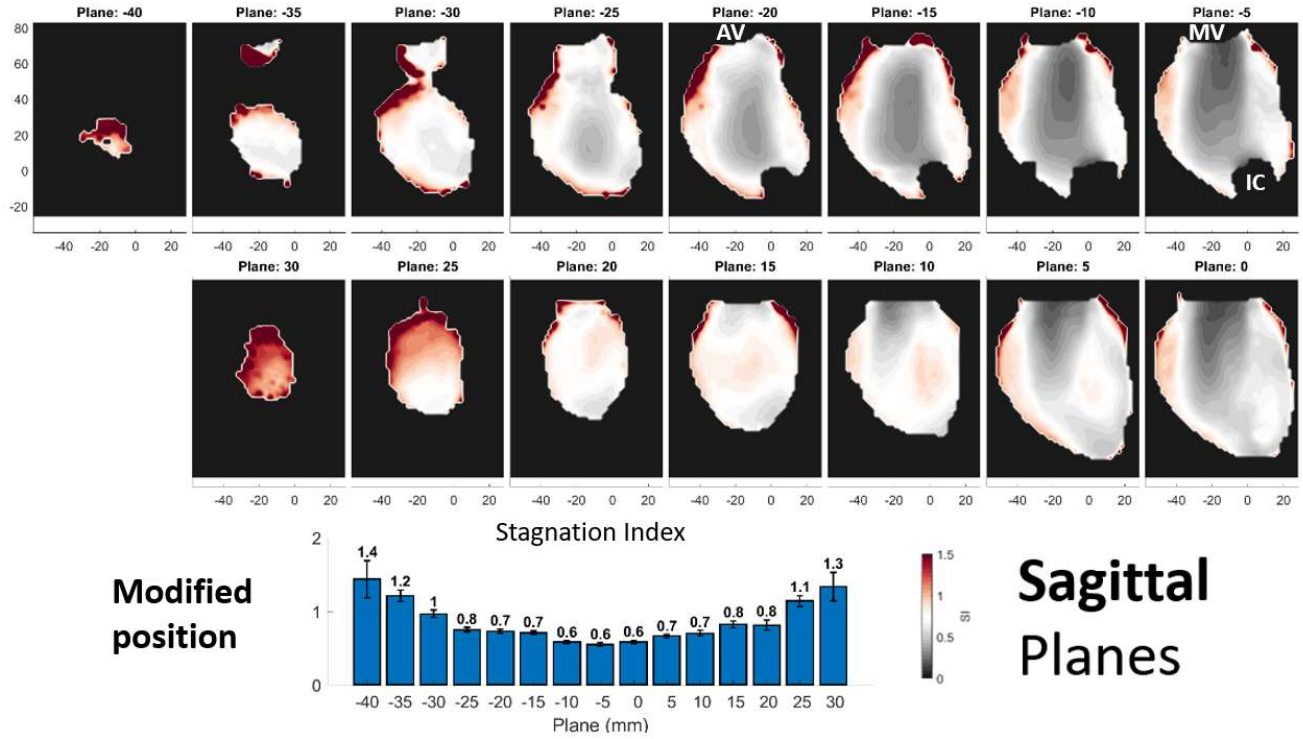

*Figure 37: Stagnation Index analysis of the **Sagittal** planes for the **modified** pump position and **patient specific contractility** settings (58ml SV). The bar plot shows the mean SI value calculated over each plane.*

4.3.1.3 ROI Calculations:

Seven ROIs were selected, corresponding to the apical region of the model and the mean SI, its standard deviation (SD) and median SI values were calculated for comparison between both pump configurations (Figure 42). These ROIs are highlighted in Figure 38 and Figure 39 for the in-Situ model and in Figure 40 and Figure 41 for the Modified model. Table 2 shows the collected results for all working points, with the Patient Specific contractility setting (SV58) highlighted in blue.

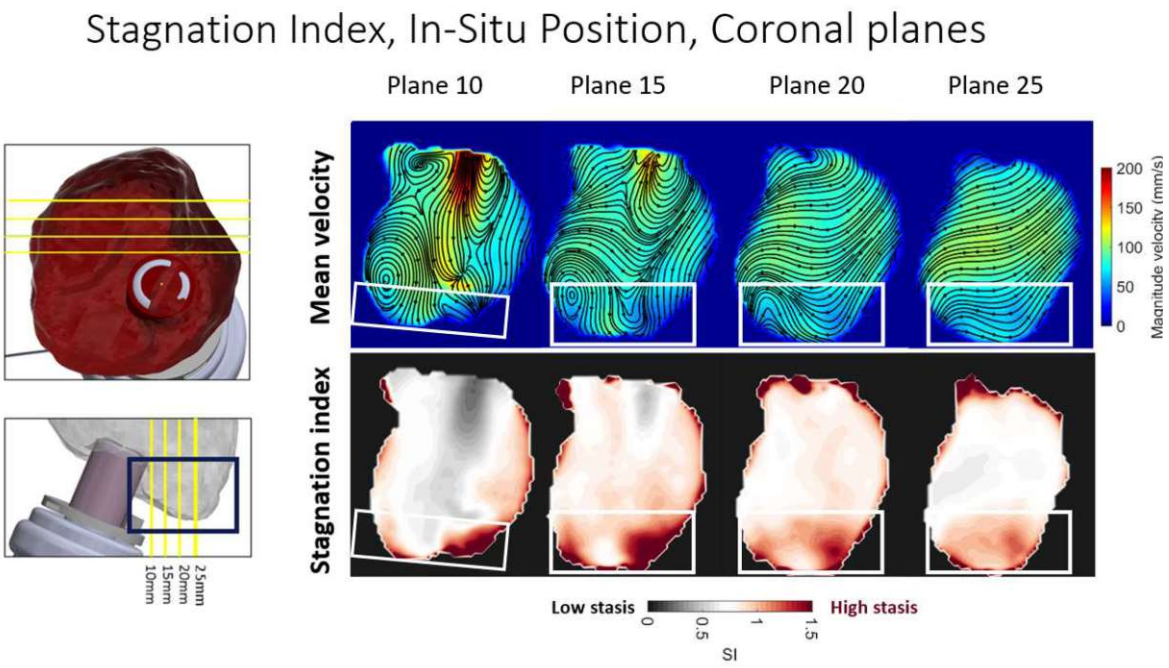

Figure 38: Results of SI analysis for the in-situ pump position at the apical region of the model for the Patient Specific contractility settings (SV58). The apical ROI used in PI and SI calculations is shown as a white box. High stagnation can be seen due to poor washout at the apex and close to the wall, especially at the bottom and top of the model..

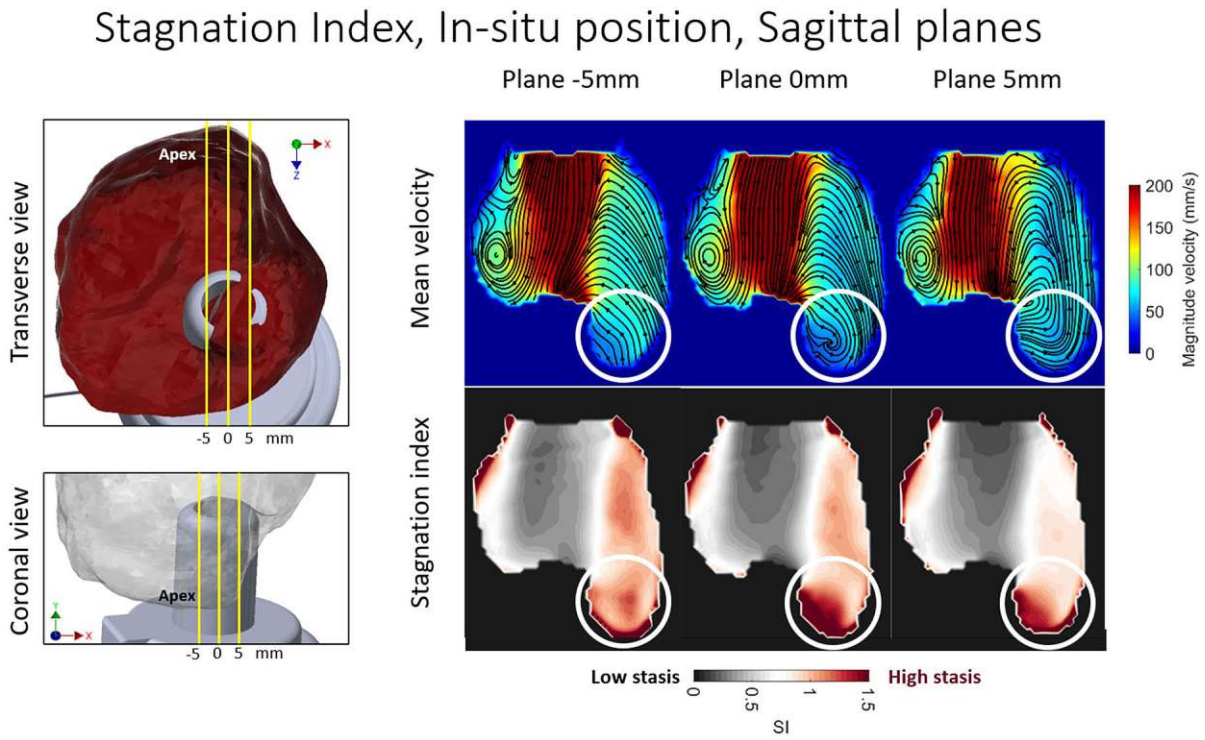

Figure 39 Results of SI analysis for the in-situ pump position in the sagittal planes where the apex is visible for the Patient Specific contractility settings (SV58). The apical ROI used in PI and SI calculations is shown as a white box. Similar to the coronal view high stagnation was observed due to poor washout of the apex in these planes.

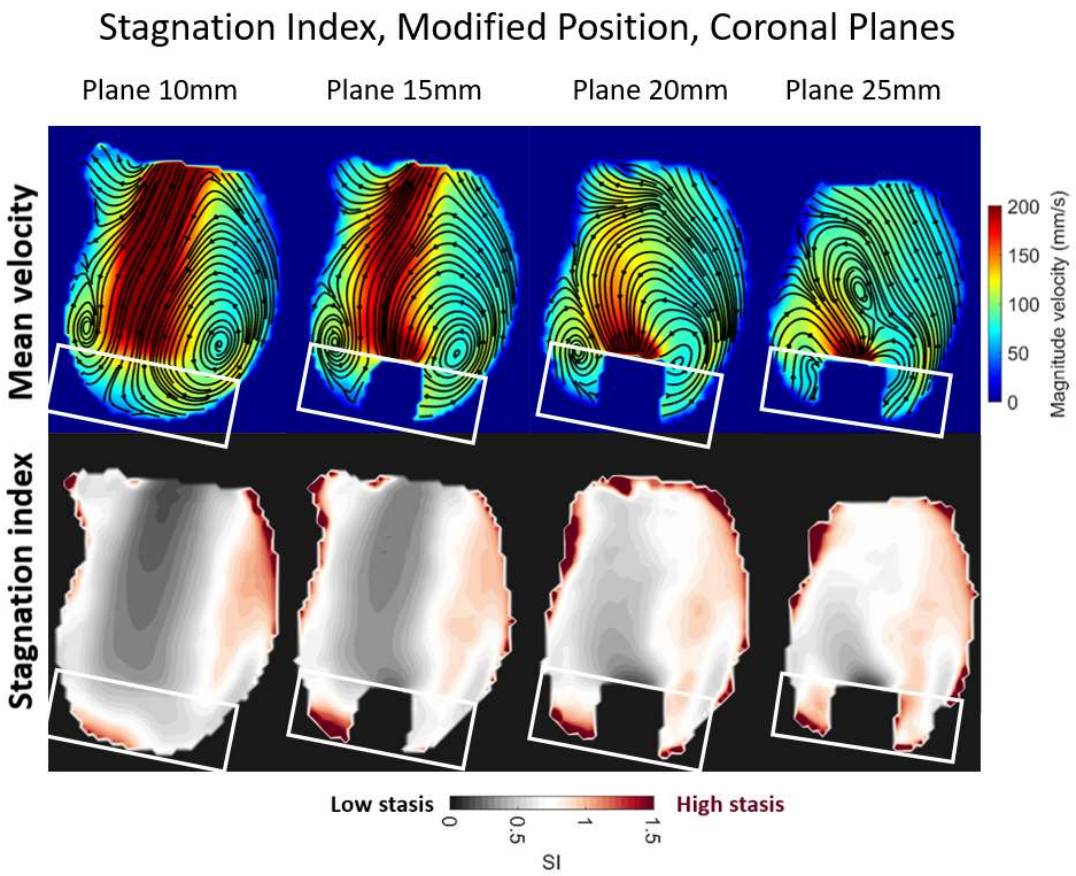

Figure 40: The modified pump position apex as seen in Coronal planes for the Patient Specific contractility settings (SV58). The apical ROI used in apical parameter calculations is shown as a white box. Some stagnation is visible in these regions, especially close to the IC and left side of the apex, though it is visibly reduced when compared with a similar ROI in the in-situ model.

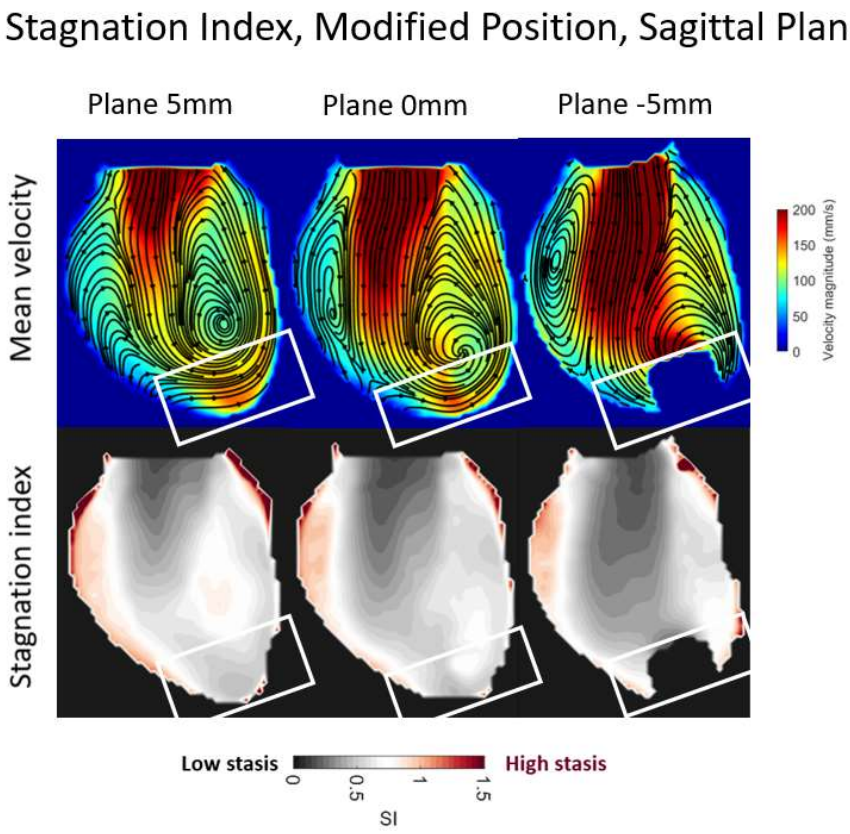

Figure 41: The modified pump position apex as seen in Sagittal planes 5mm, 0mm and -5mm for the Patient Specific contractility settings (SV58). The apical ROI used in PI and SI calculations is shown as a white box. There is no visible stagnation in the ROI, except for small regions along the wall, however it is strongly reduced when compared to the problematic apical area of the in-situ model.

Apical ROI				SI In- Situ Model			SI Modified Model		
Side	Plane	Support Type	Stroke Volume	mean SI	median SI	SD	mean SI	median SI	SD
Sag	-5mm	Full Support	SV35	0.63	0.53	0.24	0.38	0.25	0.12
		Patient Specific	SV58	0.66	0.57	0.16	0.31	0.22	0.12
		Standard Partial Support	SV64	0.73	0.67	0.12	0.31	0.23	0.09
	0mm	Full Support	SV35	0.69	0.62	0.11	0.44	0.23	0.09
		Patient Specific	SV58	0.66	0.71	0.07	0.40	0.22	0.09
		Standard Partial Support	SV64	0.74	0.85	0.05	0.34	0.24	0.04
	5mm	Full Support	SV35	0.61	0.49	0.31	0.57	0.23	0.22
		Patient Specific	SV58	0.59	0.54	0.24	0.47	0.21	0.15
		Standard Partial Support	SV64	0.65	0.60	0.18	0.44	0.23	0.14
Cor	25mm	Full Support	SV35	0.51	0.38	0.21	0.61	0.48	0.19
		Patient Specific	SV58	0.48	0.43	0.12	0.45	0.35	0.11
		Standard Partial Support	SV64	0.54	0.48	0.11	0.45	0.40	0.09
	20mm	Full Support	SV35	0.63	0.51	0.15	0.64	0.41	0.17
		Patient Specific	SV58	0.58	0.45	0.15	0.58	0.37	0.17
		Standard Partial Support	SV64	0.66	0.53	0.13	0.55	0.40	0.14
	15mm	Full Support	SV35	0.58	0.39	0.02	0.42	0.31	0.19
		Patient Specific	SV58	0.56	0.46	0.11	0.39	0.27	0.16
		Standard Partial Support	SV64	0.67	0.55	0.10	0.36	0.28	0.10
	10mm	Full Support	SV35	0.66	0.46	0.28	0.46	0.36	0.14
		Patient Specific	SV58	0.73	0.56	0.28	0.41	0.30	0.11
		Standard Partial Support	SV64	0.77	0.62	0.26	0.41	0.31	0.10

Table 2: Stagnation index calculations inside the apical ROIs. Mean SI, the standard deviation (SD) and median SI are presented for each model and the selected ROIs and each experimental setting. The blue highlight shows the Patient Specific contractility setting, as presented in the previous results. An average reduction of 19% of the mean SI was observed in the modified model's ROI when compared to a similar ROI in the in-situ model (mean relative change over all ROIs) and median SI is also reduced by 34%.

When comparing the Patient Specific setting in Table 2 it is clear that stagnation is improved in the apex of the modified model: The mean SI is decreased by 27.8% on average in these apical ROIs between both models for patient specific contractility settings. Merely one case showed unchanged mean SI values between both models: Cor +20mm (In Situ: mean SI=0.58; Modified: mean SI=0.58).

The comparison in apical stagnation for the seven selected planes and apical ROIs for the Patient Specific contractility setting alone are presented as bar plots in Figure 42.

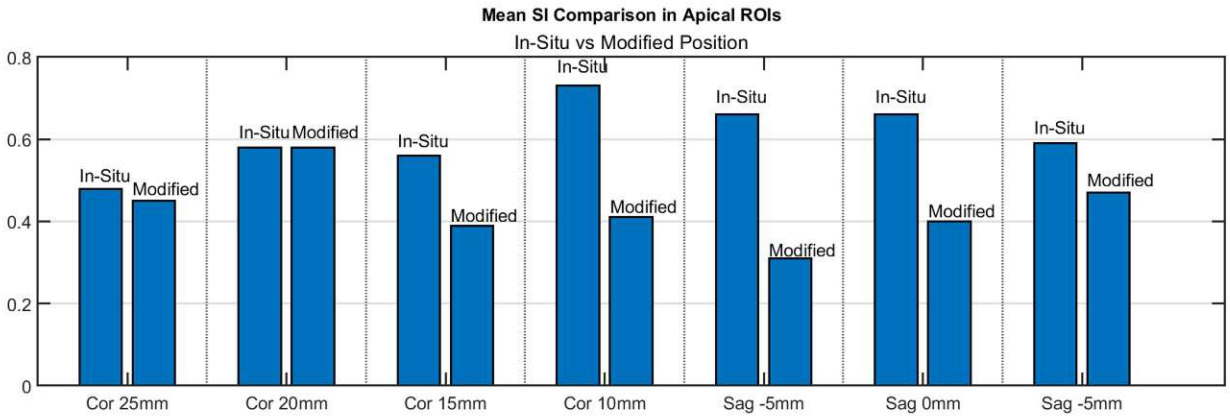

Figure 42:Comparison of mean SI value within the apical ROI for the two experiments. In all cases SI except Coronal plane +20mm stagnation was lower in the apical ROIs defined in the Modified position. The data is presented in Table 2

4.4 Pulsatility Analysis

4.4.1.1 In-situ pump position:

The mean Pulsatility Index was also calculated for all planes in both Coronal (Figure 43) and Sagittal (Figure 44) views. High pulsatility is observed at the Left Ventricular Outflow Tract (LVOT) close to the AV and along the transmitral jet pathway. At the apex of the model low pulsatility can be seen along the right side of the wall in the Coronal view, while the left side shows a slightly increased mean PI. In the Sagittal view, especially at the region of the apex pulsatility appears to be diminished in a large region to the right side of the IC.

Especially in the Sagittal view the apical pulsatility appears low due to the direction of the mitral jet pathway in planes -5mm to 5mm. It appears the mitral jet is not transported to the apical region in this model, resulting in decreased pulsatility in this region.

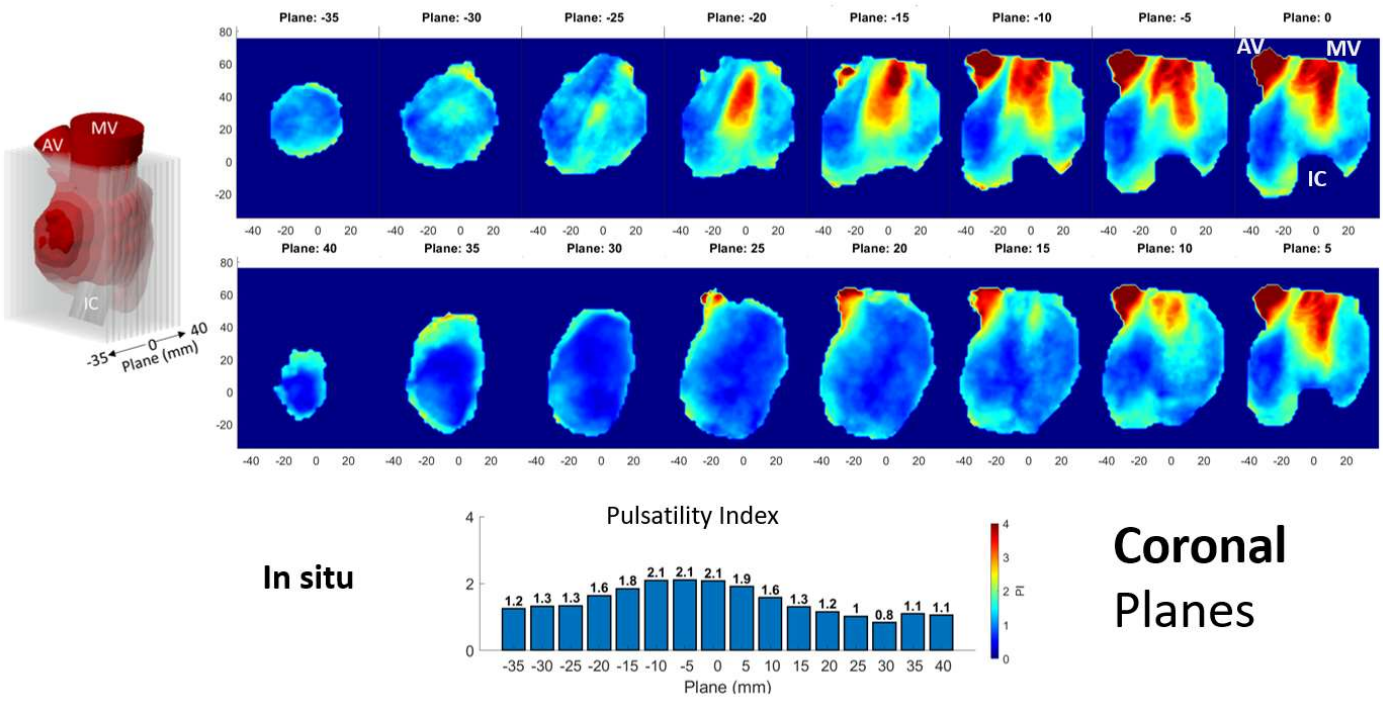

*Figure 43: Pulsatility Index analysis of the **Coronal** planes for the **in situ** pump position and **patient specific contractility** settings (58ml SV). The bar plot shows the mean PI value calculated over each plane.*

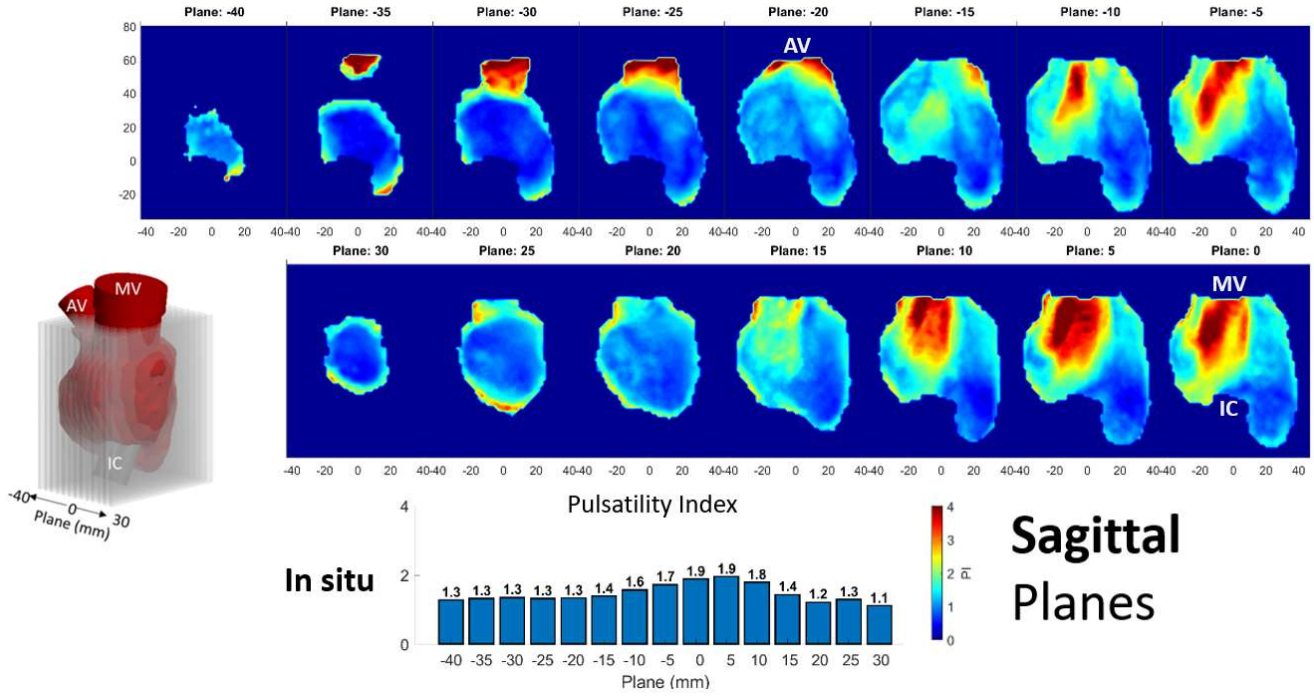

*Figure 44: Pulsatility Index analysis of the **Sagittal** planes for the **in situ** pump position and **patient specific contractility** settings (58ml SV). The bar plot shows the mean PI value calculated over each plane.*

4.4.1.2 Modified pump position:

The mean PI analysis for the modified pump position can be seen in Figure 45 (Coronal planes) and Figure 46 (Sagittal planes). Increased mean PI was observed in the apical region, especially toward the right side of the inflow cannula in the modified position. The distribution of mean PI values appears to be more normally distributed around the midplane in the Coronal view and around the -5mm to -10mm plane in the Sagittal view. When compared to the mean PI analysis of the in situ position the pulsatility along the transmitral jet is influenced by the pump position, as the modified position results in a narrower region of high PI around the pathway of the jet.

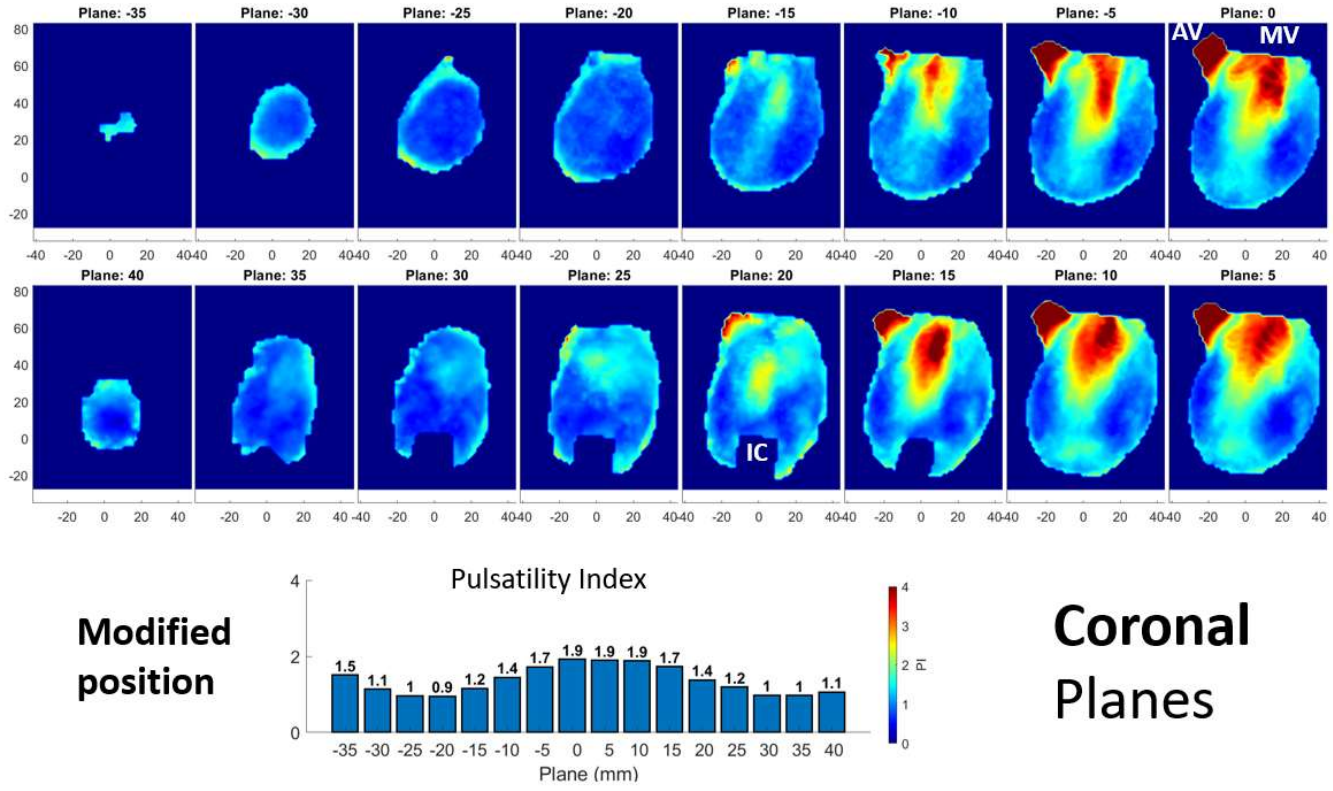

*Figure 45: Pulsatility Index analysis of the **Coronal** planes for the **modified** pump position and **patient specific contractility** settings (58ml SV). The bar plot shows the mean PI value calculated over each plane.*

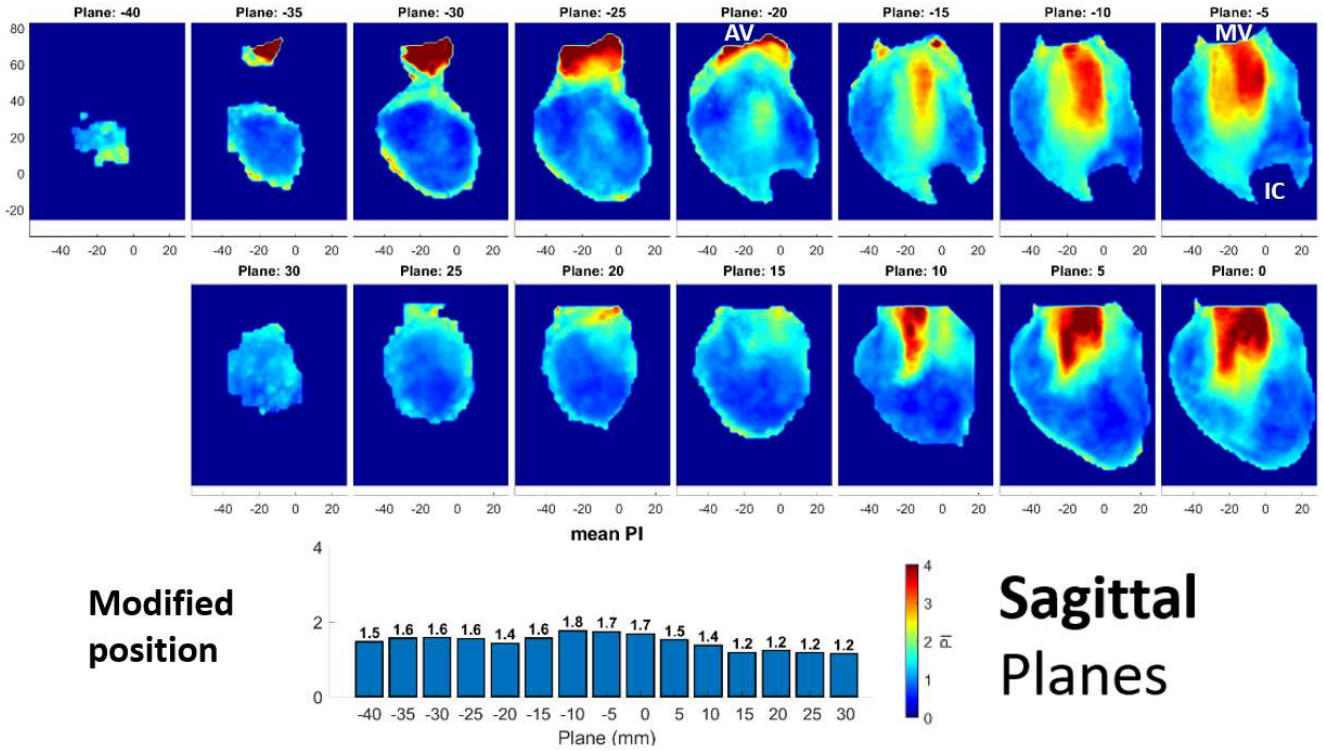

*Figure 46: Pulsatility Index analysis of the **Sagittal** planes for the **modified** pump position and **patient specific contractility** settings (58ml SV). The bar plot shows the mean PI value calculated over each plane.*

4.4.1.3 ROI Calculations:

PI was calculated in the previously specified apical ROIs in seven planes (Table 3). Inside these apical ROIs and for Patient Specific Contractility settings only three planes showed improvements for the Modified position in terms of increased mean PI: Cor 25mm (+5.0%), Cor 20mm (+15.4%) and Cor 15mm (+3.6%). All other cases show higher mean PIs occurring for the in-situ pump position. Overall, mean PI is decreased by 7.2% on average for the apical ROIs in the modified model and Patient Specific contractility settings.

Mean PI calculated in the seven selected ROIs for the Patient Specific contractility setting alone are presented in Figure 47.

Apical ROI				In- Situ Model			Modified Model		
Side	Plane	Support Type	Stroke Volume	mean PI	median PI	SD	mean PI	median PI	SD
Sag	-5mm	Full Support	SV35	1.58	1.60	0.14	1.43	1.31	0.29
		Patient Specific	SV58	1.61	1.66	0.17	1.51	1.60	0.13
		Standard Partial Support	SV64	1.55	1.47	0.10	1.47	1.42	0.12
	0mm	Full Support	SV35	1.78	1.71	0.17	0.94	1.11	0.12
		Patient Specific	SV58	1.60	1.59	0.12	1.12	1.21	0.15
		Standard Partial Support	SV64	1.74	1.62	0.11	1.12	1.14	0.10
	5mm	Full Support	SV35	1.31	1.36	0.14	0.81	0.72	0.09
		Patient Specific	SV58	1.42	1.52	0.07	1.03	1.04	0.10
		Standard Partial Support	SV64	1.50	1.55	0.14	1.12	1.15	0.08
Cor	25mm	Full Support	SV35	0.99	1.00	0.18	1.51	1.59	0.18
		Patient Specific	SV58	1.72	1.90	0.29	1.81	1.63	0.22
		Standard Partial Support	SV64	1.81	1.71	0.34	1.72	1.64	0.21
	20mm	Full Support	SV35	1.07	1.11	0.18	1.45	1.56	0.19
		Patient Specific	SV58	1.71	1.71	0.22	1.98	1.88	0.35
		Standard Partial Support	SV64	1.83	1.75	0.25	1.80	1.67	0.32
	15mm	Full Support	SV35	1.32	1.44	0.16	1.78	1.72	0.02
		Patient Specific	SV58	2.01	2.16	0.18	2.08	2.00	0.22
		Standard Partial Support	SV64	1.84	1.88	0.18	1.97	1.90	0.19
	10mm	Full Support	SV35	1.47	1.39	0.19	2.01	1.99	0.25
		Patient Specific	SV58	1.93	1.81	0.15	1.72	1.77	0.29
		Standard Partial Support	SV64	1.77	1.81	0.12	1.83	1.84	0.24

Table 3: PI Results within the specified apical ROIs in the selected planes. The blue highlighted rows show the results for the Patient Specific contractility settings (SV58). Mean and median PI is increased in the modified pump position in coronal planes (mean increase of 14.8% over all Coronal planes), while it it reduced in sagittal planes (24.9% reduction over all Sagittal planes).

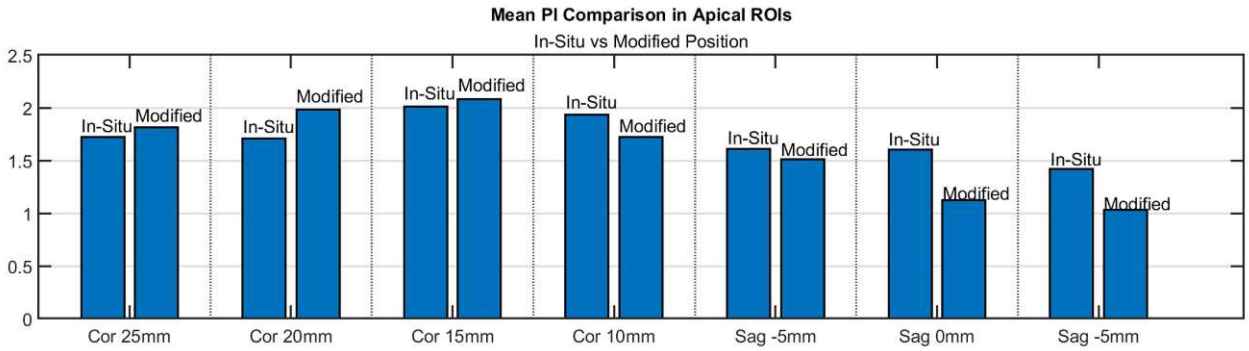

Figure 47: Comparison of mean PI values in the seven selected ROIs between each model. In 3 cases PI was increased, while four planes showed decreased pulsatility for the modified pump position apical ROIs.

5. Discussion

This project was performed to demonstrate a novel and patient specific model creation process and to compare intraventricular flow fields and related parameters between two pump positions for one patient using PIV. The results showed that the effects of altered pump placement on apical washout can be important in improving clinical outcomes for LVAD patients and will be discussed in this chapter.

5.1 Intraventricular Flow Discussion

Disruption of the natural intraventricular flow can lead to an increase in thromboembolic risk and other adverse events. While neurological adverse event rates have been comparable between all currently implanted LVADs such as the HM3 and HVAD [8], several publications have highlighted the importance of proper pump placement inside the supported ventricle with regards to thromboembolic events. The inflow cannula length [38], IC angle [39], IC position [19], [40], IC surface [41] and other design aspects have been shown to have an impact on thromboembolic risk and other important factors [10], [42].

Intraventricular flow fields were presented for two different pump positions (in-situ and modified) and a patient specific contractility setting collected from experiments on patient specific models of LVAD supported LVs. Analysis of the 2D intraventricular flow fields throughout the geometry highlighted the changes resulting from the changed pump position. The direction of the inflow jet was strongly altered by the position of the inflow cannula, leading to changes in apical washout between the models. In general, mitral jet behavior is also determined by several other factors, such as the size of the ventricle, the stroke volume, the MV diameter, the total cardiac output and the ratio of the E- and A-waves.

In these results stagnation was notably reduced within the seven apical ROIs for the apical configuration, which is a result that matches previous publications on comparisons between apical and diaphragmatic implant positions of LVADs [15]. The mean SI occurring in the modified model's apex were reduced by 27.8% on average over the in-situ model. This strong decrease in stagnation could indicate better outcomes with this pump position, as thrombus formation and other adverse events are linked to poor washout of the apex. Two planes in particular showed drastically improved situations: Sagittal plane -5mm showed a decrease of the mean SI in the apical ROI of 53.0% and Coronal plane 10mm showed a decrease of 44.5%.

Pulsatility Index analysis showed less favorable results for the modified pump position, with lower mean PI in many cases. A possible explanation for the improved pulsatility of the diaphragmatic configuration is that the pathway of the mitral jet in the in-situ model appears to lead to more redistribution of the mitral jet throughout the model by misalignment with the IC axis. In the modified model this jet is more aligned with the IC and does not appear to produce regions of increased pulsatility around the apex of the model.

Additionally, increased washout was observed via decreasing SI at the LVOT with decreasing pump support (or with increasing SVs). LVOT washout was especially low when no aortic valve opening occurred (Full Support). Washout at the apex was dependent on the direction of the inflow jet and, for the modified pump position, inversely proportional to the level of LVAD support, as reported in previous studies. In the in-situ pump position this relationship was, however, not true: mean SI was occasionally increased with increasing stroke volume (decreasing pump support). It appears that the diaphragmatic position of the LVAD was not capable of translating increased mitral jet velocity with increased apical washout consistently.

This work highlights the importance of considering LVAD implant position in preoperative assessment. Minimization of stagnation inside the apex of the ventricle reduces the risk of adverse events in LVAD patients, further improving survival rates and patient outcomes.

6. Limitations

The experiments performed in this work are limited models of patient specific ventricles under LVAD support and should be considered simplified models. Only one LV model was investigated and the quality of CT images that are currently available from LVAD patients contain many artefacts which make accurate modeling difficult. Modifications had to be made to the original segmentation of the in-situ model to accommodate for the modified pump position, which could influence the data gathered.

Additionally, the cardiac CT images used in segmentation were obtained during diastole, yet they were used as the end-systolic volume in the mock flow loop setup.

The mock loop setup used in these experiments is able to model the Windkessel effect, it is not able to reproduce many other physiologic mechanisms present in native hearts, such as the Frank Starling mechanism. The LVAD is placed within the mock loop setup in a fixed position and the LV model is attached to the pump and the MV and AV holders, prohibiting any movement of these three attachment points.

While pump flow, pump speed, arterial pressure and some other parameters were available from the patient, the stroke volume, ejection fraction and aortic flow were not captured. The heart rate was also maintained at a constant 80 BPM.

7. Conclusion

A process for the creation of patient specific flexible and transparent models of LVAD supported LVs was demonstrated and subsequently used in PIV experiments, where two pump positions were investigated. The outcomes of the flow field analysis confirm that washout in the critical areas of thrombus formation can be strongly influenced by the pump position. Mitral jet behavior seems to play a significant role in creating washout and the LVAD has a strong influence on its behavior. Stagnation was reduced in the apex of the modified model when compared to the in-situ model, while pulsatility showed decreases in many cases for the same areas. High stagnation inside the apex has been linked to increased thromboembolic risk, therefore it seems that the modified pump position indicates improved clinical outcomes over the diaphragmatic configuration. These findings highlight the importance of considering imaging data and state of the art knowledge for optimization of personalized LVAD treatment strategies to improve outcomes and patient wellbeing, especially with regards to LVAD IC positioning inside the LV.

References

[1] E. J. Molina *et al.*, "The Society of Thoracic Surgeons Intermacs 2020 Annual Report," *The Annals of Thoracic Surgery*, vol. 111, no. 3, pp. 778–792, Mar. 2021, doi: 10.1016/j.athoracsur.2020.12.038.

[2] P. C. Colombo *et al.*, "Comprehensive Analysis of Stroke in the Long-Term Cohort of the MOMENTUM 3 Study: A Randomized Controlled Trial of the HeartMate 3 Versus the HeartMate II Cardiac Pump," *Circulation*, vol. 139, no. 2, Art. no. 2, Jan. 2019, doi: 10.1161/CIRCULATIONAHA.118.037231.

[3] M. R. Mehra *et al.*, "A Fully Magnetically Levitated Circulatory Pump for Advanced Heart Failure," *n engl j med*, p. 11, 2017.

[4] N. Uriel *et al.*, "Hemocompatibility-Related Outcomes in the MOMENTUM 3 Trial at 6 Months: A Randomized Controlled Study of a Fully Magnetically Levitated Pump in Advanced Heart Failure," *Circulation*, vol. 135, no. 21, Art. no. 21, May 2017, doi: 10.1161/CIRCULATIONAHA.117.028303.

[5] A. M. Scandroglio *et al.*, "Diagnosis and Treatment Algorithm for Blood Flow Obstructions in Patients With Left Ventricular Assist Device," vol. 67, no. 23, Art. no. 23, 2016.

[6] F. Kaufmann, C. Hörmandinger, C. Knosalla, V. Falk, and E. Potapov, "Thrombus formation at the inflow cannula of continuous-flow left ventricular assist devices—A systematic analysis," p. 12.

[7] S. S. Najjar, "An analysis of pump thrombus events in patients in the HeartWare ADVANCE bridge to transplant and continued access protocol trial," *The Journal of Heart and Lung Transplantation*, vol. 33, no. 1, Art. no. 1, 2014.

[8] S. Li *et al.*, "Comparison of Neurologic Event Rates Among HeartMate II, HeartMate 3, and HVAD," *ASAIO Journal*, vol. 66, no. 6, Art. no. 6, Jun. 2020, doi: 10.1097/MAT.0000000000001084.

[9] A. Blitz, "Pump thrombosis—A riddle wrapped in a mystery inside an enigma," *Annals of cardiothoracic surgery*, vol. 3, no. 5, Art. no. 5, 2014.

[10] C. H. Glass *et al.*, "Thrombus on the inflow cannula of the HeartWare HVAD: an update," *Cardiovascular Pathology*, vol. 38, pp. 14–20, Jan. 2019, doi: 10.1016/j.carpath.2018.09.002.

[11] K. C. Strickland, J. C. Watkins, G. S. Couper, M. M. Givertz, and R. F. Padera, "Thrombus around the redesigned HeartWare HVAD inflow cannula: A pathologic case series," *The Journal of Heart and Lung Transplantation*, vol. 35, no. 7, Art. no. 7, Jul. 2016, doi: 10.1016/j.healun.2016.01.1230.

[12] K. May-Newman, Y. K. Wong, R. Adamson, P. Hoagland, V. Vu, and W. Dembitsky, "Thromboembolism Is Linked to Intraventricular Flow Stasis in a Patient Supported with a Left Ventricle Assist Device," *ASAIO Journal*, vol. 59, no. 4, Art. no. 4, Jul. 2013, doi: 10.1097/MAT.0b013e318299fced.

[13] E. N. Sorensen, Z. N. Kon, E. D. Feller, S. M. Pham, and B. P. Griffith, "Quantitative Assessment of Inflow Malposition in Two Continuous-Flow Left Ventricular Assist Devices," *The Annals of Thoracic Surgery*, vol. 105, no. 5, pp. 1377–1383, May 2018, doi: 10.1016/j.athoracsur.2017.12.004.

[14] P. Aigner *et al.*, "Pump position and thrombosis in ventricular assist devices: Correlation of radiographs and CT data," *Int J Artif Organs*, vol. 44, no. 12, pp. 956–964, Dec. 2021, doi: 10.1177/03913988211017552.

[15] A. R. Prisco, A. Aliseda, J. A. Beckman, N. A. Mokadam, C. Mahr, and G. J. M. Garcia, "Impact of LVAD Implantation Site on Ventricular Blood Stagnation," *ASAIO J*, vol. 63, no. 4, pp. 392–400, 2017, doi: 10.1097/MAT.0000000000000503.

[16] K. May-Newman, N. Marquez-Maya, R. Montes, and S. Salim, "The Effect of Inflow Cannula Angle on the Intraventricular Flow Field of the Left Ventricular Assist Device-Assisted Heart: An In Vitro Flow Visualization Study," *ASAIO J*, vol. 65, no. 2, pp. 139–147, Feb. 2019, doi: 10.1097/MAT.0000000000000790.

[17] T. Imamura *et al.*, "Cannula and Pump Positions Are Associated With Left Ventricular Unloading and Clinical Outcome in Patients With HeartWare Left Ventricular Assist Device," *J Card Fail*, vol. 24, no. 3, pp. 159–166, Mar. 2018, doi: 10.1016/j.cardfail.2017.09.013.

[18] V. K. Chivukula *et al.*, "Left Ventricular Assist Device Inflow Cannula Angle and Thrombosis Risk," *Circ Heart Fail*, vol. 11, no. 4, p. e004325, Apr. 2018, doi: 10.1161/CIRCHEARTFAILURE.117.004325.

[19] M. Ghodrati *et al.*, "The influence of left ventricular assist device inflow cannula position on thrombosis risk," *Artif Organs*, vol. 44, no. 9, pp. 939–946, Sep. 2020, doi: 10.1111/aor.13705.

[20] adh30 revised work by D. who revised original work of D. R. as S. by xavax, *A Wiggers diagram, showing the cardiac cycle events occuring in the left ventricle.* 2016. Accessed: Sep. 01, 2023. [Online]. Available: https://commons.wikimedia.org/wiki/File:Wiggers_Diagram_2.svg#/media/File:Wiggers_Diagram_2.svg

[21] K. H. Fraser, T. Zhang, M. E. Taskin, B. P. Griffith, and Z. J. Wu, "A Quantitative Comparison of Mechanical Blood Damage Parameters in Rotary Ventricular Assist Devices: Shear Stress, Exposure Time and Hemolysis Index," *J Biomech Eng*, vol. 134, no. 8, pp. 0810021–08100211, Aug. 2012, doi: 10.1115/1.4007092.

[22] M. Giersiepen, L. J. Wurzinger, R. Opitz, and H. Reul, "Estimation of Shear Stress-related Blood Damage in Heart Valve Prostheses - in Vitro Comparison of 25 Aortic Valves," *Int J Artif Organs*, vol. 13, no. 5, pp. 300–306, May 1990, doi: 10.1177/039139889001300507.

[23] V. L. Rayz *et al.*, "Numerical modeling of the flow in intracranial aneurysms: prediction of regions prone to thrombus formation," *Ann Biomed Eng*, vol. 36, no. 11, pp. 1793–1804, Nov. 2008, doi: 10.1007/s10439-008-9561-5.

[24] V. L. Rayz *et al.*, "Flow Residence Time and Regions of Intraluminal Thrombus Deposition in Intracranial Aneurysms," *Ann Biomed Eng*, vol. 38, no. 10, pp. 3058–3069, 2010, doi: 10.1007/s10439-010-0065-8.

[25] P. A. Holme *et al.*, "Shear-Induced Platelet Activation and Platelet Microparticle Formation at Blood Flow Conditions as in Arteries With a Severe Stenosis," *Arteriosclerosis, Thrombosis, and Vascular Biology*, vol. 17, no. 4, pp. 646–653, Apr. 1997, doi: 10.1161/01.ATV.17.4.646.

[26] I. Chung and G. Y. H. Lip, "Virchow's Triad Revisited: Blood Constituents," *Pathophysiology of Haemostasis and Thrombosis*, vol. 33, no. 5–6, pp. 449–454, Jan. 2005, doi: 10.1159/000083844.

[27] K. K. Marinescu, N. Uriel, D. L. Mann, and D. Burkhoff, "Left ventricular assist device-induced reverse remodeling: it's not just about myocardial recovery," *Expert Rev Med Devices*, vol. 14, no. 1, pp. 15–26, Jan. 2017, doi: 10.1080/17434440.2017.1262762.

[28] M. Raffel, C. E. Willert, F. Scarano, C. J. Kähler, S. T. Wereley, and J. Kompenhans, *Particle Image Velocimetry: A Practical Guide*. Cham: Springer International Publishing, 2018. doi: 10.1007/978-3-319-68852-7.

[29] "Raffel: Notes on Argon-ion lasers," in *Particle Image Velocimetry: A Practical Guide*, Cham: Springer International Publishing, 2018, p. 64. doi: 10.1007/978-3-319-68852-7.

[30] "Raffel: Tracer Particles," in *Particle Image Velocimetry: A Practical Guide*, Cham: Springer International Publishing, 2018, p. 33f. doi: 10.1007/978-3-319-68852-7.

[31] P. K. Kundu and I. M. Cohen, in *Fluid Mechanics - 3rd Edition*, Third Edition.Elsevier Academic Press, 2004, p. 97. Accessed: Apr. 11, 2023. [Online]. Available: https://www.elsevier.com/books/fluid-mechanics/cohen/978-0-08-047023-8

[32] P. K. Kundu and I. M. Cohen, in *Fluid Mechanics - 3rd Edition*, Third Edition.Elsevier Academic Press, 2004, p. 278. Accessed: Apr. 11, 2023. [Online]. Available: https://www.elsevier.com/books/fluid-mechanics/cohen/978-0-08-047023-8

[33] Unkown, "Laminar Flow and Turbulent Flow." https://i0.wp.com/theconstructor.org/wp-content/uploads/2021/11/Laminar-Flow-and-Turbulent-Flow-1.png?resize=417%2C380&ssl=1 (accessed Sep. 01, 2023).

[34] P. K. Kundu and I. M. Cohen, in *Fluid Mechanics - 3rd Edition*, Third Edition.Elsevier Academic Press, 2004, p. 523. Accessed: Apr. 11, 2023. [Online]. Available: https://www.elsevier.com/books/fluid-mechanics/cohen/978-0-08-047023-8

[35] Khienwad, Thananya, "Investigation of cardiac flow patterns in patients with cardiac assist devices using Particle Image Velocimetry: Effects of speed changes and particular patient-specific cardiac geometries," Medical University of Vienna, Austria, Vienna, Austria, 2021.

[36] T. Schlöglhofer, P. Aigner, M. Stoiber, and H. Schima, "Fixation and Mounting of Porcine Aortic Valves for use in Mock Circuits," *Int J Artif Organs*, vol. 36, no. 10, pp. 738–741, Oct. 2013, doi: 10.5301/ijao.5000230.

[37] R. D. Keane and R. J. Adrian, "Optimization of particle image velocimeters. I. Double pulsed systems," *Meas. Sci. Technol.*, vol. 1, no. 11, p. 1202, Nov. 1990, doi: 10.1088/0957-0233/1/11/013.

[38] K. May-Newman *et al.*, "The Effect of Inflow Cannula Length on the Intraventricular Flow Field: An In Vitro Flow Visualization Study Using the Evaheart Left Ventricular Assist

Device," *ASAIO Journal*, vol. 63, no. 5, pp. 592–603, Sep. 2017, doi: 10.1097/MAT.0000000000000559.

[39] K. May-Newman, "The Importance of Left Ventricular Assist Device Inflow Cannula Angle and the Relationship to Cardiac and Anatomical Geometry," *ASAIO J*, vol. 65, no. 5, pp. 419–421, Jul. 2019, doi: 10.1097/MAT.0000000000001026.

[40] T. Schlöglhofer *et al.*, "Inflow cannula position as risk factor for stroke in patients with HeartMate 3 left ventricular assist devices," *Artif Organs*, vol. 46, no. 6, pp. 1149–1157, Jun. 2022, doi: 10.1111/aor.14165.

[41] W. He, J. T. Butcher, G. W. Rowlands, and J. F. Antaki, "Biological Response to Sintered Titanium in Left Ventricular Assist Devices: Pseudoneointima, Neointima, and Pannus," *ASAIO J*, Jun. 2022, doi: 10.1097/MAT.0000000000001777.

[42] S. Liao *et al.*, "Numerical prediction of thrombus risk in an anatomically dilated left ventricle: the effect of inflow cannula designs," *BioMedical Engineering OnLine*, vol. 15, no. 2, p. 136, Dec. 2016, doi: 10.1186/s12938-016-0262-2.

8. Appendix

Due to the large number of results created during data analysis only the Patient Specific contractility setting was presented in the Results section. Here, two further contractility settings are presented for both models: Full Support (SV35) and an additional Standard Support Setting ("Standard Partial Support", SV64). Mean velocities were determined for each plane, along with mean PI and mean SI calculations. The results of the apical calculations for PI and SI are however shown in the Results section (Table 2 and Table 3 contain data for all contractility settings) and will not be presented here again.

8.1 Images of Steady Stream Analysis:

8.1.1 In-Situ Pump Position

8.1.1.1 Full Support

The results of the velocity field analysis for the Full Support setting (SV35) can be seen in Figure 48 and Figure 49. In this situation aortic valve opening does not occur during the cardiac cycle, so lot velocities are observed around the Left Ventricular Outflow Tract (LVOT). In the Sagittal view the vortex ring of the transmitral jet is able to reach the apex in the -5mm plane, however it does not seem to influence the apex at the +5mm plane.

Mean velocity in planes intersecting the apex:

- Cor 25mm: 76 mm/s
- Cor 20mm: 71 mm/s
- Cor 15mm: 76 mm/s
- Cor 10mm: 86 mm/s
- Sag 5mm: 101 mm/s
- Sag 0mm: 109 mm/s
- Sag -5mm: 101mm/s

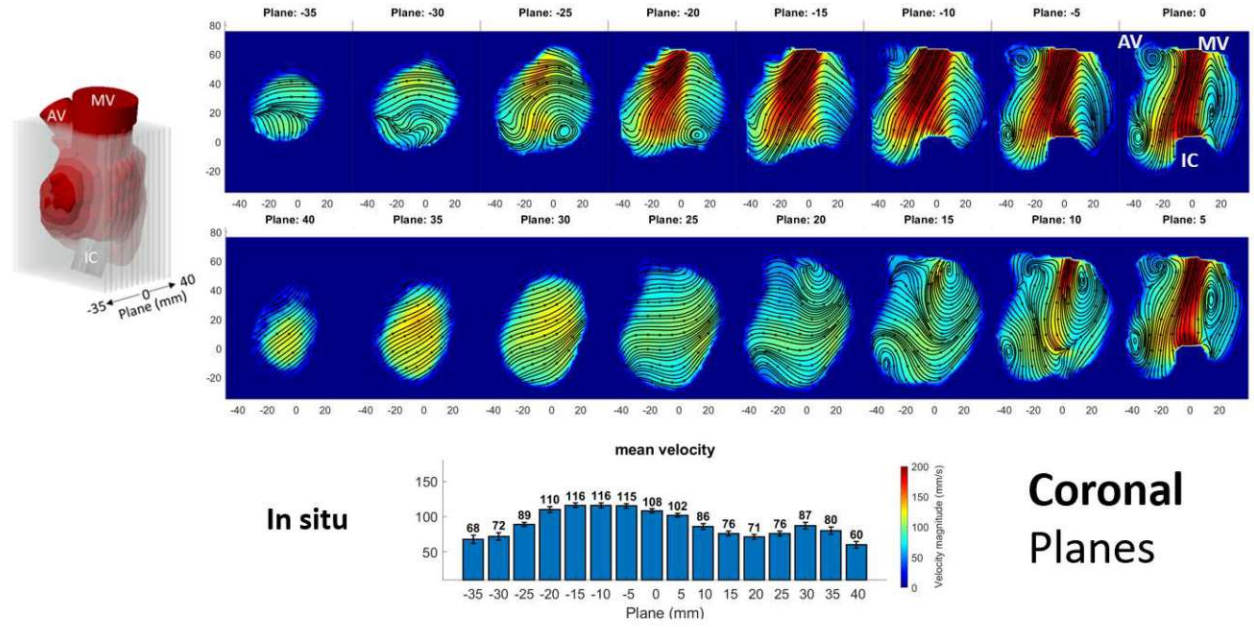

*Figure 48: Mean velocity fields of **Coronal** Planes for the **in-situ** pump position and **Full Support** contractility settings (35ml SV). The bar plot shows the mean velocity calculated over the entire field for each plane.*

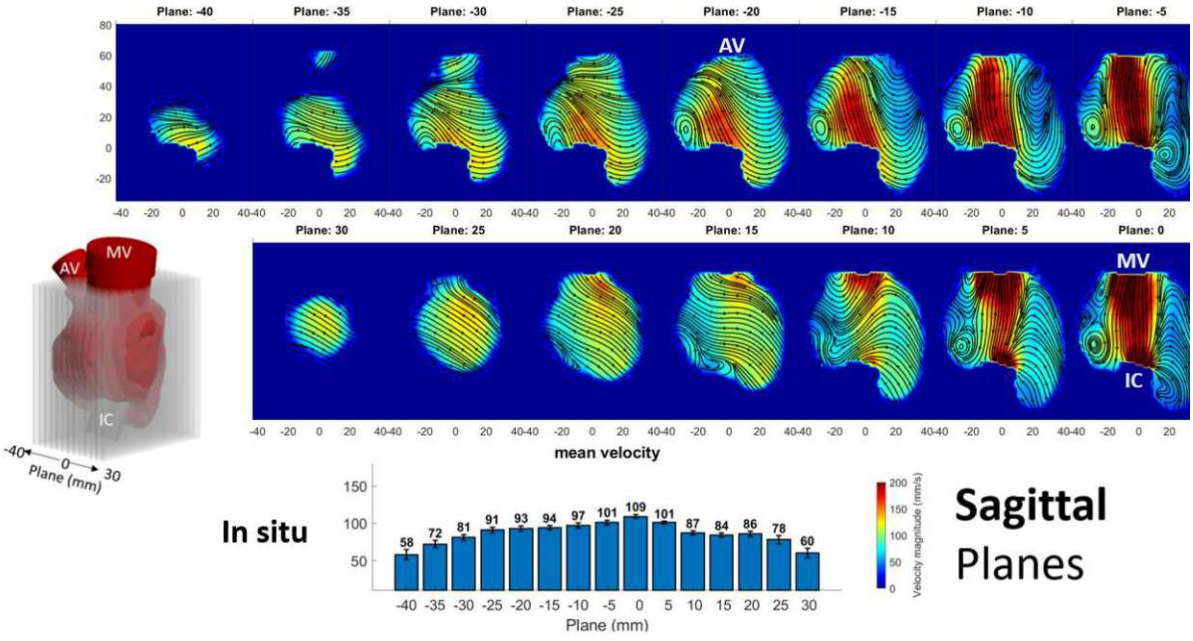

*Figure 49: Mean velocity fields of **Sagittal** Planes for the **in-situ** pump position and **Full Support** contractility settings (35ml SV). The bar plot shows the mean velocity calculated over the entire field for each plane.*

8.1.1.2 Partial Support 2

The results of the mean velocity field analysis for the in-situ model and the Standard Partial Support setting (SV64) can be seen in Figure 50 and Figure 51. The apical situation is similar

to the Patient Specific setting, with slightly increased velocities over the patient specific mean velocities in each plane.

Mean velocity in planes intersecting the apex:

- Cor 25mm: 73 mm/s
- Cor 20mm: 70 mm/s
- Cor 15mm: 72 mm/s
- Cor 10mm: 86 mm/s
- Sag 5mm: 120 mm/s
- Sag 0mm: 118 mm/s
- Sag -5mm: 105 mm/s

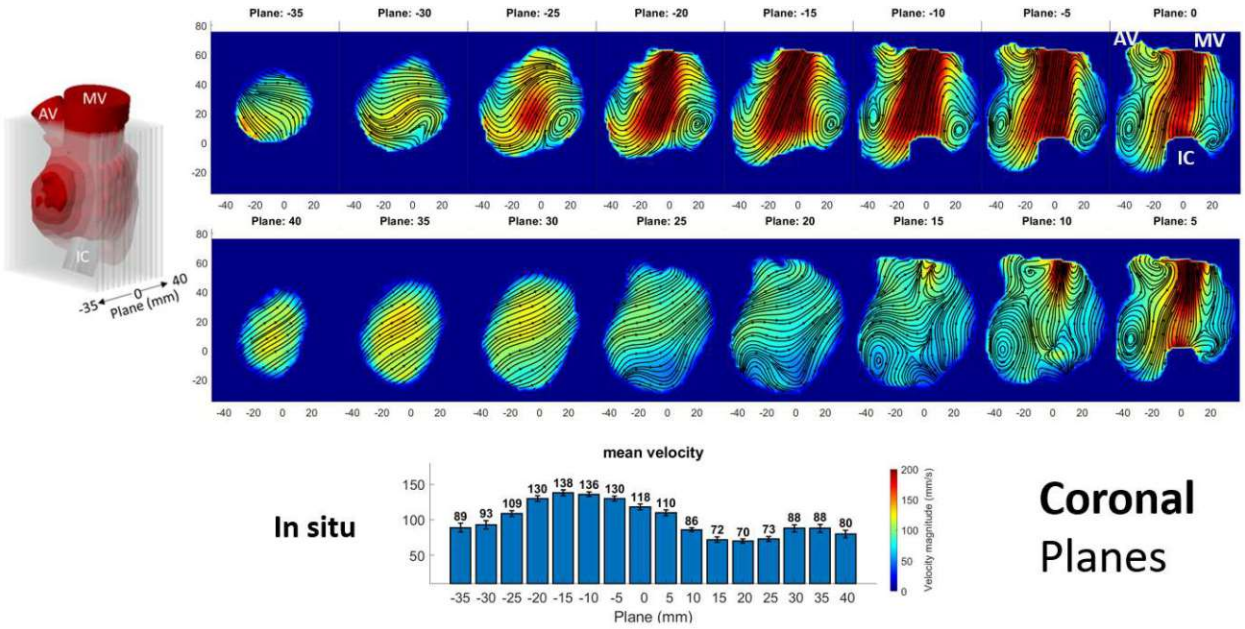

*Figure 50: Mean velocity fields of **Coronal** Planes for the **modified** pump position and **Standard Partial Support** contractility settings (64ml SV). The bar plot shows the mean velocity calculated over the entire field for each plane.*

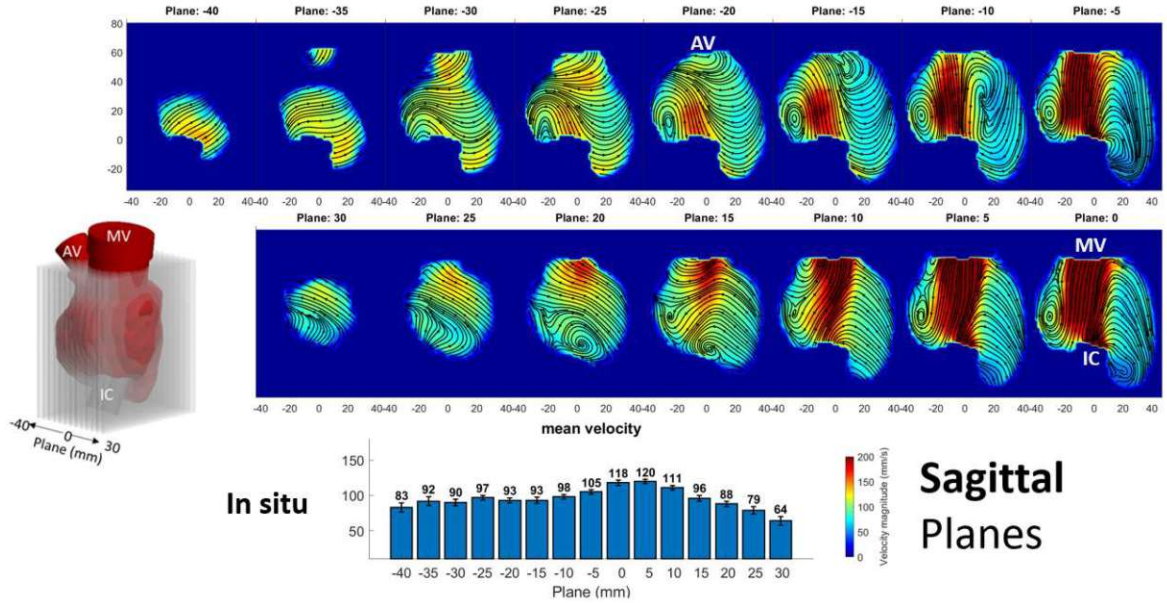

*Figure 51: Mean velocity fields of **Sagittal** Planes for the **modified** pump position and **Standard Partial Support** contractility settings (64ml SV). The bar plot shows the mean velocity calculated over the entire field for each plane.*

8.1.2 Modified Pump Position

8.1.2.1 Full Support

The results of the velocity field analysis for the modified pump position and Full support (SV35) contractility settings can be seen in Figure 52 and Figure 53.

Mean velocity in planes intersecting the apex:

- Cor 25mm: 69 mm/s
- Cor 20mm: 78 mm/s
- Cor 15mm: 96 mm/s
- Cor 10mm: 109 mm/s
- Sag 5mm: 98 mm/s
- Sag 0mm: 111 mm/s
- Sag -5mm: 123 mm/s

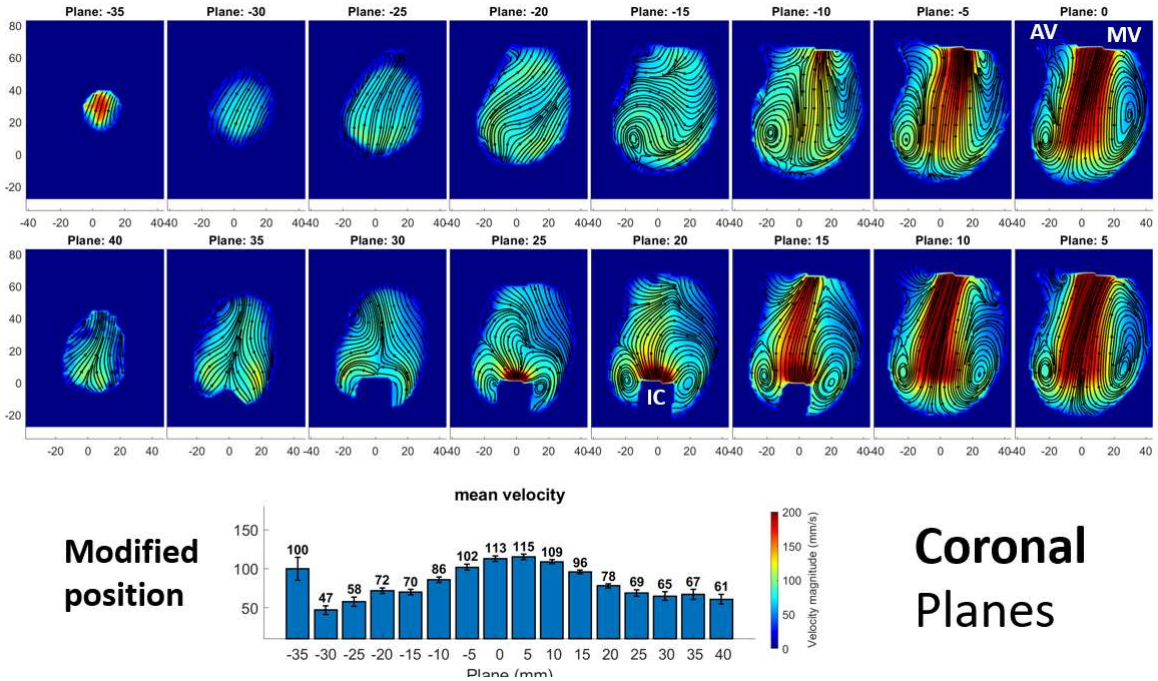

*Figure 52: Mean velocity fields of **Coronal** Planes for the **modified** pump position and **Full Support** contractility settings (35ml SV). The bar plot shows the mean velocity calculated over the entire field for each plane.*

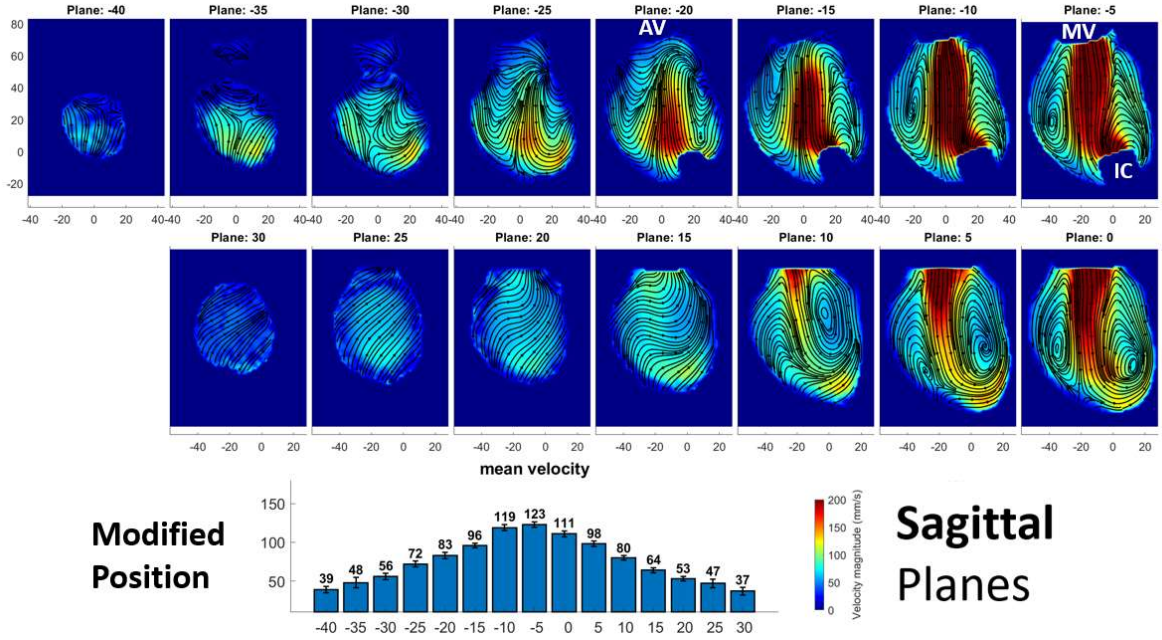

*Figure 53: Mean velocity fields of **Sagittal** Planes for the **modified** pump position and **Full Support** contractility settings (35ml SV). The bar plot shows the mean velocity calculated over the entire field for each plane.*

8.1.2.2 Partial Support 2

The results for the mean velocity field analysis of the modified pump position and Standard Partial support settings (SV64) can be seen in Figure 54 and Figure 55.

Mean velocity in planes intersecting the apex:

- Cor 25mm: 87 mm/s
- Cor 20mm: 96 mm/s
- Cor 15mm: 116 mm/s
- Cor 10mm: 128 mm/s
- Sag 5mm: 111 mm/s
- Sag 0mm: 128 mm/s
- Sag -5mm: 139 mm/s

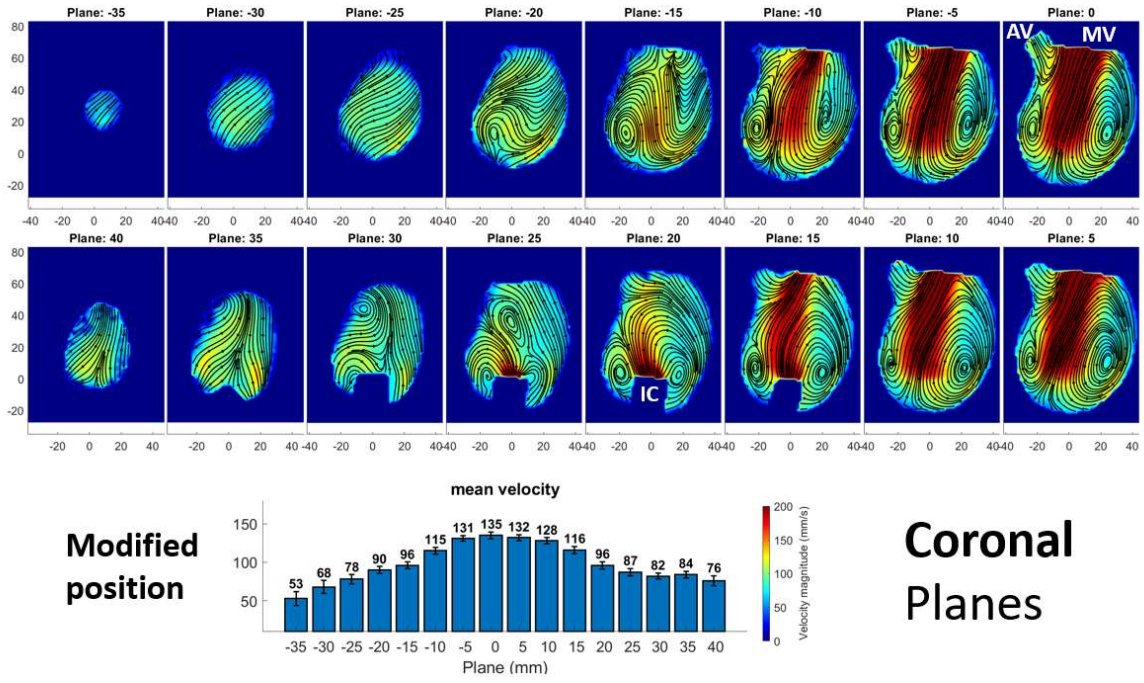

*Figure 54: Mean velocity fields of **Coronal** Planes for the **modified** pump position and **Standard Partial Support** contractility settings (64ml SV). The bar plot shows the mean velocity calculated over the entire field for each plane.*

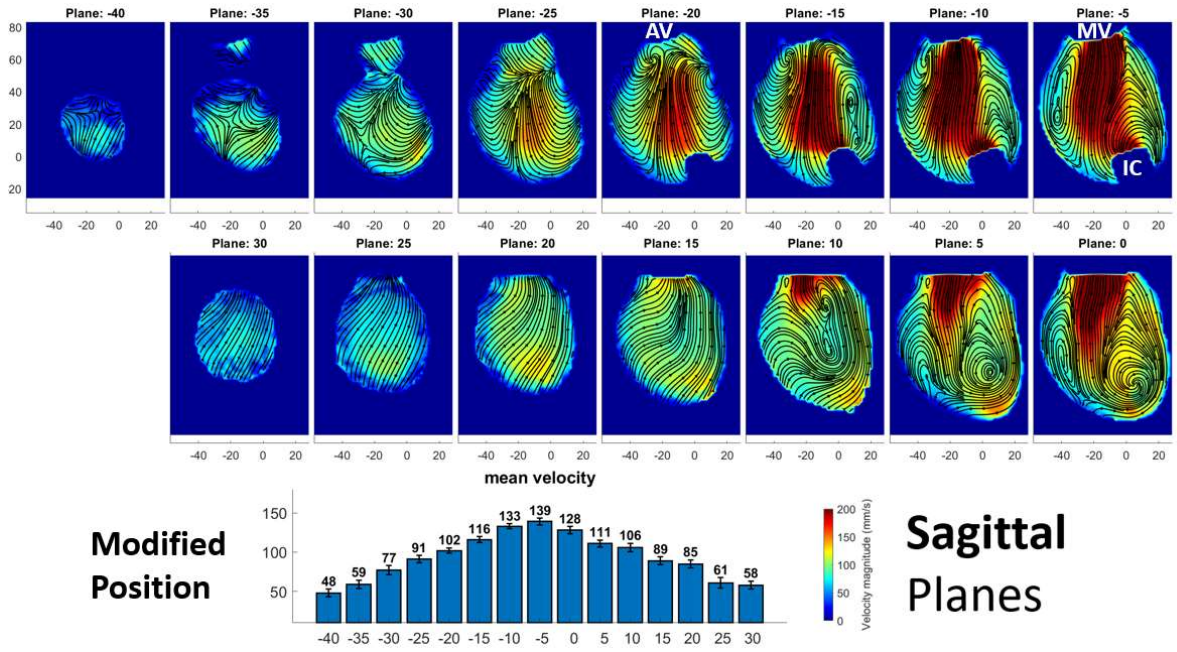

*Figure 55: Mean velocity fields of **Sagittal** Planes for the **modified** pump position and **Standard Partial Support** contractility settings (64ml SV). The bar plot shows the mean velocity calculated over the entire field for each plane.*

8.2 Pulsatility Index Analysis

8.2.1 In-Situ Pump Position

8.2.1.1 Full Support

Mean Pulsatility Index results for the Full Support (SV35) situation and In-situ pump position can be seen in Figure 56 and Figure 57.

Mean PI in planes intersecting the apex:

- Cor 25mm: 0.7
- Cor 20mm: 0.8
- Cor 15mm: 0.9
- Cor 10mm: 1.1
- Sag 5mm: 1.7
- Sag 0mm: 1.7
- Sag -5mm: 1.5

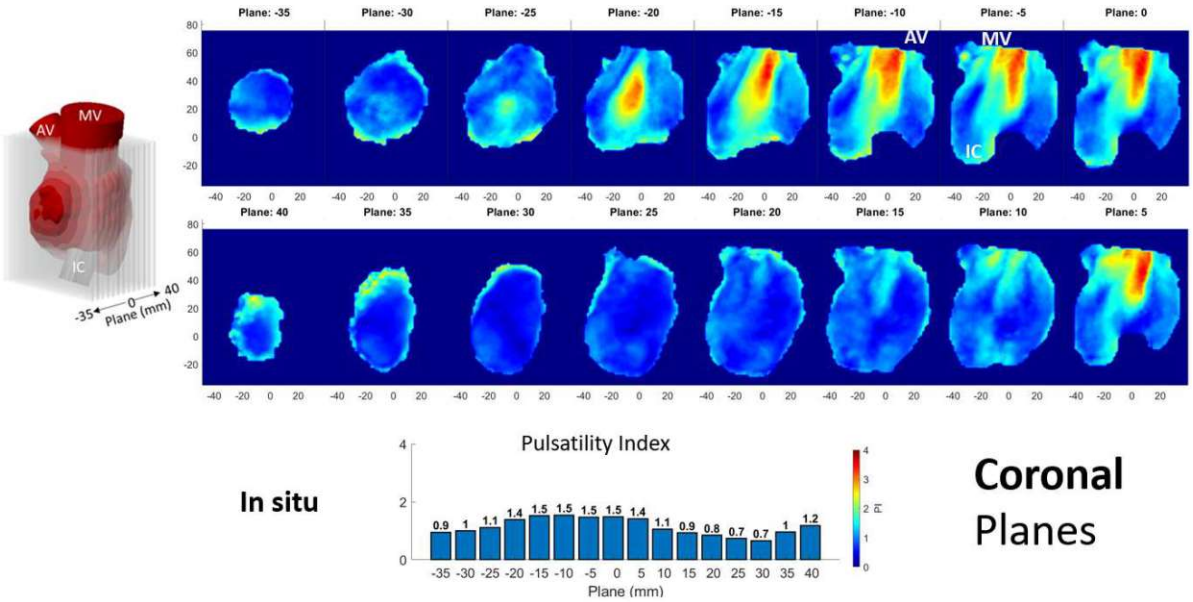

*Figure 56: The mean PI for the **Coronal** Planes for the **in-situ** pump position and **Full Support** contractility settings (35ml SV). The bar plot shows the mean velocity calculated over the entire field for each plane.*

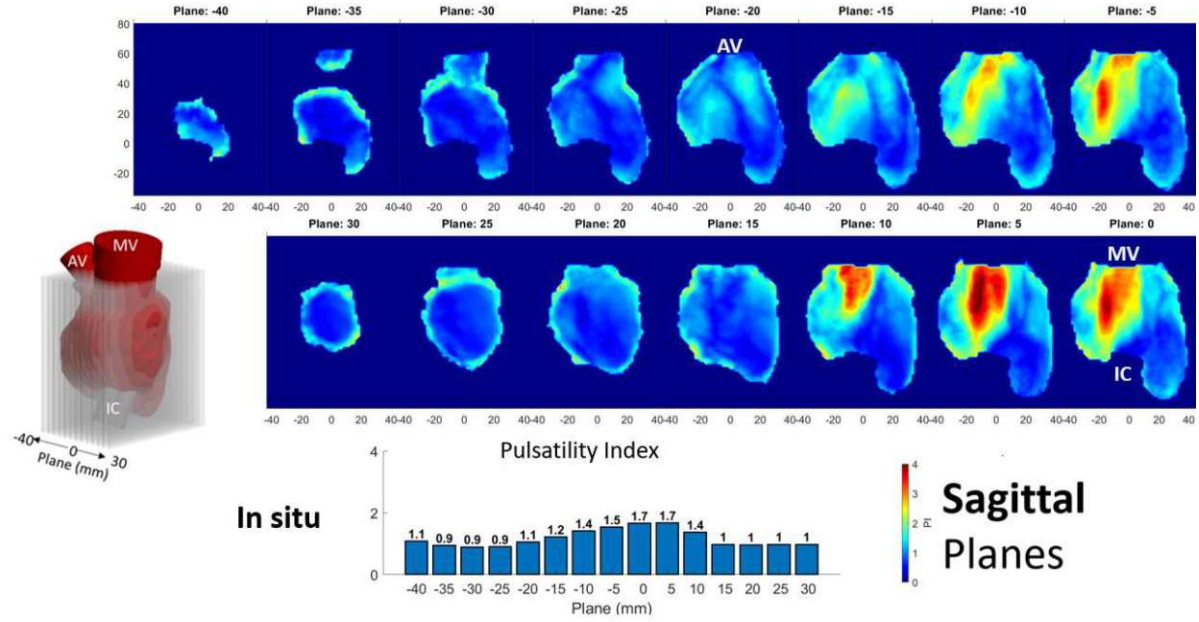

*Figure 57: The mean PI for the **Sagittal** Planes for the **in-situ** pump position and **Full Support** contractility settings (35ml SV). The bar plot shows the mean velocity calculated over the entire field for each plane.*

8.2.1.2 Partial Support 2

Mean Pulsatility Index results for the Standard Partial Support situation (SV64) and In-situ pump position can be seen in Figure 58 and Figure 59.

Mean PI in planes intersecting the apex:

- Cor 25mm: 1
- Cor 20mm: 1.1
- Cor 15mm: 1.3
- Cor 10mm: 1.7
- Sag 5mm: 2
- Sag 0mm: 1.8
- Sag -5mm: 1.8

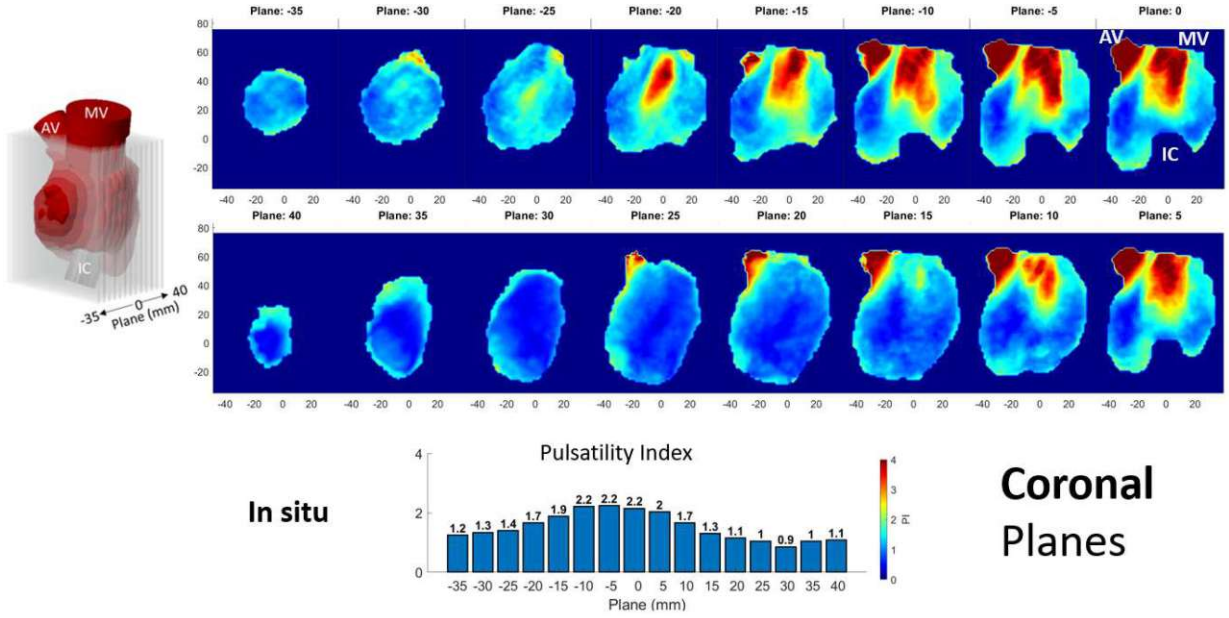

*Figure 58: The mean PI for the **Coronal** Planes for the **in-situ** pump position and **Standard Partial Support** contractility settings (64ml SV). The bar plot shows the mean velocity calculated over the entire field for each plane.*

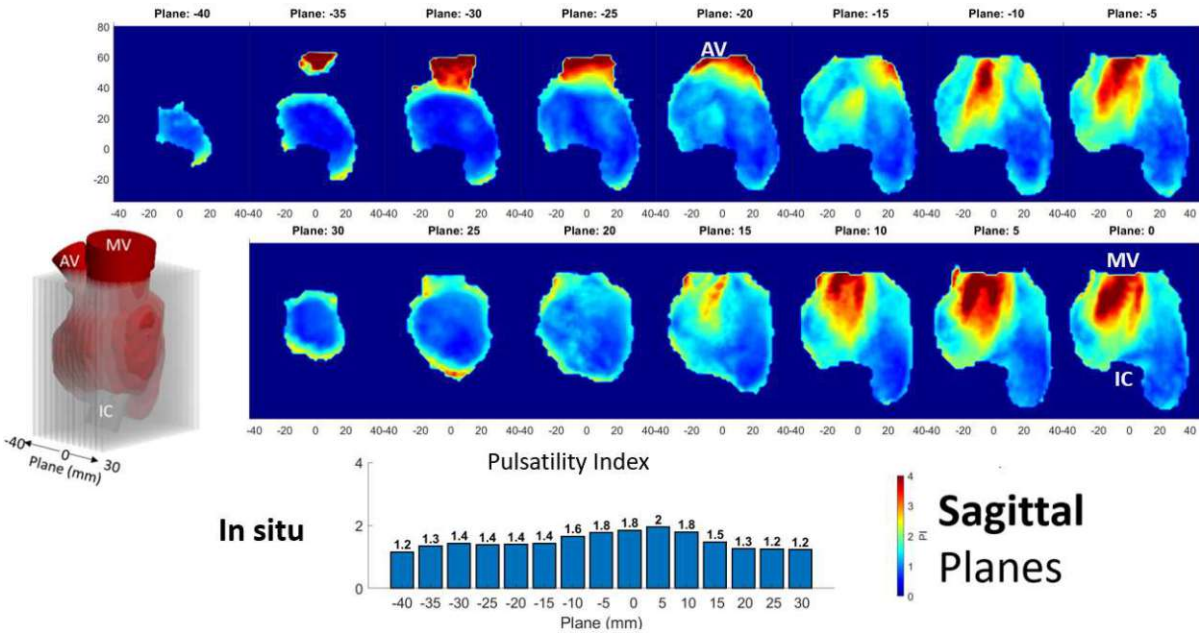

*Figure 59: The mean PI for the **Sagittal** Planes for the **in-situ** pump position and **Standard Partial Support** contractility settings (64ml SV). The bar plot shows the mean velocity calculated over the entire field for each plane.*

8.2.2 Modified Pump Position

8.2.2.1 Full Support

Mean Pulsatility Index results for the Full Support (SV35) situation and modified pump position can be seen in Figure 60 and Figure 61.

Mean PI in planes intersecting the apex:

- Cor 25mm: 1
- Cor 20mm: 1.2
- Cor 15mm: 1.4
- Cor 10mm: 1.5
- Sag 5mm: 1.5
- Sag 0mm: 1.6
- Sag -5mm: 1.7

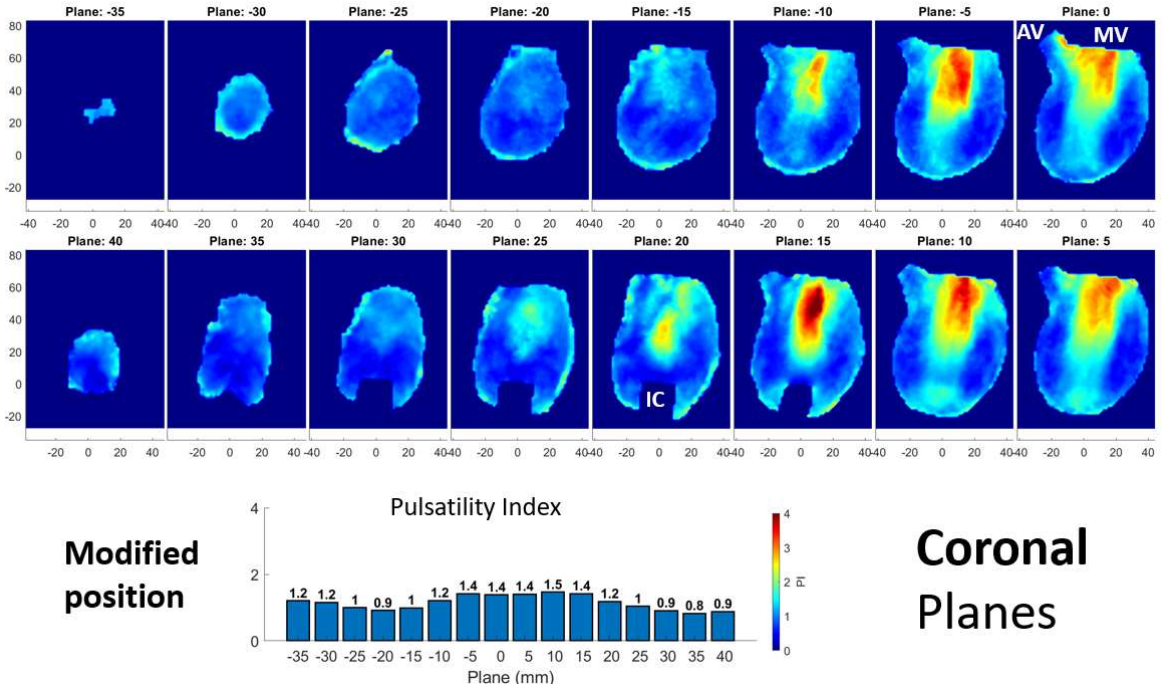

*Figure 60: The mean PI for the **Coronal** Planes for the **Modified** pump position and **Full Support contractility** settings (35ml SV). The bar plot shows the mean velocity calculated over the entire field for each plane.*

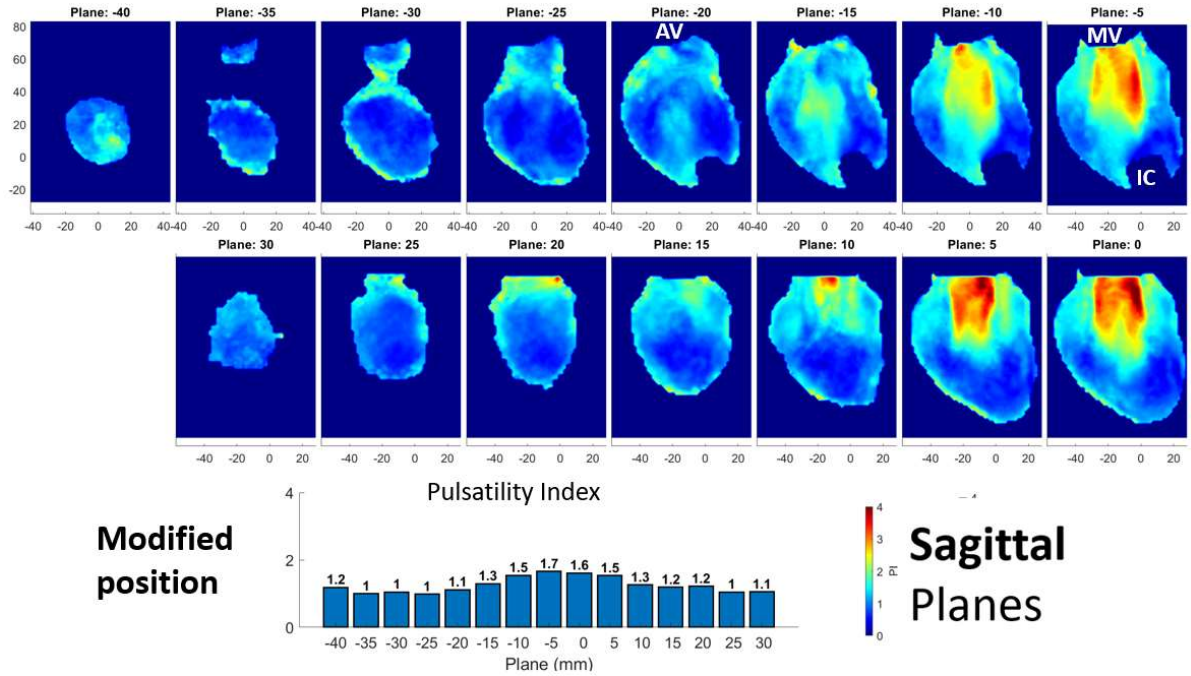

*Figure 61: The mean PI for the **Sagittal** Planes for the **Modified** pump position and **Full Support contractility** settings (35ml SV). The bar plot shows the mean velocity calculated over the entire field for each plane.*

8.2.2.2 Partial Support 2

Mean Pulsatility Index results for the Standard Partial Support (SV64) situation and In-situ pump position can be seen in Figure 62 and Figure 63.

Mean PI in planes intersecting the apex:

- Cor 25mm: 1.2
- Cor 20mm: 1.4
- Cor 15mm: 1.8
- Cor 10mm: 2
- Sag 5mm: 1.6
- Sag 0mm: 1.7
- Sag -5mm: 1.8

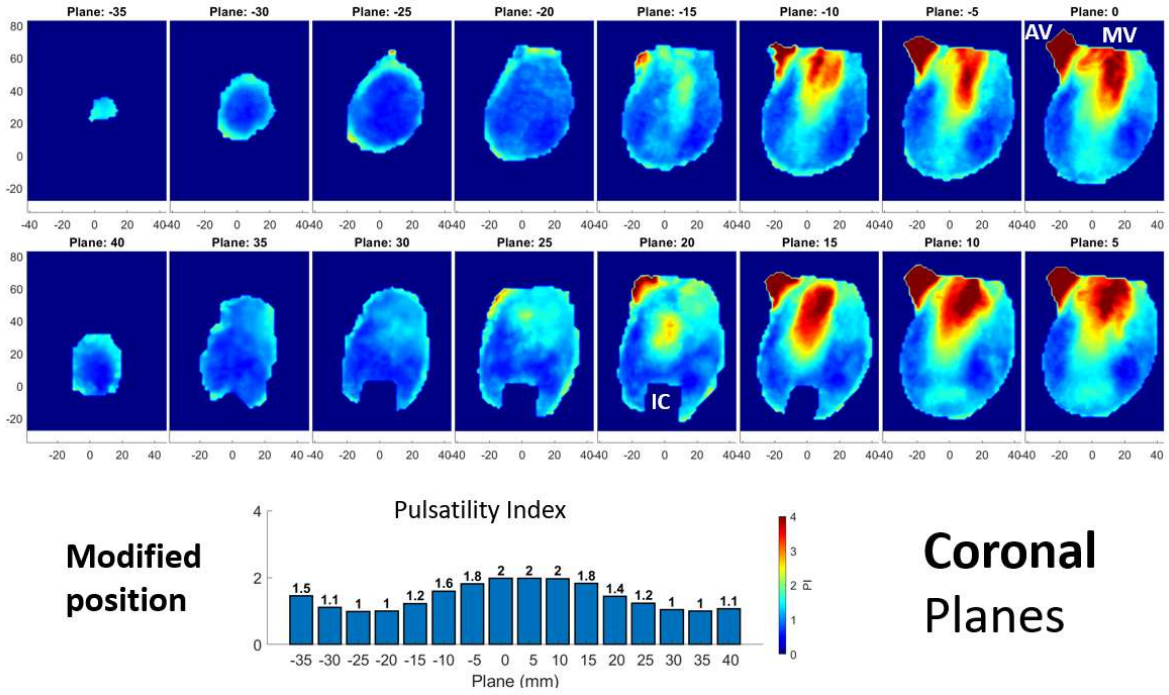

*Figure 62: The mean PI for the **Coronal** Planes for the **Modified** pump position and **Standard Partial Support** contractility settings (64ml SV). The bar plot shows the mean velocity calculated over the entire field for each plane.*

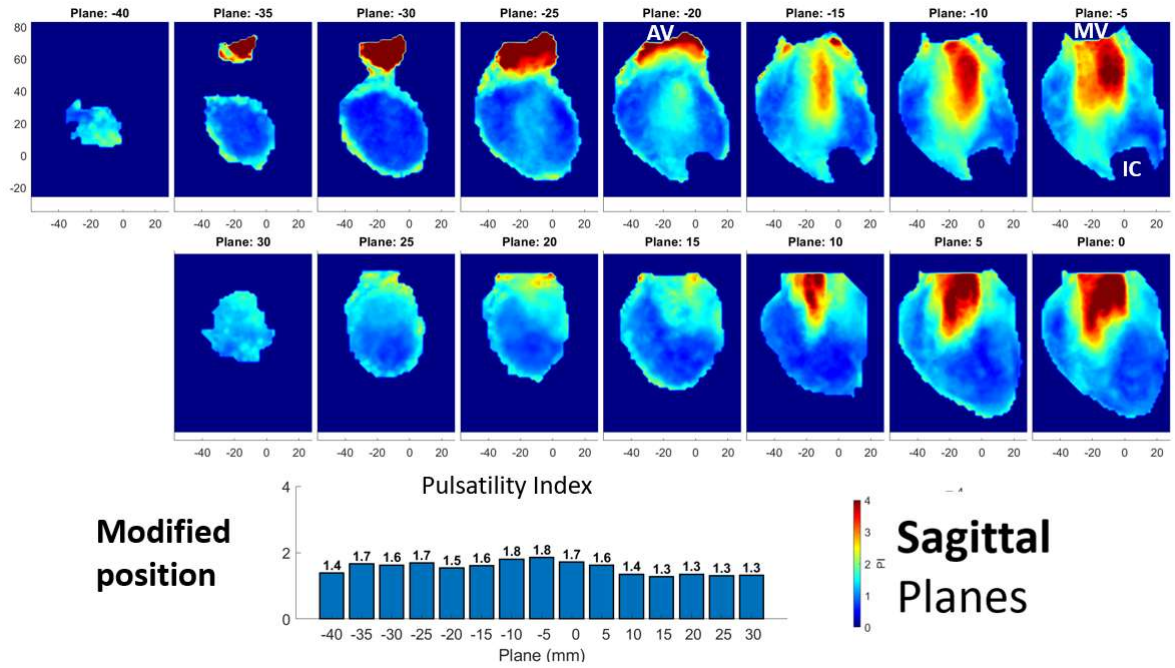

*Figure 63: The mean PI for the **Sagittal** Planes for the **Modified** pump position and **Standard Partial Support** contractility settings (64ml SV). The bar plot shows the mean velocity calculated over the entire field for each plane.*

8.3 Stagnation Index Analysis

8.3.1 In-Situ Pump Position

8.3.1.1 Full Support

Mean Stagnation Index results for the Full Support situation and In-situ pump position can be seen in Figure 56 and Figure 57.

Mean SI in planes intersecting the apex:

- Cor 25mm: 1 $s*m^{-1}$
- Cor 20mm: 1.1 $s*m^{-1}$
- Cor 15mm: 1 $s*m^{-1}$
- Cor 10mm: 0.9 $s*m^{-1}$
- Sag 5mm: 0.8 $s*m^{-1}$
- Sag 0mm: 0.8 $s*m^{-1}$
- Sag -5mm: 0.8 $s*m^{-1}$

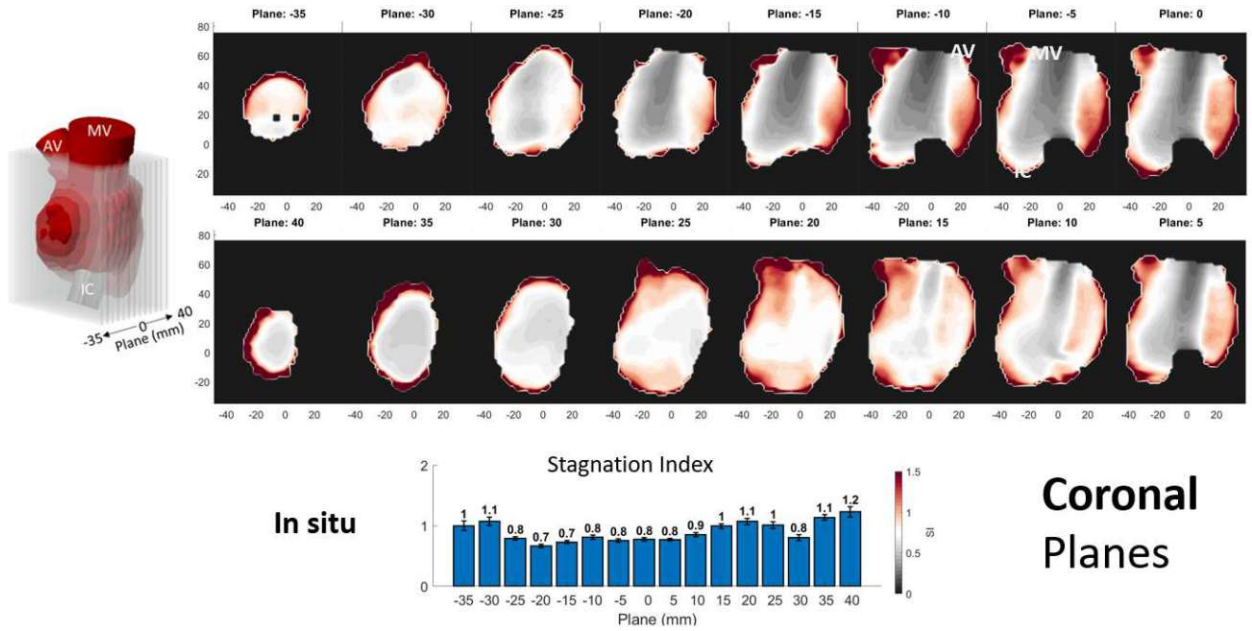

*Figure 64: The mean SI for the **Coronal** Planes for the **in-situ** pump position and **Full Support** contractility settings (35ml SV). The bar plot shows the mean velocity calculated over the entire field for each plane.*

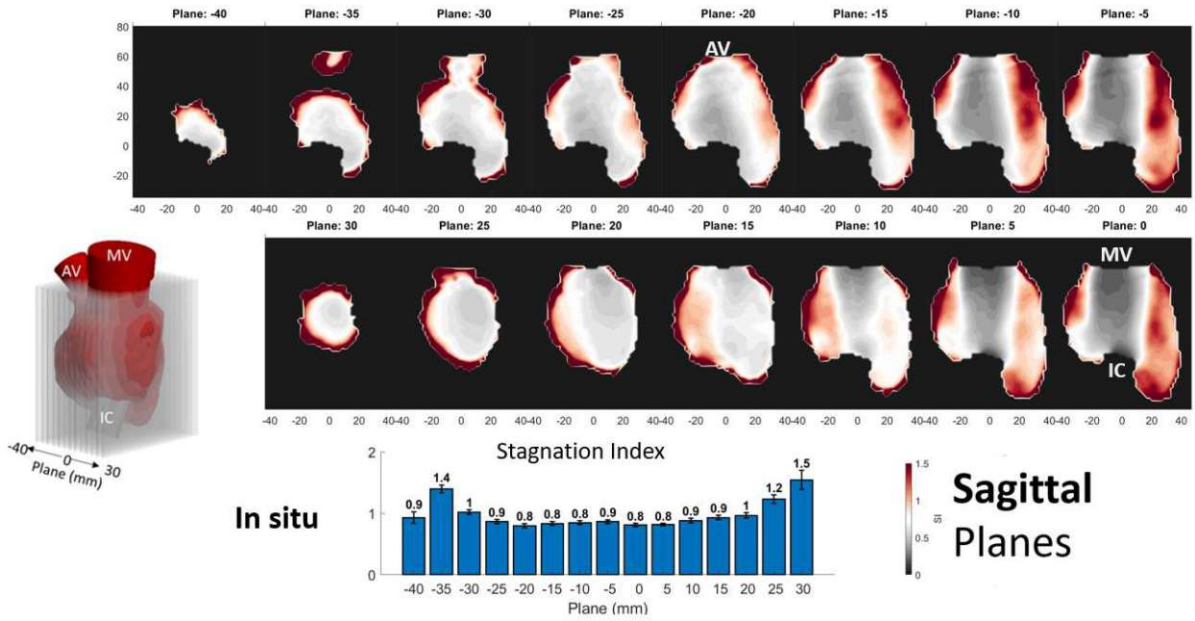

*Figure 65: The mean SI for the **Sagittal** Planes for the **in-situ** pump position and **Full Support** contractility settings (35ml SV). The bar plot shows the mean velocity calculated over the entire field for each plane.*

8.3.1.2 Partial Support 2

Mean Stagnation Index results for the Standard Partial Support (SV64) situation and In-situ pump position can be seen in Figure 62 and Figure 63.

Mean SI in planes intersecting the apex:

- Cor 25mm: 1 $s*m^{-1}$
- Cor 20mm: 1 $s*m^{-1}$
- Cor 15mm: 1 $s*m^{-1}$
- Cor 10mm: 0.8 $s*m^{-1}$
- Sag 5mm: 0.7 $s*m^{-1}$
- Sag 0mm: 0.7 $s*m^{-1}$
- Sag -5mm: 0.8 $s*m^{-1}$

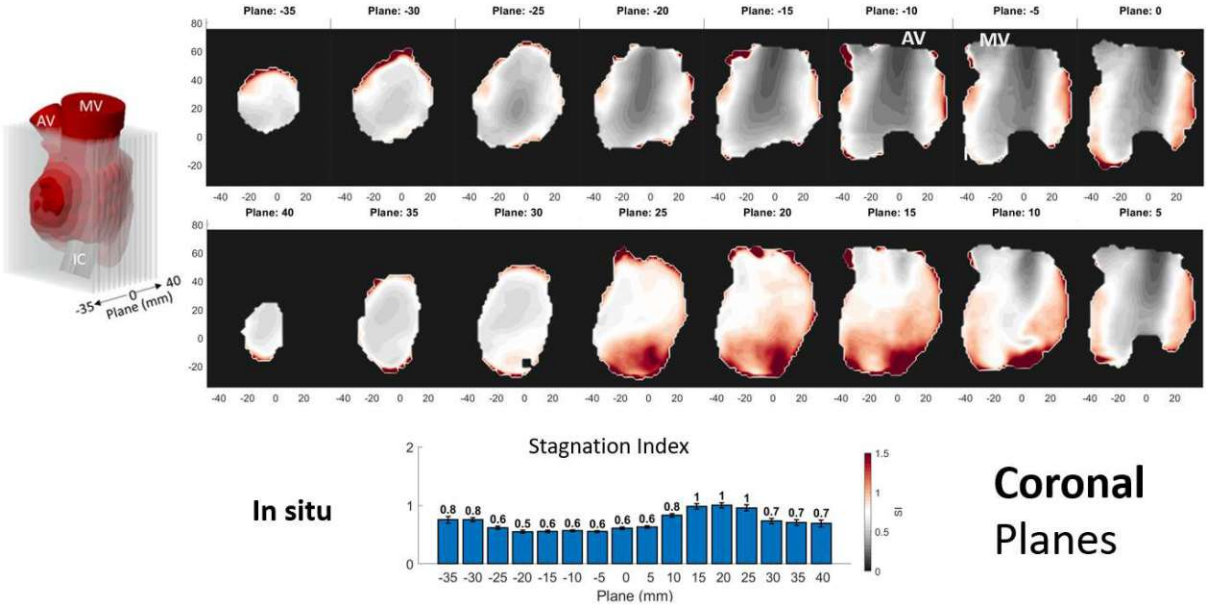

*Figure 66: The mean SI for the **Coronal** Planes for the **in-situ** pump position and **Standard Partial Support** contractility settings (64ml SV). The bar plot shows the mean velocity calculated over the entire field for each plane.*

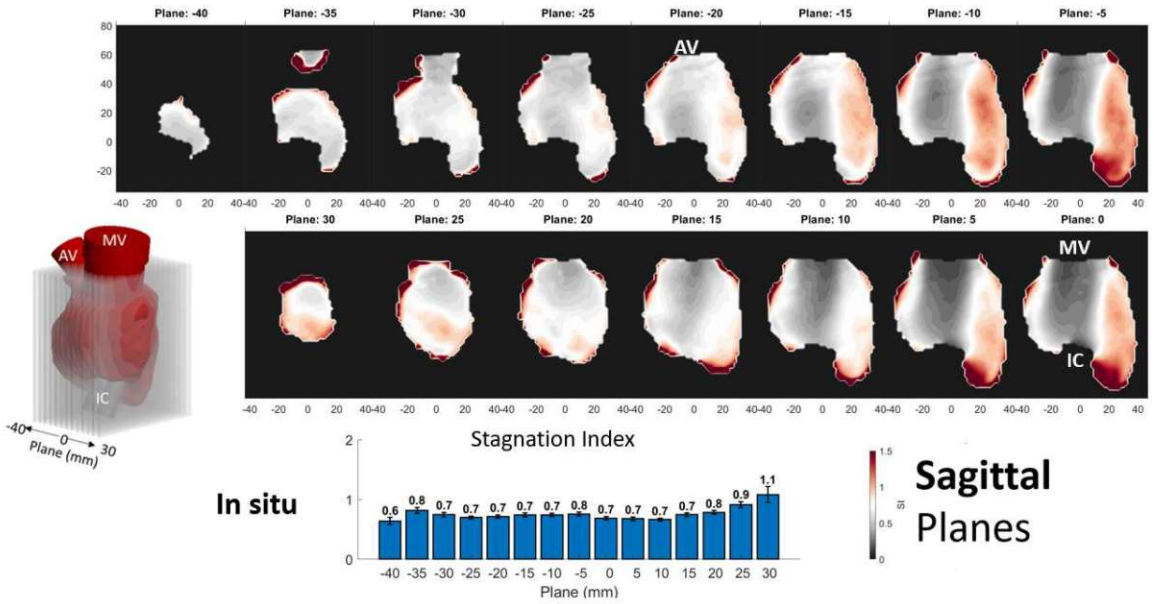

*Figure 67: The mean SI for the **Sagittal** Planes for the **in-situ** pump position and **Standard Partial Support** contractility settings (64ml SV). The bar plot shows the mean velocity calculated over the entire field for each plane.*

8.3.2 Modifed Pump Position

8.3.2.1 Full Support

Mean Stagnation Index results for the Full Support (SV35) situation and modified pump position can be seen in Figure 68 and Figure 69.

Mean SI in planes intersecting the apex:

- Cor 25mm: 1.1 $s*m^{-1}$
- Cor 20mm: 1.1 $s*m^{-1}$
- Cor 15mm: 0.9 $s*m^{-1}$
- Cor 10mm: 0.8 $s*m^{-1}$
- Sag 5mm: 0.8 $s*m^{-1}$
- Sag 0mm: 0.7 $s*m^{-1}$
- Sag -5mm: 0.7 $s*m^{-1}$

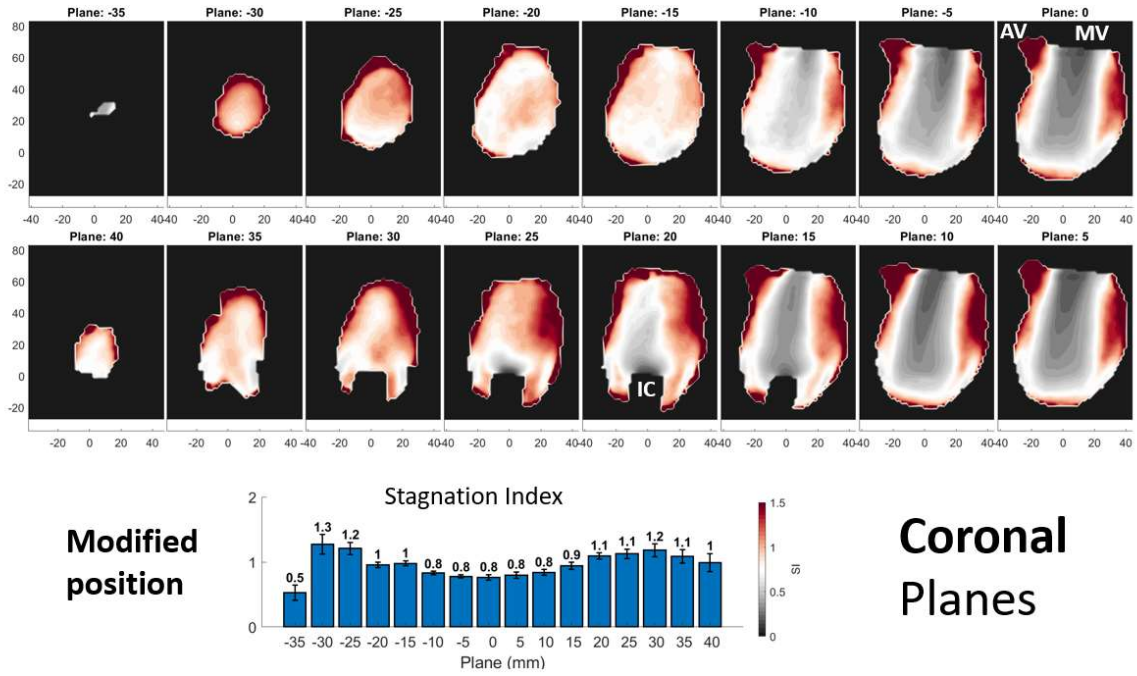

*Figure 68: The mean SI for the **Coronal** Planes for the **Modified** pump position and **Full Support** contractility settings (35ml SV). The bar plot shows the mean velocity calculated over the entire field for each plane.*

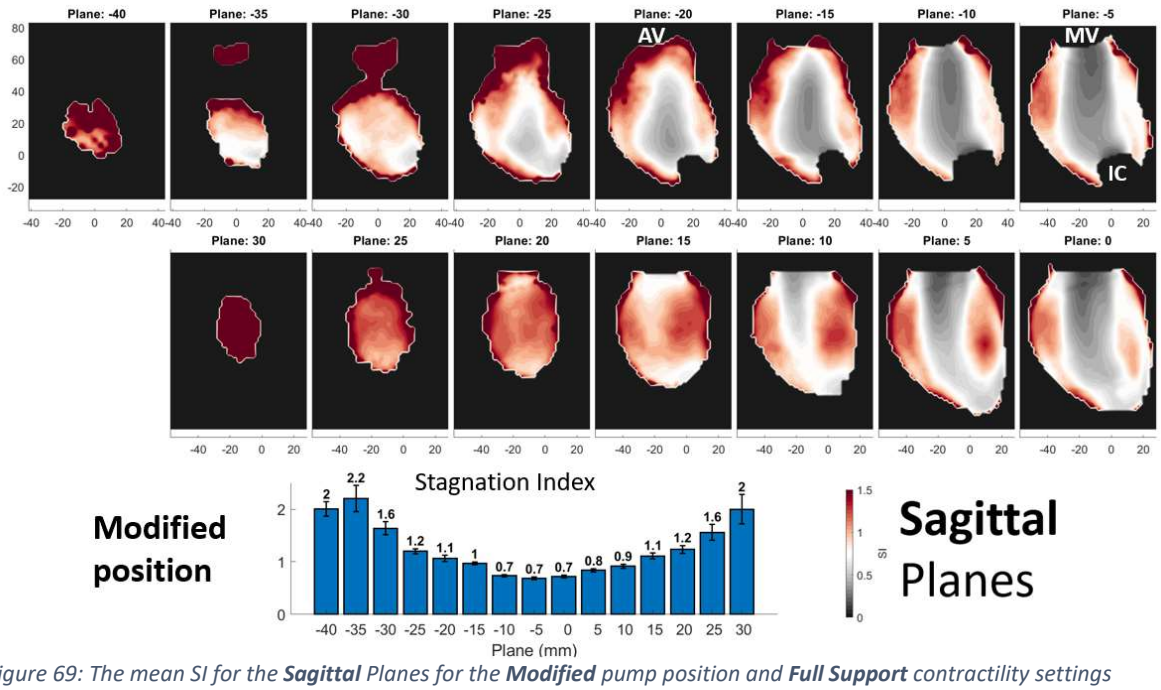

*Figure 69: The mean SI for the **Sagittal** Planes for the **Modified** pump position and **Full Support** contractility settings (35ml SV). The bar plot shows the mean velocity calculated over the entire field for each plane.*

8.3.2.2 Partial Support 2

Mean Stagnation Index results for the Standard Partial Support setting (SV34) and modified pump position can be seen in Figure 70 and Figure 71.

Mean SI in planes intersecting the apex:

- Cor 25mm: 0.8 $s*m^{-1}$
- Cor 20mm: 0.8 $s*m^{-1}$
- Cor 15mm: 0.7 $s*m^{-1}$
- Cor 10mm: 0.6 $s*m^{-1}$
- Sag 5mm: 0.7 $s*m^{-1}$
- Sag 0mm: 0.6 $s*m^{-1}$
- Sag -5mm: 0.5 $s*m^{-1}$

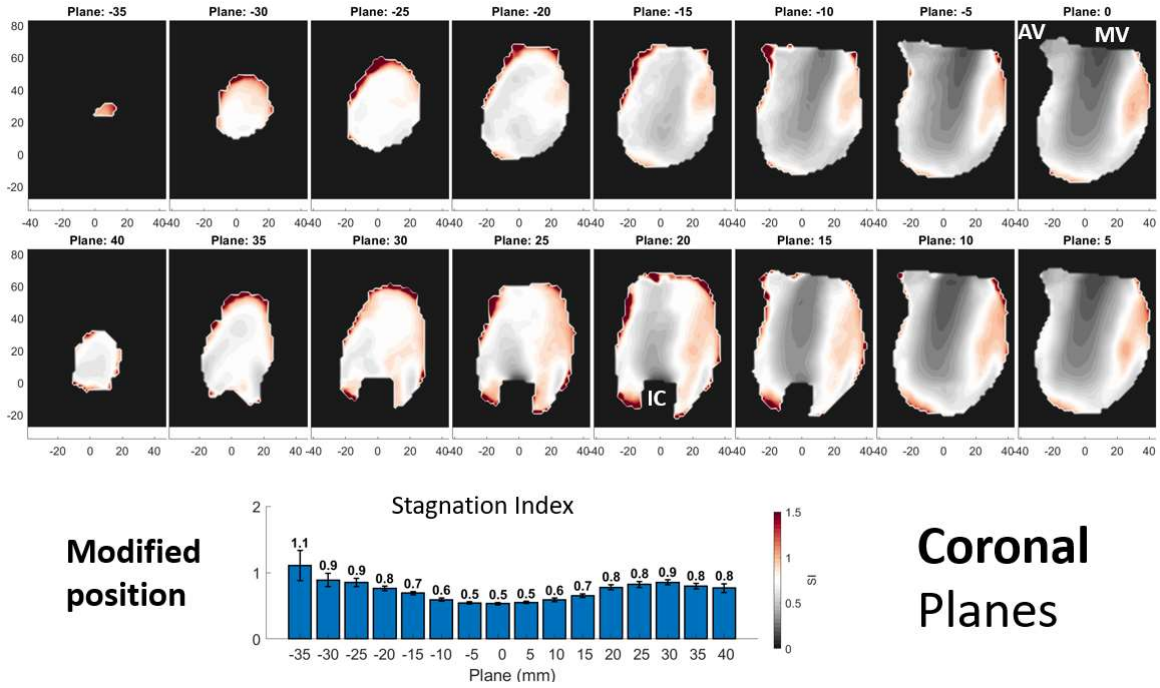

*Figure 70: The mean SI for the **Coronal** Planes for the **Modified** pump position and **Standard Partial Support** contractility settings (64ml SV). The bar plot shows the mean velocity calculated over the entire field for each plane.*

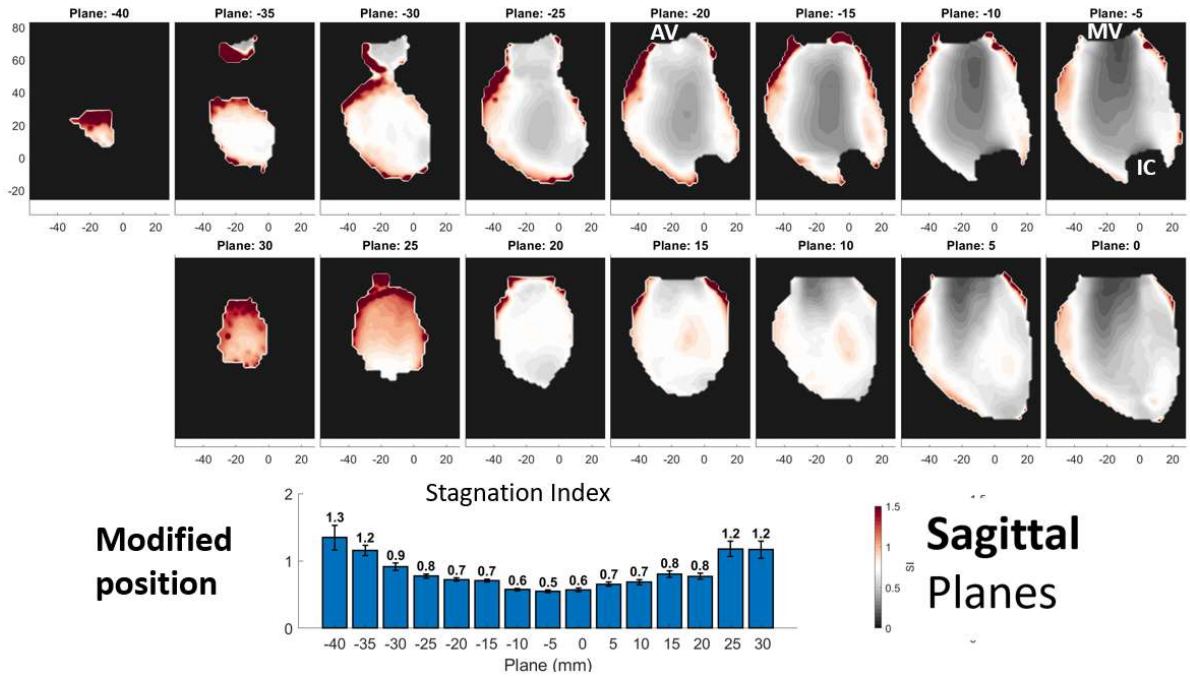

*Figure 71: The mean SI for the **Sagittal** Planes for the **Modified** pump position and **Standard Partial Support** contractility settings (64ml SV). The bar plot shows the mean velocity calculated over the entire field for each plane.*